EPIGENETIC THERAPY TIES MYC DEPLETION TO REVERSING IMMUNE EVASION AND TREATING LUNG CANCER

By:
Michael J. Topper

A dissertation submitted to Johns Hopkins University in conformity with the requirements for the degree of Doctor of Philosophy

Baltimore, Maryland
10/2017

Abstract

Combining DNA demethylating agents (DNMTis) with histone deacetylase inhibitors (HDACis) holds promise for enhancing cancer immune therapy. Herein, pharmacologic and isoform specificity of HDACi's are investigated to guide their addition to a DNMTi, thus devising a new, low-dose, sequential regimen which imparts a robust anti-tumor effect for non-small cell lung cancer (NSCLC). Using in vitro treated NSCLC cell lines, we elucidate an Interferon-αβ based transcriptional program with accompanying upregulation of antigen presentation machinery mediated in part through dsRNA induction. This is accompanied by suppression of MYC signaling and an increase in the T cell chemoattractant, CCL5. Use of this combination treatment schema in mouse models of NSCLC reverses tumor immune evasion and modulates T-cell exhaustion state towards memory and effector T-cell phenotypes. Key correlative science metrics emerge for an upcoming clinical trial, testing enhancement of immune checkpoint therapy for NSCLC.

Advisor:	Dr. Stephen Baylin (Reader)
Thesis committee:	Dr. Robert Casero (Reader) Dr. Edward Gabrielson Dr. Christine Hann Dr. Cynthia Zahnow

Figure 1: Graphical Abstract

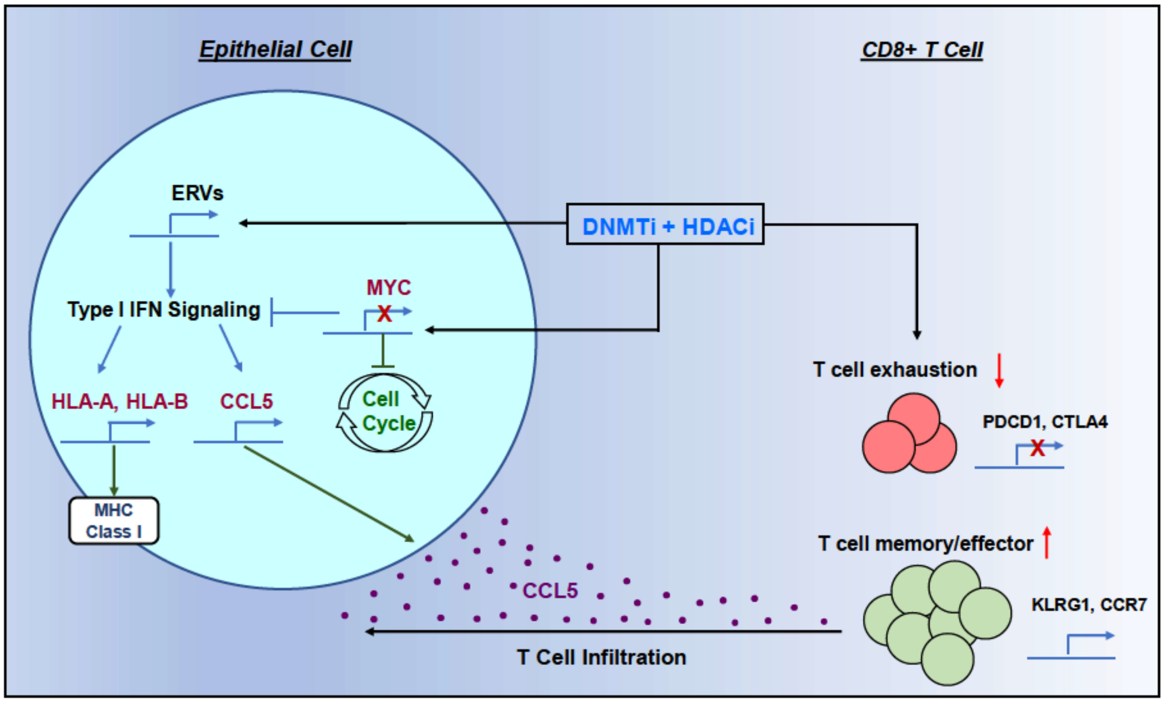

Table of contents

I. Introduction

II. NSCLC epithelial cell specific response to combined epigenetic treatment

III. MYC perturbation as a driver of response to epigenetic treatment

IV. Combination epigenetic treatment exerts a robust anti-tumor effect in 2 independent mouse models

V. Combination epigenetic treatment alters the tumor immune microenvironment, most markedly on the lymphocyte compartment.

VI. Combination epigenetic treatment inhibits tumor growth through CD8$^+$ T cells and MYC dependent mechanisms

List of Tables:

List of Figures

I. Introduction

1. Disease specific background: Lung cancer

The work presented herein focuses on therapeutic intervention for the leading cause of cancer deaths in the world, lung cancer. This disease is classified into 2 broad categories based on histological classification: small cell and non-small cell lung cancers. Approximately 85% of all lung cancers present as non-small lung cancer (NSCLC) and this will be the focus of the presented work. NSCLC is comprised of 3 major subtypes: adenocarcinoma, squamous cell carcinoma, and large cell carcinomas (Herbst et al., 2008). The most prevalent type of NSCLC is adenocarcinoma which presents most commonly with either TP53 and Kras mutations, but rarely with both (Cancer Genome Atlas Research Network. 2014). Squamous cell carcinomas, the other dominant subtype have a high frequency of TP53 mutations (Cancer Genome Atlas Research Network., 2012). Deriving therapeutic efficacy in this solid malignancy has been problematic. While immune therapy has been a breakthrough for the management of this disease, only a minority of patients respond durably. A major challenge for the field is increasing the proportion of patients who respond durably through derivations of both rational combination therapies and identification of biomarkers predictive of response beyond PD-L1 positivity alone.

2. DNA: Methylation, Methyltransferases (DNMT) and Methyltransferase Inhibitors (DNMTis)

2.1 DNA Methylation

DNA methylation is a stable modification with differential functionality depending on the region of the genome incorporated. Promoter DNA methylation acts as a transcriptionally repressive modification which recruits nuclear repressor complexes, thus instilling a repressive chromatin state which is negatively correlated with transcription factor binding (Jones, Baylin, 2007). Gene body methylation is associated with transcriptionally active genes, although the causation of this modification in facilitating gene transcription is largely unknown and therefore may be merely correlated with the act of active transcription (Duymich et al., 2016). Enhancer methylation is even more elusive, while there is evidence that methylation of enhancers is anti-correlated with transcription factor binding and thus gene expression (Chartlet et al., 2016), other data suggests the necessity of DNA methylation and associated methyltransferases to maintain enhancer integrity and functionality (Rinaldi et al., 2016). DNA methylation is known to be dysregulated in malignancies with associated genome wide hypo and promoter associated hyper methylation, this coupled with the reversibility of this mark, makes the alteration of DNA methylation an attractive approach for the treatment of human cancer (Baylin, Jones, 2016).

2.2 DNA Methyltransferases (DNMTs)

DNA methyltransferases are comprised of 4 major isoforms: DNMT1, DNM3a, DNMT3b, DNMT3L. The maintenance methyltransferase DNMT1 is required to maintain DNA methylation of sites during cellular replication. DNMT3a,3b are the de novo methyltransferases and can methylate regions of DNA which are unmethylated or as a proof reading methyltransferase (Baylin, Jones, 2016). Additionally, this mechanism of de novo methyltransferase activity is key to stably silencing of recently incorporated viral

DNA (Meilinger et al., 2009). Recent data suggests the de novo methyltransferases may be required for the maintenance of enhancer stability (Rinaldi et al., 2016). DNMT3L has no known enzymatic functionality but is known to increase the processivity and thus the activity of DNMT3a facilitated methylation of DNA (Holz-Schietinger et al., 2010) The inhibition of this group of enzymes has formed the backbone of clinically relevant epigenetic therapy.

2.3 DNMT Inhibitors

Three sequence non-specific DNMT inhibitors (Azacitidine, Decitabine, and Guadecitabine) are either FDA approved or in phase III clinical trials for hematological malignancies. Azacitidine incorporates into both DNA and RNA, while Decitabine and Guadecitabine are DNA only incorporators. (Jones et al., 2016). The original application of DNMT inhibitors used high doses of these agents and were largely unsuccessful (Derissen et al., 2013). The mechanism of action for these agents is the stable incorporation of these cytidine analogues into the DNA. DNA methyltransferases then interact with these incorporated cytidine analogues forming a covalent bond between analogue and enzyme. This leads to the degradation of the enzyme and the formation of an abasic site in the genome requiring DNA repair (Stresemann et al., 2008). The degradation of DNMTs facilitates the demethylation of the genome either through replication dependent DNA demethylation (passive demethylation) or TET mediated DNA demethylation (active demethylation) (Chan et al., 2003). Canonically speaking the activity of DNMTis was thought to be mediated through the reactivation of tumor suppressor genes. However emerging data, including the work in this dissertation, suggests the activity of these agents extends well beyond this spectrum of genes.

3. Histone: Acetylation, Acetyltransferase (HATs), Deacetylases (HDACs), and HDAC inhibitors

3.1 Histone Deacetylases and Nuclear Repressive Complexes

As stated above, disregulation of epigenetic regulation of gene expression is a hallmark of cancer. Aberrant silencing of important tumor suppressor or other growth regulatory genes by the combination of hypoacetylation and hypermethylation of promoter regions results in loss of normal growth control. As such, the histone acetylation state is a critical determinant in the transcriptional regulation of important growth regulatory genes, and thus HDACs are interesting drug targets that have the potential to reactivate aberrantly silenced genes in cancer.

3.2 Histone Acetylation

Histone acetylation is an active process regulated by both the relative abundance and localization of histone acetyltransferases (HATs) and nuclear-localized histone deacetylases (Ropero et al., 2007). The post-translational modification of acetylation is extremely dynamic with a half-life of less than 15 minutes for all modified histones; this necessitates continual maintenance of the mark (Barth et al., 2010). Protein acetylation induces charge neutralization of histone lysine tails, inducing dissociation of the tails from the negatively charged DNA phosphodiester backbone. This removes steric hindrance for transcription factor association, thus creating a transcriptionally permissive state at a specified locus (Ropero et al, 2007).

3.3 Histone Deacetylases (HDACs)

HDACs, or histone deacetylase, enzymes are classified based on cellular localization and cofactor dependence. The predominant function of this enzyme class is to act as an eraser of one of the marks in the histone code; specifically, the removal of an acetyl moiety from lysines in histone tails. Specifically, some of the HDACs do function as scaffolds and readers of the histone code. Thus far, 18 HDACs have been identified to date, with 11 HDACs comprising the classical zinc-dependent HDACs, and the remaining 7 being the class III NAD-dependent Sirtuins (SIRT 1-7). The presence or lack of a nuclear localization signal is critical for determining the cellular distribution of the classical zinc-dependent deacetylases. These HDACs are subcategorized into 3 distinct classes: Class I, Class II and Class IV (Witt, Deubzer, Milde, & Oehme, 2009), (Ropero & Esteller, 2007),(Falkenberg & Johnstone, 2014).

Table 1: HDAC Isoforms

HDAC Class	HDAC Isoforms											Cellular Localization	Expression	Reader or Eraser
	1	2	3	4	5	6	7	8	9	10	11			
Class I	X	X	X					X				Nuclear	Constitutive	Eraser
Class IIa				X	X		X		X			Nuc./Cyto.	Tissue Specific	Reader
Class IIb						X				X		Nuc./Cyto.	Tissue Specific	Eraser
Class IV											X	Nuc./Cyto.	Unk.	Eraser

Class I HDACs

Class I HDACs are predominantly nuclear localized, consisting of HDACs 1, 2, 3, and 8 (Table 1). Class I HDACs have near ubiquitous expression across many disparate cell linages (Witt et al., 2009) (Falkenberg & Johnstone, 2014). HDACs 1 and 2 are key in terms of histone acetylation regulation as these HDACs form the catalytic core of multiple corepressor complexes (Bantscheff et al., 2011). These complexes recognize methylated CpG DNA through the presence of methyl binding domain proteins such as MeCP2 and MBD2 and facilitate the localization of these complexes to areas of CpG island methylation in the genome (Denslow & Wade, 2007; Ebert et al., 2013). HDAC3, another critical regulator of histone acetylation, can translocate between the nuclear and cytoplasmic compartment, with the primary site of action being the nuclear compartment. This HDAC isoform must associate with the NCoR complex to attain a catalytically permissive conformation, free of repressive chaperones (Codina et al., 2005; Guenther, Barak, & Lazar, 2001). HDAC8 has lower enzymatic function, relative to other Class I isoforms, but has been implicated in the acetylation of both histone and non-histone substrates (Witt et al., 2009). Overexpression of Class I HDAC isoforms 1, 2, and 3 have been detected in a wide range of malignancies including prostate, gastric and colon cancers. This overexpression is correlated with p21 downregulation resulting in dysregulation of the cell cycle (Glozak & Seto, 2007). Critical to the epigenetic therapy focus of this review, is the link of HDAC's 1 and 2 to the DNA methylation processes discussed earlier above. These two proteins, as mentioned earlier and further below, bind to the DNMT's as well as to key complexes that interact with DNA methylation such as the MBD's, the SIN transcription repression complexes, and the NURD complex, among others (Rountree et al., 2000, Fuks, et al., 2003, O'Hagan et al., 2008 , Deaton & Bird, 2011, (Ahuja et al., 2014; Cai et al., 2014; O'Hagan et al., 2008, Xia et al., 2017)

Class II HDACs

Class II HDACs function more in terms of non-histone substrate modification and display tissue specificity in terms of expression (Verdin, Dequiedt, & Kasler, 2003). Class II HDACs are further subsetted into two broad categories: Class IIa and Class IIb (Table 1). Both of these subclasses are zinc dependent and thus subcategorization is based more on enzyme activity and the presence of a nuclear localization signal (Witt et al., 2009) (Falkenberg & Johnstone, 2014). Class IIa HDACs, HDACs 4, 5, 7, and 9, have low enzymatic activity and act more as readers of acetylated lysine tails and scaffolding than erasers (Bradner et al., 2010). Class IIa HDACs do contain a nuclear localization signal, allowing these enzymes to shuttle between the nuclear and cytoplasmic compartments. Class IIb HDACs, HDACs 6 and 10, actively deacetylate non-histone substrates and act to augment protein stability and activation status. This class of enzymes lacks a nuclear localization signal and is strictly comprised of cytoplasmic deacetylases (Verdin et al., 2003) (Falkenberg & Johnstone, 2014). HDAC6 is a critical regulator of the unfolded protein response: in this context, HDAC6 deacetylates HSP90 and HSP70, allowing for binding of ATP and target proteins (R. Rao et al., 2010). The overexpression of HDAC6 has been demonstrated in a wide range of cancers including osteosarcoma, AML and ovarian cancers (Glozak & Seto, 2007); (Aldana-Masangkay & Sakamoto, 2011). Additionally, it was elucidated in a study by Lee *et al.* that HDAC6 is a critical determinant of anchorage-independent growth of RAS-transformed MEF cells, implicating a crucial role for this HDAC in RAS mediated tumorigenesis (Y. S. Lee et al., 2008).

Class IV HDAC

The Class IV HDAC, HDAC11 is a zinc-dependent histone deacetylase whose function is largely unknown. Sharing significant homology with both Class I and Class II HDACs, HDAC11 does not possess a nuclear localization signal and is thought to act more as a cytoplasmic HDAC (Table 1) (Ropero & Esteller, 2007; Witt et al., 2009).

4. Nuclear repressive complexes

4.1 NuRD Complex: a link between DNA methylation, histone deacetylation and nucleosome remodeling.

As discussed in the Introduction, the Nucleosome Remodeling and Deacetylase complex or NuRD nuclear repressive complex provides a link between DNA methylation, histone deacetylation and nucleosome remodeling. The interaction of this complex may have very special connections to the gene silencing associated with DNA methylation and HDACs and for strategies to target abnormalities involving these proteins in cancer (Cai et al., 2014). Table 2 provides a summary of the study by Bantscheff et al., 2011 which elucidated NuRD complex associated chromatin modifiers. The NuRD complex contains the core enzymatic components of an HDAC1:HDAC2 dimer, which facilitates the deacetylase function of the complex (Bantscheff et al., 2011). One of its main components, CHD4 is upstream in a DNA damage response for recruiting DNMT's, HDAC's and other proteins involved with transcription repressive functions to promoters of genes to help initiate and maintain abnormal DNA methylation and gene silencing (Xia et al., 2017) functions. Nucleosome remodeling is enabled by the presence of 2 Mi-2 proteins: CHD3 and CHD4. These SWI/SNF family ATPases compact nucleosome structure. Localization of the complex is permitted by the presence of methyl CpG island binding proteins MBD2 and MBD3, with only MBD2 possessing the functionality of methylated DNA recognition (Denslow & Wade, 2007). The NuRD complex provides a direct mechanistic link between DNA methylation and alteration of chromatin structure at the level of histone modification and nucleosome remodeling (Wong, Guo, & Zhang, 2014). This model predicts NuRD complex recognition of 5-methylcytosines of the DNA through interaction of the complex at the level of MBD2 proteins; after this localization, deacetylation of histones and nucleosome remodeling will facilitate acquisition of the transcriptionally repressive state (Figure 2). The NuRD complex, in conjunction with DNA methylation, has demonstrated the propensity to act as a repressive complex in colorectal cancer, facilitating the stable repression of tumor suppressor genes such as SFRPs 1, 2, and 5 in human colorectal cancer cell lines (Cai et al., 2014)

Figure 2: NuRD repressive nuclear complex

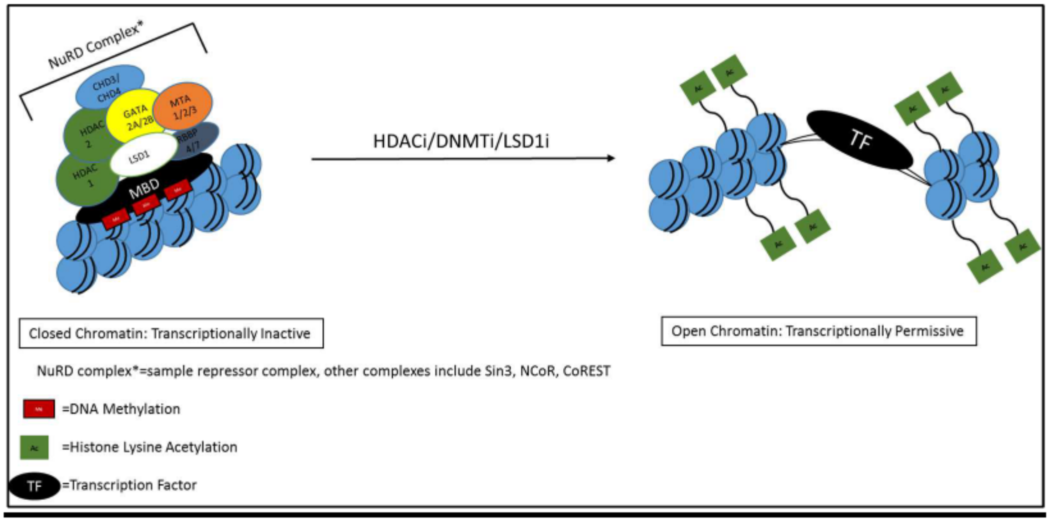

4.2 NCoR and SMRT Corepressor Complex

The Nuclear receptor Corepressor (NCoR) and Silencing Mediator for Retinoid and Thyroid receptors (SMRT) corepressor complexes are critical transcriptional repressors of nuclear receptors (Wong et al., 2014). This complex interacts with multiple deacetylases including HDACs 3, 4, 5, and 7. With regard to deacetylase activity, HDAC3 has the highest functionality in this repressor complex, owing to its higher intrinsic enzymatic capacity (Bradner et al., 2010). Prior to interaction with the repressor complex, HDAC3 is inactive enzymatically due to occlusion of the enzyme active site by two protein chaperones: Hsc70 and TRiC. The DAD domain of the NCoR-SMRT complex binds HDAC3 at the N terminus, facilitating a conformational change at the C terminus. This conformational change expels the protein chaperones from the active site, thus activating the HDAC3 enzyme. (W. M. Yang, Tsai, Wen, Fejer, & Seto, 2002) (J. Zhang, Kalkum, Chait, & Roeder, 2002) (Codina et al., 2005) (Perissi, Jepsen, Glass, & Rosenfeld, 2010). In promyelocytic leukemia (PML) specifically, it has been demonstrated that NCoR occupancy of the retinoic acid (RA) promoter reduces the transcriptional induction of RA responsive genes; these cancers are thus immune to the differentiation effects of RA. This provides direct evidence of aberrant transcriptional regulation by NCoR in driving PML leukemia carcinogenesis (Wong et al., 2014). MeCP2, a CpG methylation recognition protein, provides a direct link between the NCoR-SMRT complexes and DNA methylation. A study by Ebert *et al*. 2013, found the ablation of the interaction between NCoR and MeCP2 reduced the ability of the methyl binding protein to repress transcription (Ebert et al., 2013). The presence of this CpG recognition protein is critical to recruit the NCoR-SMRT complex to methylated CpG regions to instill repressive chromatin architecture at methylated loci.

4.3 Corepressor of RE1-Silencing Transcription factor (CoREST) Repressor Complex

The CoREST complex is a functional deacetylase and demethylase complex whose activity is facilitated by the interaction of lysine-specific demethylase 1 (LSD1) (See histone demethylation section below) with an HDAC1:HDAC2 dimer (Table 2) (Bantscheff et al., 2011). DNA binding and recognition by the CoREST complex is enabled by the SANT2 domain of CoREST (Boyer et al., 2002). In this model, the SANT2 domain binds the complex to the DNA, and the HDAC1:HDAC2 components of the complex create hypoacetylated nucleosomes upstream of LSD1. This facilitates substrate recognition by LSD1, which imparts demethylation of H3K4. Furthermore, the association of LSD1 (see below) with the CoREST complex protects the protein from degradative processes (Forneris, Binda, Adamo, Battaglioli, & Mattevi, 2007; Foster et al., 2010; M. Yang et al., 2006).

The downregulation of E-cadherin is considered an early step in tumorigenesis and a potent mediator of the epithelial-to-mesenchymal transition. In a study by Cowger et al., a critical role for the CoREST complex was discovered in the facilitation of E-cadherin transcriptional repression, thus identifying a direct role for this complex in carcinogenesis (Cowger, Zhao, Isovic, & Torchia, 2007).

H3K4 methylation provides a mechanistic link between the CoREST complex and DNA methylation. The presence of the H3K4me3 mark has been demonstrated to act as a block for DNMT3L association, while the lack of H3K4 methylation is permissive for the association of DNMT3a/b/l (Rose & Klose, 2014). In line with this, a study by Lu et al. elucidated that after a transient exposure to DNA methyltransferase inhibitors, knockdown of CoREST complex components prevents the remethylation of the MLH1 promoter (Y. Lu, Wajapeyee, Turker, & Glazer, 2014). This demonstrates a differing but equally important role for the corepressor complex in regulating the epigenome, where the repressor complex actively enables the occurrence of DNA methylation through the deposition of repressive chromatin marks.

Figure 3: CoREST repressive nuclear complex

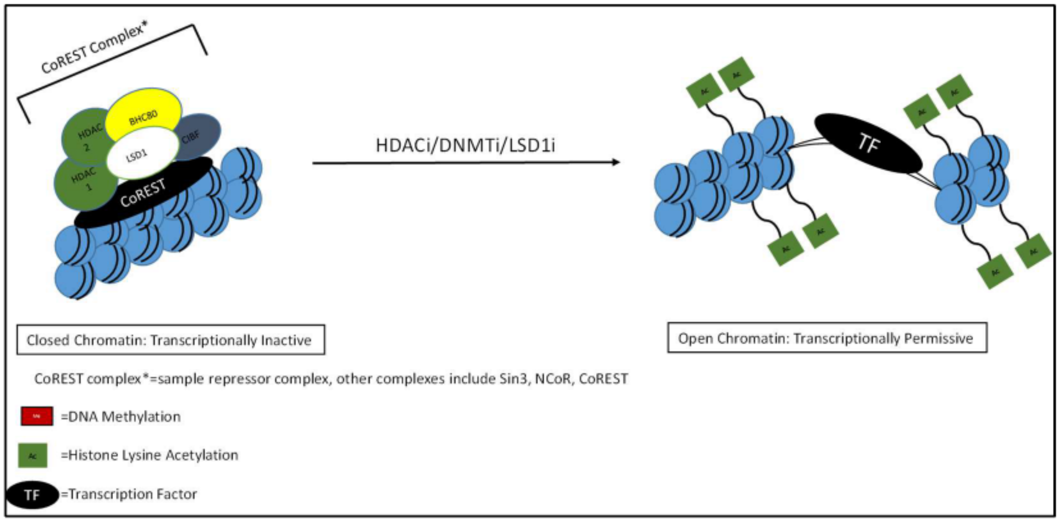

5. HDAC inhibitors

5.1 HDAC Inhibitors: General Mechanism of Zinc Chelators

Current drug development strategies for targeting the classical HDACs center on the use of reversible inhibitors to chelate zinc away from the active site of the HDAC enzyme. This disrupts the ability of the enzyme to facilitate zinc-dependent substrate coordination and nucleophilic attack by water (Lombardi, Cole, Dowling, & Christianson, 2011). The general pharmacophore of an HDAC inhibitor follows the schematic of cap-linker-chelator. Inhibitor specificity is derived from the cap, while the inhibitory functionality is based on chelation of zinc away from the active site of the deacetylase (Bantscheff et al., 2011; Bradner et al., 2010; Falkenberg & Johnstone, 2014). The general classes of HDAC inhibitors are hydroxamic acids, benzamides, cyclic peptides and aliphatic fatty acids. While the benzamides display Class I specificity in terms of inhibition, the other classes of inhibitors are broader spectrum. However, nuanced differences in isoform selectivity can be noted (Bradner et al., 2010; New, Olzscha, & La Thangue, 2012; Witt & Lindemann, 2009). Table 3 provides a summary of HDAC inhibitors with associated class and phase of clinical development.

Table 2: HDAC inhibitors and associated classifications

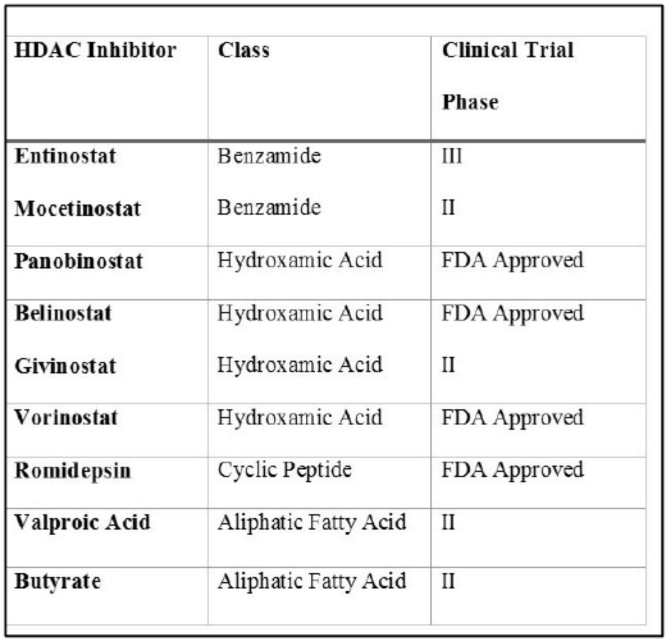

HDAC Inhibitor	Class	Clinical Trial Phase
Entinostat	Benzamide	III
Mocetinostat	Benzamide	II
Panobinostat	Hydroxamic Acid	FDA Approved
Belinostat	Hydroxamic Acid	FDA Approved
Givinostat	Hydroxamic Acid	II
Vorinostat	Hydroxamic Acid	FDA Approved
Romidepsin	Cyclic Peptide	FDA Approved
Valproic Acid	Aliphatic Fatty Acid	II
Butyrate	Aliphatic Fatty Acid	II

5.2 Mechanisms of HDAC-Induced Anti-Cancer Effects

HDAC inhibitors are pleiotropic drugs with a wide range of effects, both epigenetic- and non-epigenetic-based. HDAC inhibitors induce transcriptional changes in just 2-5% of genes, and these changes in isolation do not fully explain the drug response phenotype of cell cycle arrest and apoptosis. A well-known consequence of HDAC inhibition is the induction of p21 transcription; this cyclin-dependent kinase inhibitor has the potential to induce G1-S restriction point cell cycle arrest. p21 induction does correlate well with the often observed increase in G1 cell population after administration of high-dose HDAC inhibitors, and therefore has at least some phenotypic implications (Gui, Ngo, Xu, Richon, & Marks, 2004).

HDAC inhibitors also induce both caspase-dependent and caspase-independent cell death. Caspase 3-induced cell death is dependent on cytochrome c release, a hallmark of intrinsic apoptosis, while caspase-independent cell death is induced by autophagy (Shao et al., 2004). This cell death response has been demonstrated to be at least partly dependent on ROS production by HDAC inhibitors. In a study by Bhalla et al., a hydroxamic acid derivative HDAC inhibitor could induce a 3-fold increase in ROS with the apoptosis in this setting determined to be ROS dependent (Bhalla et al., 2009).

5.3 HDAC Inhibitor sub classifications

Hydroxamic Acid-Based Inhibitors: Vorinostat and Panobinostat

Vorinostat, or suberoylanilide hydroxamic acid (SAHA), is a hydroxamic acid-based HDAC inhibitor with FDA approval for the treatment of CTCL (Table 3) (Mann, Johnson, Cohen, Justice, & Pazdur, 2007; Mann, Johnson, He, et al., 2007). Vorinostat displays a broad of spectrum of HDAC isoform inhibition, with Ki values measuring in the low nanomolar range for HDACs 1, 2, 3 and 6, a Ki of 480 nM for HDAC8 and a Ki of 3.6 uM for HDAC4; no measurable inhibition could be ascertained for the remaining HDACs (Bradner et al., 2010). Vorinostat is dosed at 400 mg daily for the treatment of CTCL patients who have failed two prior systemic therapies. A phase II trial in refractory CTCL patients noted a 31% response rate to Vorinostat (Mann, Johnson, Cohen, et al., 2007;

Mann, Johnson, He, et al., 2007). Panobinostat is a very potent, broad-spectrum hydroxamic acid HDAC inhibitor, displaying Ki values in the low nanomolar and picomolar range for HDACs 1, 2, 3 and 6. Relatively high potency was also noted for HDACs 4, 5 and 8, with Ki measurements of 550 nM, 80 nM and 105 nM, respectively (Bradner et al., 2010). Panobinostat has been deployed clinically in combination with the proteasome inhibitor Bortezomib, resulting in noted drug synergy. The mechanism of this synergy is based upon HDAC6-mediated deacetylation of HSP90 and the subsequent augmentation of the unfolded protein response (R. Rao et al., 2010). The perturbation of this unfolded protein response is most acutely toxic in the immunoglobulin-secreting environment of multiple myeloma. In the PANORAMA trial, the combination of Panobinostat + Bortezomib + Dexamethasone resulted in an increase of progression-free survival from 8.1 months in the Bortezomib + Dexamethasone group to 12 months in refractory myeloma patients (Richardson et al., 2016; San-Miguel et al., 2013).

The FDA has granted accelerated approval to another hydroxamic acid derivative, Belinostat, (Table 3) for the treatment of relapsed or refractory Peripheral T Cell Lymphoma, based on the results of a phase II trial (H. Z. Lee et al., 2015). The FDA mandates that a phase III trial be conducted to explore Belinostat in combination with Cyclophosphamide, Hydroxydaunorubicin, Oncovin, and Prednisone (CHOP) vs. CHOP alone as a part of this accelerated approval.

Thus far, histone deacetylase inhibitors have demonstrated much promise for the treatment of hematological malignancies, but the results in solid malignancies have been disappointing to date.

Benzamide-based HDAC Inhibitor: Entinostat

An exception to the lack of efficacy, to date, for HDAC inhibitors in solid tumors may be Entinostat, which is gaining traction for the treatment of solid malignancies. Entinostat, or MS275, a benzamide-based HDAC inhibitor, has received breakthrough therapy status for advanced ER+ breast cancer and has been deployed clinically for a wide range of malignancies (Table 3). As a benzamide-based inhibitor, Entinostat displays selective inhibition of class I HDACs with K_is for HDACs 1 and 3 of 22 nM and 360 nM, respectively (Bradner et al., 2010). In a phase II clinical trial which compared the efficacy of 25 mg Exemestane daily with placebo or 5mg Entinostat weekly in ER+ breast cancer, the addition of Entinostat led to a significant increase in progression-free survival and overall survival (Yardley et al., 2013).

Cyclic Tetra Peptide-based Inhibitor: Romidepsin

Romidepsin, or FK228, is a cyclic tetrapeptide-based HDAC inhibitor with FDA approval for the treatment of CTCL and Peripheral T Cell Lymphoma (PTCL) (Table 3). The FDA recommended dose and schedule is 14 mg/m2 IV on days 1, 8 and 15 of a 28-day schedule. A phase II trial noted an overall response rate of 34%, with a durable response of 13-15 months in refractory CTCL patients (S. F. Jones et al., 2012; M. Kim, Thompson, Wenger, & O'Bryant, 2012). Romidepsin is a very potent HDAC inhibitor with biochemical Ki’s in the picomolar range for all class I HDACs. High potency was also noted against HDACs 4 and 6, with Ki’s of 20.5 nM and 9.5 nM, respectively (Bradner et al., 2010).

5.4 Biomarkers of Response to HDAC Inhibition and Prognostic Indications

The search for prognostic indicators of histone deacetylase inhibitor activity and patient response has been thus far rather difficult. The canonical and most deployed marker of histone deacetylase inhibitor activity is augmentation of histone acetylation status; while potentially useful, it has been shown to not correlate with response to the therapeutic (Prince, Bishton, & Harrison, 2009). The induction of p21 has also been deployed as a marker of drug activity, due to its near ubiquitous induction in the presence of histone deacetylase inhibition (Stimson & La Thangue, 2009). But like acetylation augmentation, p21 induction is not always correlated with response.

A potential prognostic indicator for response to histone deacetylase inhibitors may lie in the detection of a deregulated proteasome pathway. In a study by Fotheringham et al., a genome-wide loss-of-function screen in U2OS cells identified HR23B, a ubiquitin domain-containing protein, as a predictive biomarker for HDAC inhibitor response. Specifically, protein levels of HR23B were found to correlate directly with the sensitivity of cells to undergo HDAC inhibitor induced apoptosis, in this setting. Additionally, in a later study by Kim et al., this same marker was found to drive sensitivity of CTCL to HDAC inhibitors in clinical samples with a positive predictive value of 71.7% noted between HR23B protein abundance, as discerned by immunostaining of CTCL biopsies, and sensitivity to SAHA (Fotheringham et al., 2009; Khan et al., 2010).

In summary, although the precise mechanisms by which HDAC inhibitors interfere with tumor growth have not yet been fully elucidated, encouraging clinical results in specific cancers with multiple classes of these inhibitors suggest a promising future for their use. Future studies must elucidate HDAC inhibitor sensitivity biomarkers to more accurately target patients for HDAC inhibitor-based therapies. Furthermore, the question of which HDACs should be inhibited and what schedule of drug should be used remains open and most likely will be mutational and lineage dependent.

6. Potential synergy between combination epigenetic therapy and immune checkpoint for the treatment of refractory, recurrent NSCLC

An early indication of the potential synergy between DNMTi, HDACi and immune checkpoint therapy was observed in a small clinical cohort of refractory, recurrent NSCLC patients (Juergens et al., 2011). In this trial of combination Azacitidine plus intermittent MS-275, 2 patients displayed effacacious responses to combination epigenetic therapy alone with durable 14 month complete response and an 8 month partial reponse noted. A total of 19 epigentically treated patients received subsequent systemic therapies and 3 of these displayed effacacious reponses to anti-PD1 therapy with a noted regression in target lesion size from 30 to 60%. While these data provided evidence that NSCLC lesions may respond to combination epigenetic and immune therapies, the derivation of how this combination truly worked or markers predictive of reponse were not elucidated.

II. NSCLC epithelial specific response to combined epigenetic therapy

1. Introduction

Identifying rational combinations to augment anti-tumor immunity and increase the response to immune checkpoint therapy represents a major challenge for the field. Durable responses were observed in patients with NSCLC who were initially treated with a DNA methyltransferase inhibitor (DNMTi) combined with intermittent histone deacetylase inhibitor (HDACi) followed by immune checkpoint therapy (Juergens et al., 2011). Combination epigenetic therapy regimens most commonly utilize DNMTi's in combination with HDACi's on the premise that the latter can enhance re-expression of abnormally silenced genes mediated by abnormal, gene promoter DNA methylation (Cameron et al., 1999; Jones et al., 2016). However, little attention has been paid to examining the specific pharmacologic features of HDACi, optimal dosing strategy, and underlying mechanisms mediating maximal synergy with DNMTi's. The zinc chelating HDACi's are comprised of 3 major classes: benzamide, hydroxamic acid, and cyclic tetrapeptides (Bradner et al., 2010; Falkenberg and Johnstone, 2014; Rasheed et al., 2007; Zahnow et al., 2016). Benzamide class HDACi's target class I HDAC isoforms, while hydroxamic acid class HDACi's target both Class I (HDACs 1,2,3) and Class IIb (HDAC6), although differences in isoform targeting can be noted (Bradner et al., 2010).

We have earlier shown that low-doses of DNMTi impart durable changes in both genome-wide DNA methylation and transcriptome while avoiding acute cytotoxicity (Tsai et al., 2012). Additionally, we and others have discovered that DNMTi's can induce an epithelial immune signature for NSCLC and other cancers (Li et al., 2014; Moreno-Bost et al., 2011; Oi et al., 2009; Weiser et al., 2001; Wrangle et al., 2013). A key mediator of this signaling, is a cytoplasmic, double stranded RNA (dsRNA) mediated interferon response induced through the activation of endogenous retrovirus (ERV) transcription (Chiappinelli et al., 2015; Roulois et al., 2015). How the distinct classes of HDACis contribute to enhancing immune therapy specifically is unknown.

Herein, testing individual HDACi's based on both their isoform specific Ki's and pharmacokinetic parameters, enabled the best pairing of these agents with Aza for achieving anti-tumor effects, which include immune responses.

2. Materials and methods

Cell lines and cell culture:

Non small cell lung cancer cell lines used in the study were obtained from ATCC. The cells were cultured in RPMI1640 media (Corning) containing FBS (Hyclone) at 10% v/v.

Cells were maintained at 37°C in the presence of 5% CO2. Cells were passaged every 3 days. Human Non Small Cell Lung Cancer cell lines: NCI-H1755 (female), NCI-H520 (male), NCI-H1650 (male), NCI-H1975 (female), NCI-H441 (male), NCI-H661 (male), NCI-H596 (male), HCC4006 (male), NCI-H1703 (male), NCI-H838 (male), NCI-H2170 (male), NCI-H1792 (male), NCI-H460 (male), NCI-H23 (male), A-549 (male), NCI-H1299 (male), HCC827 (female)

In Vivo Mouse Studies:

Xenograft studies in NOD/SCID mice :

We used male NOD-SCID mice (5-6 weeks old) for these studies. Mice were bred and housed at the Johns Hopkins Animal care facility. All animal experiments were approved by the Johns Hopkins Animal Care and Use Committee. All animal care and protocols followed were in accordance with guidelines of the institutional Animal Care and Use Committee (IACUC). Mice were injected subcutaneously in the flank with 2.0×10^5 viable cells for H1299 and 5.0×10^4

viable cells H460 cells in 0.2 mL of RPMI with Matrigel (1:1). Drug treatments were started 10 days post injection for H460 and 14 days post injection for H1299, when palpable tumors could be discerned and continued as indicated in the figure. Mice were treated with the dosing schedules shown in **(Figure 7A)**. Treatment was continued for the entire duration of the study and mice were sacrificed when tumors size exceeded 2000mm3. Tumor volume determined by measurements obtained from digital caliper and calculated as V= 0.5(LxWxH).

PDX mouse model:

A PDX mouse model (TM00302) was obtained from Jackson Laboratories. This model was derived from metastatic lung adenocarcinoma in a female patient with the following mutations KRAS ^{G12D}; KDR ^{Q472H}, TP53 ^{R158L}. The tumor was harvested from a JAX provided donor mouse mouse and sectioned into 2mm^3 fragments. These fragments were then implanted subcutaneously in the flank of male NSG mice (5-6 weeks old). Once implanted tumors were papable, mice were randomized into three treatment groups and dosed as depicted in Figure S7A. Mice were treated for the duration of the study and at culmination of treatment mice were sacrificed. Tumors were excised from the animals and weighed as a measure of disease burden.

Drug Reagents:

Azacidine (Sigma) was dissolved in PBS at 500uM (in vitro) and 7.1 mg/mL (in vivo), aliquoted, and stored at -80C for single use. ITF-2357 (Apexbio) was dissloved in DMSO to concentrations of: 1mM, 500uM, 250uM, 100uM, 50uM and 25uM (in vitro) and 50mg/mL (in vivo), aliquoted and stored at -20C. MS-275 (Syndax) was dissloved in DMSO to concentrations of: 2.5mM, 1mM, 500uM, 250uM, 125uM (in vitro) and 50mg/mL (in vivo), aliquoted and stored at -20C. MGCD0103 (Apexbio) was dissloved in DMSO to concentrations of: 1mM, 500uM, 250uM, 100uM, 50uM and 25uM (in vitro) and 10mg/mL (in vivo), aliquoted and stored at -20C. RGFP996 (Apexbio) was dissloved in DMSO to concentrations of: 10mM, 5mM, 2.5uM, 1uM, 500uM and 100uM (in vitro), aliquoted and stored at -20C. Tubastatin A (Apexbio) was dissloved in DMSO to concentrations of: 10mM, 5mM, 2.5mM, 1mM, 500uM and 250uM (in vitro), aliquoted and stored at -20C. Vorinostat (Cell signaling) was dissloved in DMSO to concentrations of 300uM (in vitro), aliquoted, and stored at -20C. Puromycin (Sigma), dissolved in PBS at 1mg/mL, aliquoted and stored -20C.

Azacitidine drug treatments:

Cell lines were plated at the following densities for Azacitidine treatments per T75 flask: : NCI-H1755 ($2.0*10^5$), NCI-H520 ($2.0*10^5$), NCI-H1650 ($2.0*10^5$), NCI-H1975 ($1.0*10^5$), NCI-H441 ($2.0*10^5$), NCI-H661 ($2.0*10^5$), NCI-H596 ($2.0*10^5$), HCC4006 ($2.0*10^5$), NCI-H1703 ($2.0*10^5$), NCI-H838 ($1.0*10^5$), NCI-H2170 ($2.0*10^5$), NCI-H1792 ($1.0*10^5$), NCI-H460 ($1.0*10^5$), NCI-H23 ($2.0*10^5$), A-549 ($1.0*10^5$), NCI-H1299 ($1.0*10^5$), HCC827 ($2.0*10^5$) .Allowed to adhere for 24 hours before the onset of treatment. Cells were treated with 500uM Azacitidine diluted 1:1000 or PBS vehicle in complete RPMI1640 media every 24 hours for the indicated treatement duration. Drug treatments with HDACi are assay specific and are detailed in the relevant sections.

Cell Viability Assays (MTS colorimetric):

Cells treated as described in Azacitidine treatment section, were trypsinized, enumerated, and assesed for viability by trypan blue exclsuion assay. Equal numbers of viable cells were plated in 96 well plates at the following densities per well, in technical triplicate: : NCI-H1755 ($2.0*10^3$), NCI-H520 ($2.0*10^3$), NCI-H1650 ($2.0*10^3$), NCI-H1975 ($1.0*10^3$), NCI-H441 ($2.0*10^3$), NCI-H661 ($2.0*10^3$), NCI-H596 ($2.0*10^3$), HCC4006 ($2.0*10^3$), NCI-H1703 ($2.0*10^3$), NCI-H838 ($1.0*10^3$), NCI-H2170 ($2.0*10^3$), NCI-H1792 ($1.0*10^3$), NCI-H460 ($1.0*10^3$), NCI-H23 ($2.0*10^3$), A-549 ($1.0*10^3$), NCI-H1299 ($1.0*10^3$), HCC827 ($2.0*10^3$) . Cells were allowed to adhere for 24 hours in the presence of complete media prior to the onset of treatment. Adhered cells were incubated with 100uL drug supplemented media every 3 days, treated with DMSO(vehicle) at .1% or the following drugs/concentrations standarized to .1% DMSO final concentration. ITF-2357: 25nM, 50nM, 100nM, 250nM, 500nM, 1uM; MGCD0103: 25nM, 50nM, 100nM, 250nM, 500nM, 1uM; RGFP996: 250nM, 500nM, 1uM, 2.5uM, 5.0uM and 10uM; Tubastatin A: 250nM, 500nM, 1uM, 2.5uM, 5.0uM and 10uM; MS-275: 125nM, 250nM, 500nM, 1uM, 2.5uM. Treatments were applied for a period of 5 days, afterwhich, MTS colorimetric assay (promega) was conducted. MTS reagent was diluted 20uL per mL in complete and vortexed to ensure the resultant solution was homogenous. Drug treated was gently removed from treated cells by multichannel pipette and replaced MTS supplemented media. Cells were incubated in 37C incubator to allow the colorietric reaction to occur. After incubation 490nm absorbance was read using the BioRad iMark microplate reader for media+MTS, vehicle treated+MTS and drug treated+MTS cells. Absorbance values were imported to Graphpad prism. Data were normalized the vehcicle treated cells for both mock and Aza treated condtion. Drug doses were log transformed. These normalized, log transformed data were analyzed by 4 parameter nonlinear regreesion to generte log dose response curves for each cell line and drug condition and determination of drug effect at dose. The resultant dose repsonse curves are a representation of these data, with the indicated biolofical replicates being a represention of the mean for each condtion. These dose response data were utlitized for drug synergy analysis (Compusyn). The fractional effect data for each drug condtion were imported for drugs both alone and in combination with Aza. These data were anayzed and used to generate combination index output as an indicator of drug synergy.

BrdU Cell Prolifertion Assay, colorimetric ELISA:

Cells were plated in technical triplicate in 96 well fomat at the densities described in the Cell viabilty section. Vehicle or Aza treated cells were allowed to adhere for 24 hrs prior to the onset of treatment. Cell were subsequently treated with the following inhibtiors for 3 days. MGCD0103: 200nM, ITF-2357: 100nM, Tubastatin A: 1uM, RGFP996: 2uM. On day 3 of treatment, Stock Brdu (Calbiochem BrdU Cell Proliferation Assay) was diluted 1:1000 in complete media and added to 100uL of drug treated media. Cells were incubated with BrdU at 37C for 5 hours to allow for DNA synthese based incorporation. The remainder of protocol was carried out as decribed in Calbiochem protocol, with the lot specifc 1:2400 dilution of secondary antibody. 450nm absorbance values derived from ELISA were measured using the Biorad iMark plate reader. The triplicate measurements per condition were imported to graphpad prism and the data background subtracted, normalized to vehicle treated control to generate the normalized proliferation. Error bars depicted as SEM between the means of experimental replicates, after computing the mean of technical triplicates. Statistical signifcance is the result of two way anova conducted between the experimental conditions depicted.

Gene expression analysis by microarray:

RNA expression were conducted by microarray for the conditions descibed in the relevant figures. The R/Bioconductor package limma was used to process expression data. Within- and between-array normalizations were performed using the loess and aquantile methods, respectively. The normexp option was used for background correction. Raw files read in using the read.maimages function. Log2 fold change in transcription for drug treated conditions over mock treated was obtained for each sample at each time point studied. Ranked lists of log2 fold change were analyzed using Gene Set Enrichment Analysis (GSEA) by the Broad Institute and data packages (Subramanian et al., 2005). Pathways enriched with a false discovery rate less than 0.25 were selected with cutoff of 2.0 normalized enrichment score in human studies. Median absolute deviation analysis of Log2 fold change transcription data were obtained using Morpheus program (Broad). Top 500 genes were selected and depicted as heatmap representative of minimum to maximum value ranking for each gene across cell lines and conditions.

DAVID analysis of median absolute deviation derived genes (KEGG Pathways):

Top 500 genes derived by median absolute deviation analysis were obtained as described in Gene expression by microarray methods section and were analyzed for KEGG Gene Ontology (GO) enrichment using the DAVID Bioinformatics resources database (Huang da et al., 2009a, b). Only categories that were below the DAVID p value of .05, and containing at least 5 genes per pathway are reported.

ERV absolute quantitative real time PCR (qPCR):

Eleven codogenic and partially codogenic ERV envelope (env) gene families (see Figure 3 and Figure S4 for ERV env genes used in this investigation), one ERV gag (ERV-W5) and two ERV pols (ERVFXA34, erv9-1) were quantified using qPCR and have been previously described (Chiappinelli et al, 2015). Additionally, some of these ERV primers could potentially hybridize with other ERV transcripts among the ERV family members, e.g. the ERV-K env primers could hybridize with 8 transcripts derived from ERV-K102 (1q22), -107 (5q33.3), -108 (7p22.1), -109 (6q14.1), -113 (19p13.11), -115 (8p23.1), -17833 (19q12), -74261 (12q14.1) according to sequence alignments (Chiappinelli et al, 2015).

The qPCR methodology detecting the ERV genes has been previously described (Chiappinelli et al, 2015). Briefly, ERV genes were amplified by qPCR from 40 ng of cell line cDNA with SYBR-green technology and then analyzed with an ABI7300 (ABI, Darmstadt, Germany). Expression values were calculated as molecules per ng total RNA using a standard curve of each cloned gene determined by real time PCR and calculated as mean +/- SEM. TBP and beta-actin were used as housekeeping genes where a mean from both genes was used for normalization of NSCLC cell lines.

IFNα/β qPCR:

qPCR methodology for detecting IFNα/β related genes (ISG15, OASL1, HLA-A, HLA-B) differential expression was conducted on 20ng of cell line cDNA with SYBR green technology. Expression values were calculated as fold change over mock by delta-delta ct. Beta-actin was used as housekeeping gene for normalization of NSCLC cell line expression.

Taqman microfluidic genecard:

1ug of total RNA was used for cDNA reaction and diluted to 50uL total volume in molecular grade water. Diluted cDNA was combined with 50uL of Taqman universal PCR mastermix and loaded onto a Taqman microfludic genecard with the following primer/probe sets preloaded: IRF7, IFI27, STAT1, IFNB1, MX1, OASL, IFI6, beta actin, TBP. Expression values were calculated as fold change over mock by delta-delta ct. Beta actin and TBP were used as housekeeping genes for normalization of NSCLC cell line expression.

Immunoblotting:

Protein was extracted by 4% SDS mediated lysis, followed by processing of lysates through homogenizer column (Omega). Protein concentrations were estimated by BCA (Pierce Biotechnology). Lysates were processed using PAGE with 4-12% Bis-Tris BOLT gel (Life Technologies) and transferred to PVDF membrane (Millipore). Membranes were blocked in 10% milk/TBST and immunoblotted with the following antibodies.: Rabbit monoclonal anti-Acetyl α Tubulin (Cell Signaling, 1:1000), Rabbit monoclonal anti-Acetylated Histone 3 (Cell Signaling, 1:1000), Rabbit polyclonal anti-Histone H3 (Cell Signaling, 1:1000), Rabbit polyclonal anti-DNMT1 (Sigma Aldrich, 1:2000), Mouse monoclonal anti-β-Actin (Sigma Aldrich, 1:10000). The loading control antibodies (anti-β-Actin, anti-Histone H3) in all cases were applied after membrane stripping.

DNMT1 Knockdown Cell Viability Assay:

DNMT1 knockdown was initated, see refernce for sequence (Cai et al., 2017) and control vector shGFP 5′- GCAAGCTGACCCTGAAGTTCAT3-3′. Clonal selection was initated with puromycin selection. Selected clones were plated at cell densities, treated and analyzed as described in Cell viabilty Assay section of methods. Error bars are representative of mean +/- SEM between experimental replicates.

3. Results

Combination Aza + ITF-2357 induces drug synergy when applied to human NSCLC

Selection of HDACi's was instituted by pairing these agents with low-dose (500 nM) Aza. Clinically relevant HDACi's (ITF-2357, MGCD-0103, MS-275) were selected and paired with Aza based on their known pharmacokinetic parameters (cmax and half-life) and enzymatic Ki's against key HDAC isoforms **(Table 3)** (Bradner et al., 2010; Falkenberg and Johnstone, 2014; Furlan et al., 2011; Gore et al., 2008; Rasheed et al., 2007; Ryan et al., 2005; Zahnow et al., 2016).

Table 3: PK/PD parameters of clinically relevant HDACis deployed in the current study

Compound	~cMax	~Half-life	HDAC Ki uM			
			1	2	3	6
ITF-2357	300nM	7 hrs.	.002	.003	.003	.0042
SAHA	1.0uM	1.5-2 hrs.	.0013	.0016	.005	.0016
MGCD0103	600nM	9.9 hrs.	.009	.034	.265	
MS275	50nM	105 hrs.	.022		.36	

We initially examined the effect of sequential Aza + HDACi on cell proliferation across a panel of 16 cell lines representing the diverse oncogenotypes of NSCLC (**Figures 5 and 6**). These data revealed that the antiproliferative effect of this treatment regimen correlated with the subtype and mutational status of the NSCLC cell line queried. The hydroxamic acid class HDACi (ITF-2357) in combination with Aza demonstrated the most potent antiproliferative phenotype. Among our four most responsive cell lines, three were RAS mutant subtype. Therefore, we selected these cell lines for further studies of therapeutic scheduling and HDAC isoform targeting delineation. Using a comparative analysis, wherein, Aza and ITF-2357 are both sequentially and concurrently employed (**Figure 4**), only the former schedule induces both synergy and robust potentiation of HDACi by Aza (**Figures 6 and 7**).

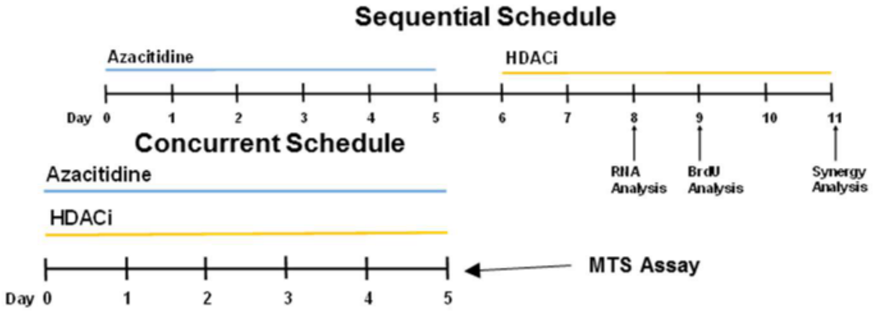

Figure 4: Concurrent and sequential Aza + HDACi treatment schemas

In vitro treatment schema for sequential and concurrent application of Aza and/or HDACi to NSCLC cell lines. **(D)** Log dose response curve of MTS data for H460 cells treated concurrently with Aza and variable concentrations of ITF-2357 (day 5, data are mean ± SEM, n=3).

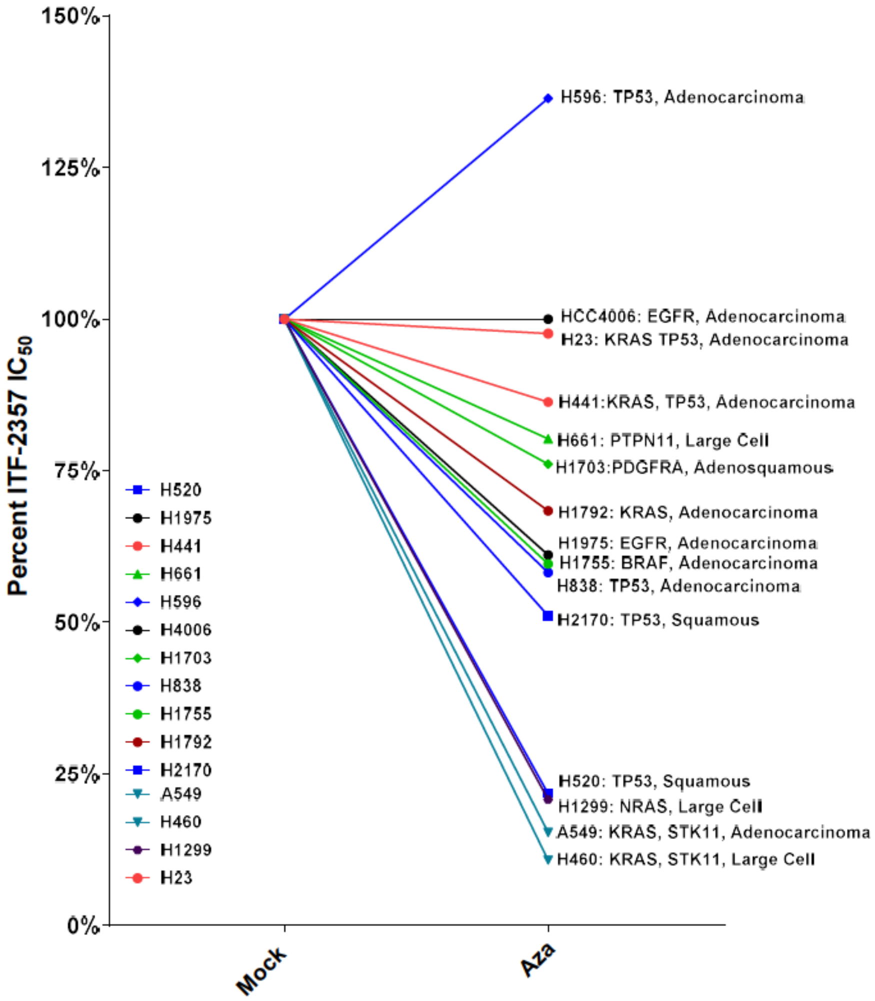

Figure 5: Composite representation of ITF-2357 IC50 through the application of sequential Aza + ITF-2357

Composite representation of ITF-2357 IC50 as determined by four parameter dose response analysis in the presence of mock or 500nM Aza pre-treatment. Individual dose response curves are in Figure 6 and 7A.

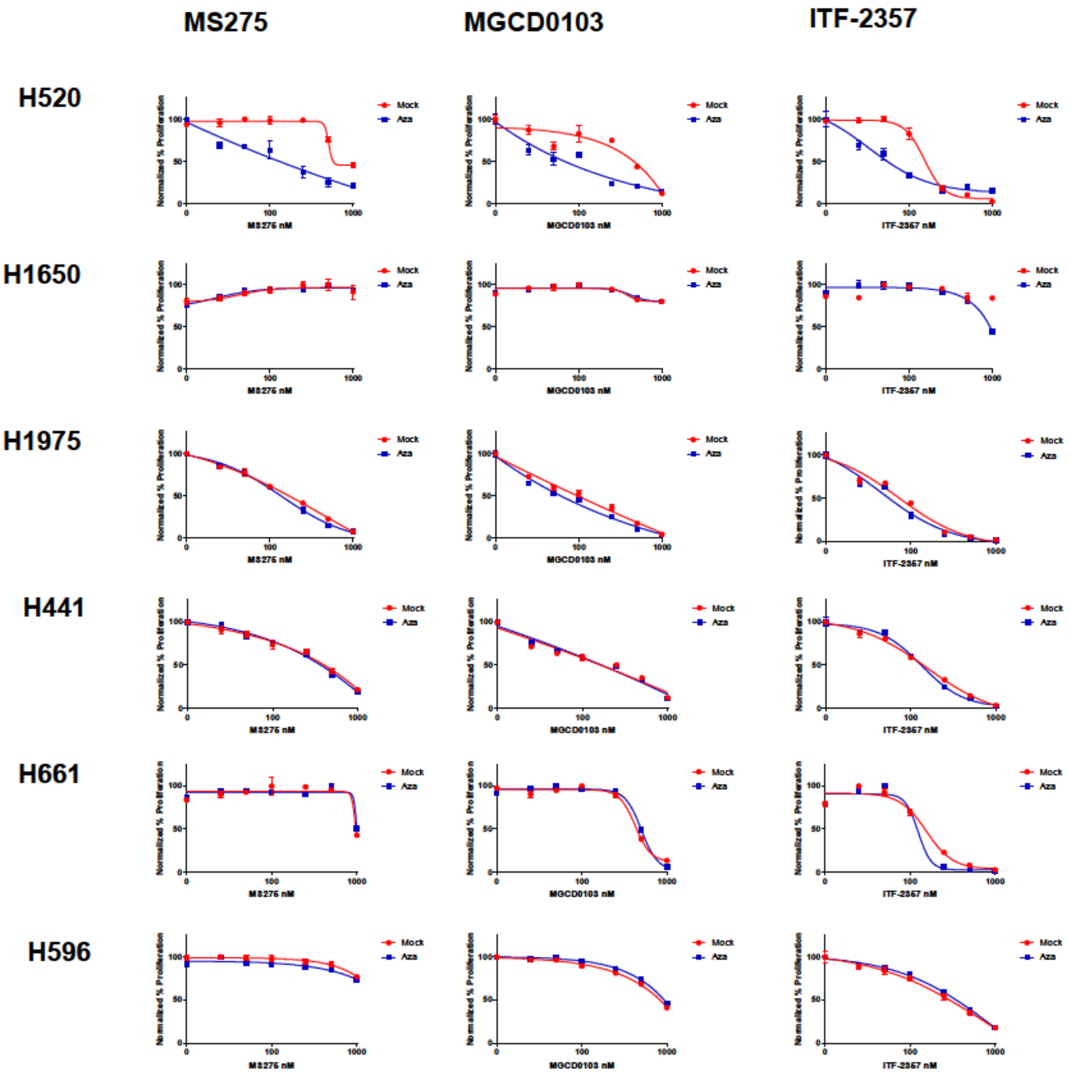
MS275
MGCD0103
ITF-2357
H520
H1650
H1975
H441
H661
H596
Normalized % Proliferation
0
50
100
0
100
1000
MS275 nM
MGCD0103 nM
ITF-2357 nM
Mock
Aza

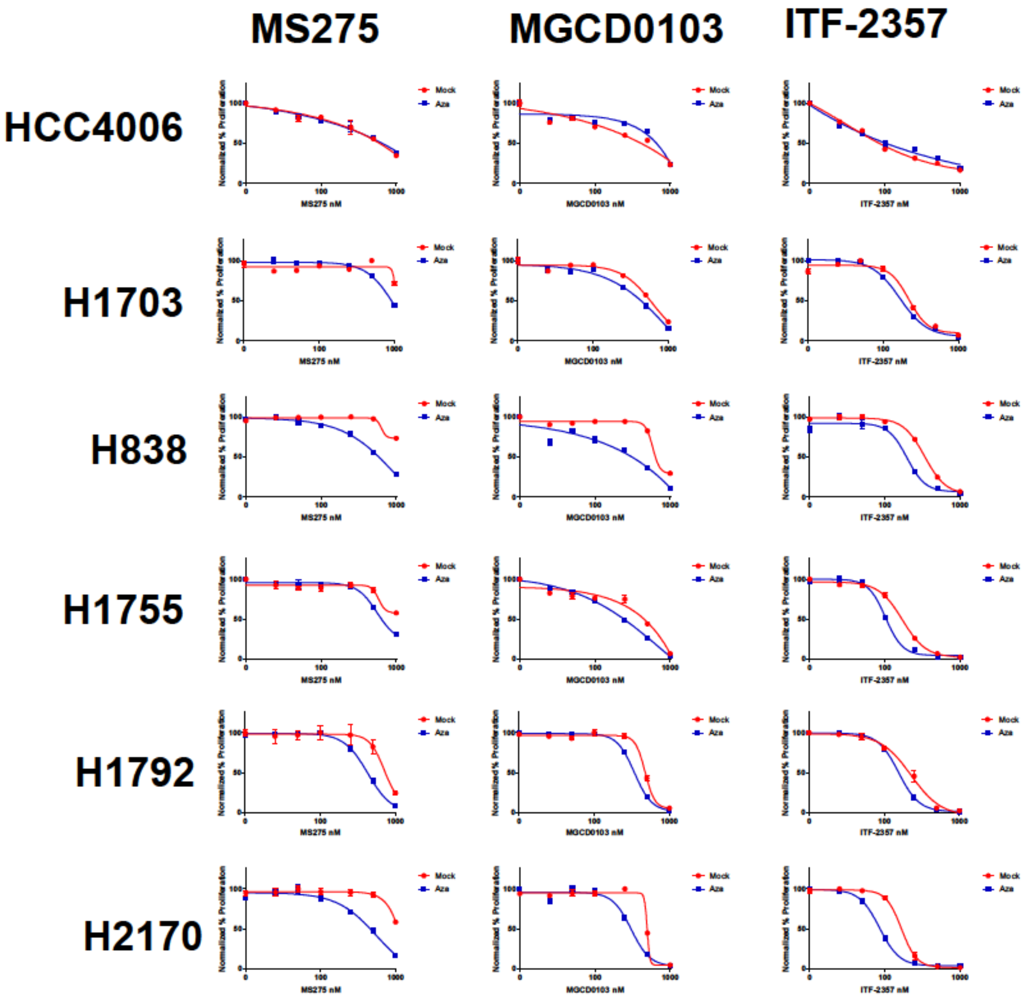

Figure 6: Sequential Aza + HDACi NSCLC cell line dose response data for benzamide and hydroxamic acid HDACis

Log dose response curves of MTS data from screen of NSCLC cell lines treated sequentially with either vehicle or 500nM Aza followed by the HDAC inhibitors indicated in the figure. (day 11, data are mean ± SD between n=3 technical replicates).

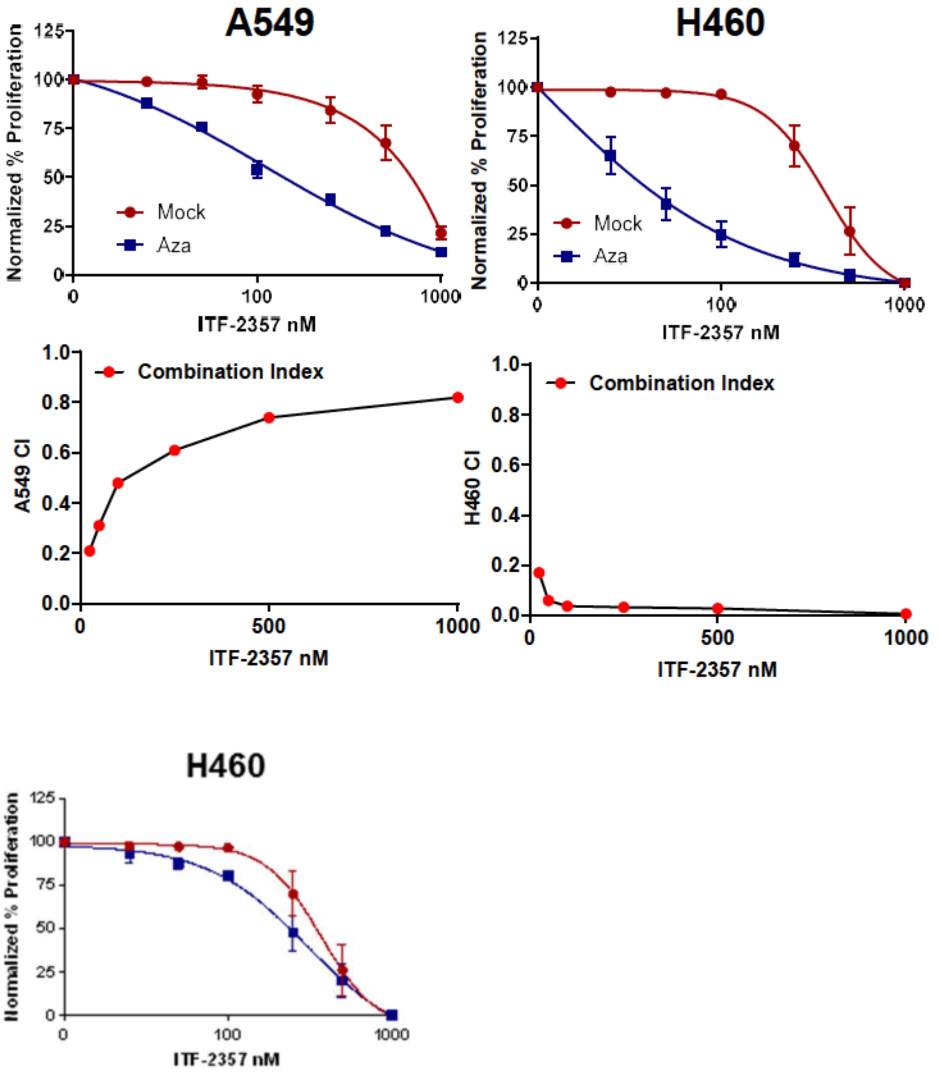

Figure 7: A549 and H460 dose response and combination index of sequential Aza + ITF-2357 in comparison to H460 concurrent Aza + ITF-2357

(A) Sequential treatment (mock or 500nM Aza) ITF-2357 log dose response curves for growth inhibition of A549 and H460 cells (day 11, n=5, Data represented as mean ± SEM). **(B)** Combination index (CI) plots for sequential application of Aza + ITF-2357 in A549 and H460 cells (n=5). **(C)** Log dose response curve of MTS data for H460 cells treated concurrently with Aza and variable concentrations of ITF-2357 (day 5, data are mean ± SEM, n=3).

We thus used this schema of sequential treatment in our further studies. To delineate the enhanced anti-proliferative effect of ITF-2357 over the others we next tested the function of the individual HDAC isoforms in the Aza priming response to HDACi. We find through the application of HDAC isoform specific inhibitors, an Aza induced priming to both class I and IIb targeting HDACis **(Figures 8 and 9)**. These data suggest the observed Aza + ITF-2357 antiproliferative phenotype to be the result of broader targeting of HDACs, including both nuclear (HDACs 1, 2, 3) and non-nuclear isoforms (HDAC 6).

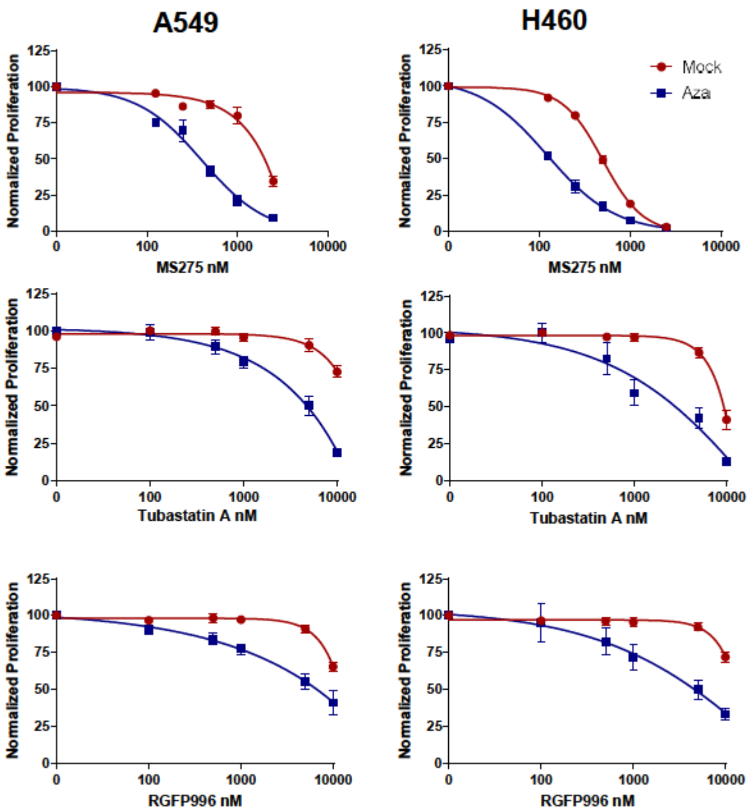

Figure 8: Aza imparts sensitization to differential isoform specific HDAC inhibitors when applied in a sequential manner

Sequential treatment (mock or 500nM Aza) MS-275, RGFP996 (HDAC3i), Tubastatin A (HDAC6i) log dose response curves for growth inhibition of A549 and H460 cells (day 11, n=3, Data represented as mean ± SEM).

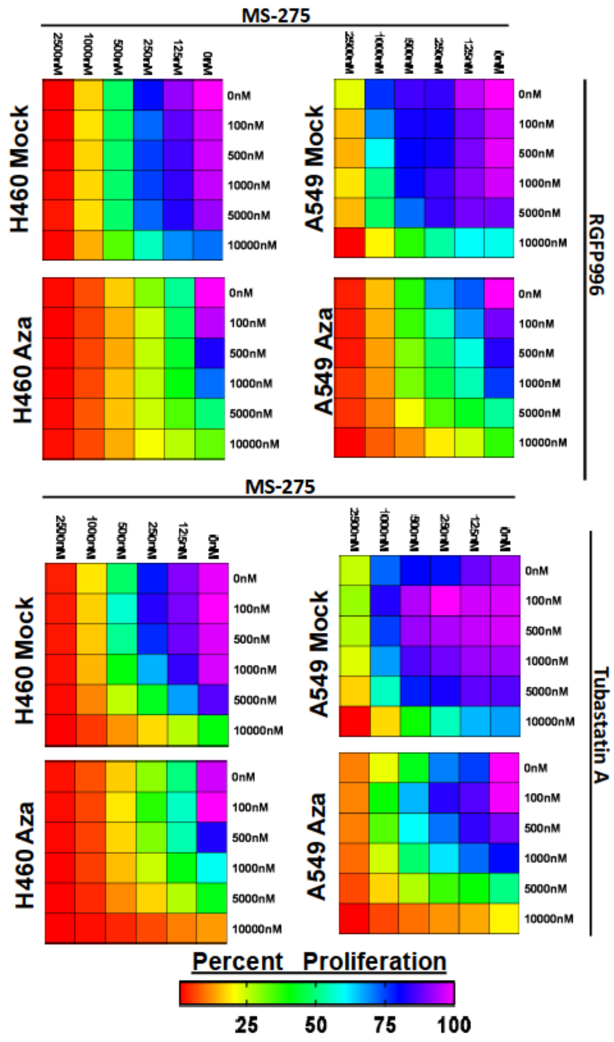

Figure 9: The application of HDAC isoform inhibitor combinations potentiates the activity of HDACis especially in Aza primed NSCLC cell lines

Sequential treatment (mock or 500nM Aza) with MS275 plus either RGFP996 or Tubastatin A drug dose response matrix for growth inhibition of A549 and H460 cells (day 11, n=3, color gradation indicates percent viability at indicated dose combination).

As a further characterization of the antiproliferative effects of Aza in combination with HDACi, we deployed equal molar concentrations of MS-275 and ITF-2357 and assessed cell proliferation specifically. In agreement with the previous data, we find 100nM ITF-2357, a concentration roughly one-third cmax, (Furlan et al., 2011) demonstrated a more robust inhibition of proliferation than 100nM MS-275 **(Figure 11A).** We next sought to define the contribution of individual HDAC isoforms to the antiproliferative effect noted from 100nM ITF-2357. To accomplish this end, we first determined equivalent doses based on isoform pharmacodynamic targets, these being, histone acetylation for HDAC1,2 and tubulin acetylation for HDAC6 (Asthana et al., 2013; Fournel et al., 2008; Khan et al., 2008). The resulting equivalent doses were 200nM MGCD0103 and 1000nM Tubastatin A to mimic 100nM ITF-2357 **(Figure 10)**. Selection of 2000nM RGFP996 for HDAC3 inhibitor was based on extrapolation of Ki, due to lack of known pharmacodynamic markers for these isoform (Malvaez et al., 2013) These normalized doses of HDAC isoform specific inhibitors identify HDACs 1, 2 and 3 as key arbiters of the Aza + ITF-2357 antiproliferative actions **(Figure 11B)**.

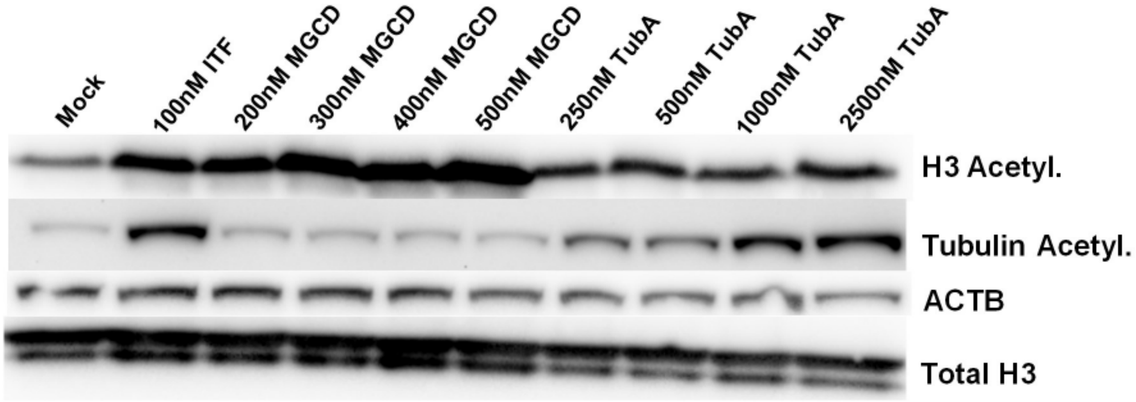

Figure 10: HDACi pharmacodynamic control immunoblot

Evaluation of pharmacologic targets of HDAC1/2: histone acetylation and for HDAC6, tubulin acetylation by immunoblotting in A549 cell line. Histone 3 and β-Actin used as loading controls. Drug and drug concentrations are indicated in the figure. (24-hour treatment, ITF= ITF-2357, MGCD= MGCD0103, TubA= Tubastatin A, n=2).

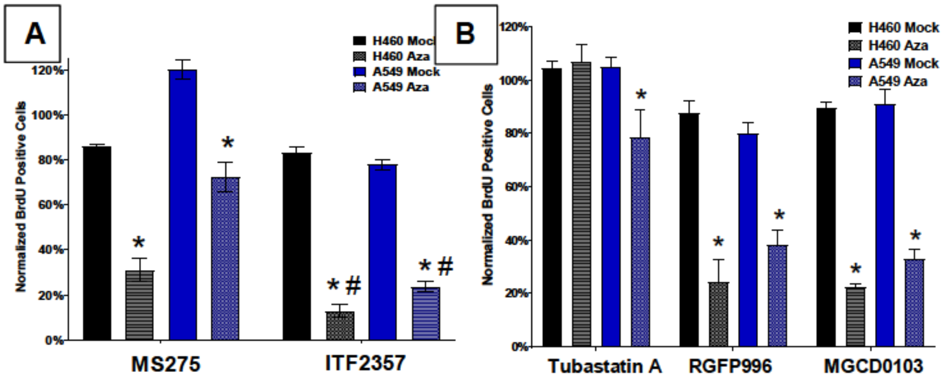

Figure 11: Nuclear HDAC isoforms elicit cell cycle inhibition in combination with Aza

(A) Normalized BrdU percent positivity for Aza +/- 100nM MS-275 or 100nM ITF-2357 (day 9, n=4 (MS-275), n=6 (ITF-2357)). Data are presented as mean ± SEM. * p value < 0.05 relative to mock, # p value < 0.05 relative to Aza + MS-275 **(B)** Normalized BrdU percent positivity for mock or Aza treated cells in combination with the indicated HDACi's (day 9, 200nM MGCD0103, 2000nM RGFP996, 1000nM Tubastatin A; data are mean ± SEM, n=6).

Additionally, to elucidate the specificity of Aza priming to HDACi we deployed shRNA mediated DNMT1 depletion, the major pharmacodynamic target of Aza (Cai et al., 2014). We observe potent augmentation of the HDACi anti proliferative effect when utilized in combination with DNMT1 depletion **(Figure 12A and 12B)**.

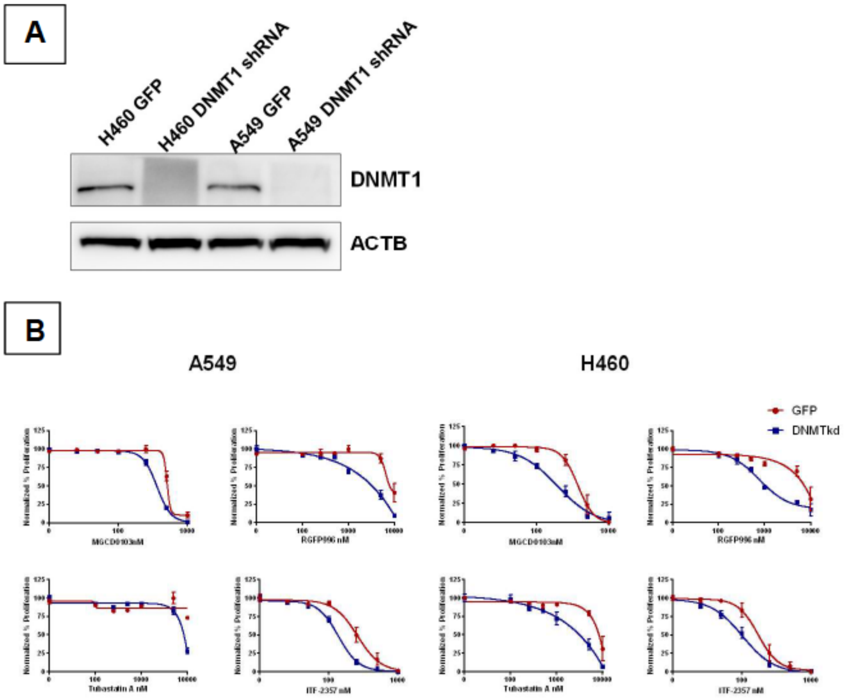

Figure 12: DNMT shRNA knockdown phenocopies Aza priming to nuclear isoform targeting HDACi

(A) Immunoblotting for DNMT1 in A549 and H460 cells infected with empty vector or shDNMT1 vector. β-Actin used as loading control (day 5, n=2) **(B)** Log dose response for A549 and H460 cells infected with empty vector or shDNMT1 vector and treated with HDACi as indicated in figure (5-day HDACi exposure, n=2)

Finally, we tested the efficacy of sequential Aza + HDACi in vivo using immune-incompetent mice. We observed significant reduction of tumor burden across 3 xenograft models, two for established NSCLC cell lines and one using a *KRAS, KDR, TP53* mutant primary patient derived xenograft (PDX) model when utilizing Aza + ITF-2357 (**Figures 13A, 13B, 13C**). The combination of Aza + MS-275 did not have significant efficacy in the H460 xenograft model, the most sensitive cell line tested, at the doses used in our study (**Figure 13A**). Aza + MGCD0103 achieved significant efficacy in H460 xenografts (**Figure 13D**) and modest efficacy in the patient derived xenograft (**Figure 13E**).

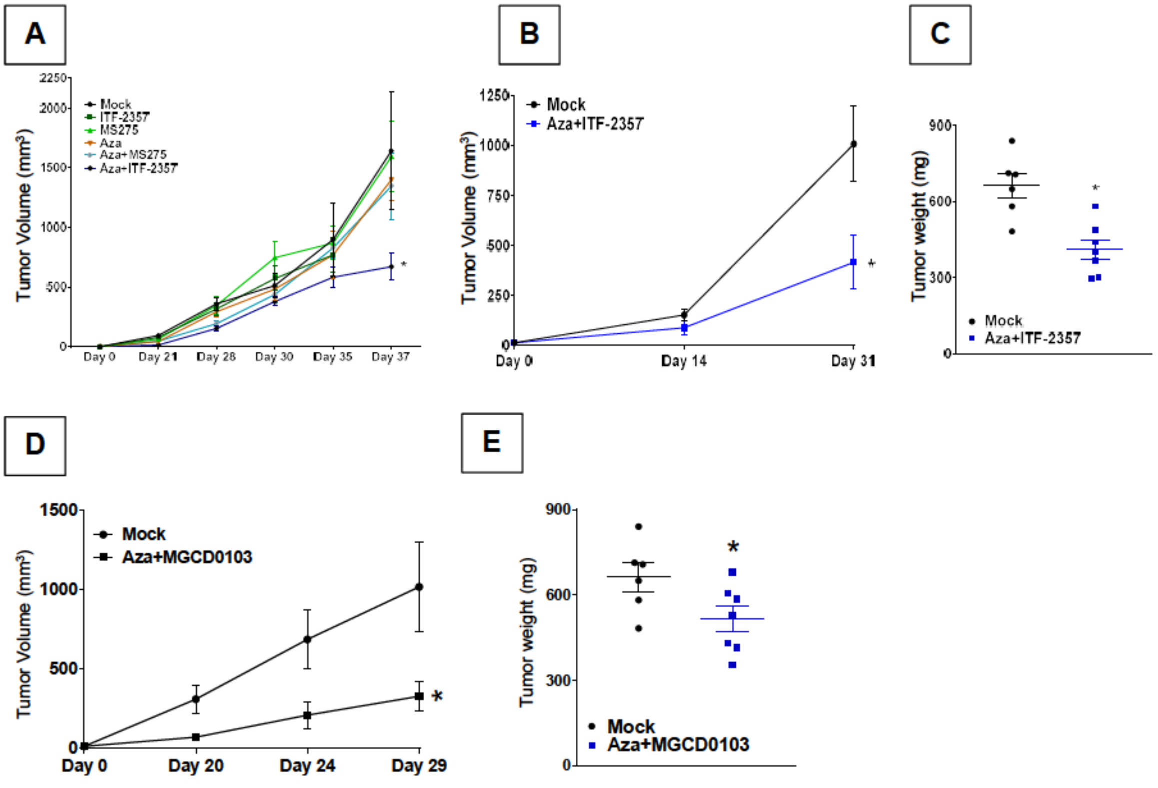

Figure 13: Combination Aza + HDACi displays efficacy in multiple NSCLC xenograft models

(**A and B**) Mean volumes of tumor xenografts obtained from NOD-SCID mice subcutaneously injected with H460 cells **(A)** or H1299 cells **(B)** and treated with the agents as indicated in the figure. (Data are presented as mean ± SEM, n=5). **(C)** Tumor weights for patient derived xenografts treated with the agents as outlined in the figure (28 days of treatment duration, data are presented as mean ± SEM, n=6 mock; n=7 Aza + ITF-2357). **(D)** Average volumes of tumor xenografts obtained from NOD-SCID mice subcutaneously injected with H460 cells (Day 0 equals onset of treatment, data are mean ± SEM, n=4 mock, n=5 Aza + MGCD0103). **(E)** Tumor weights for patient derived xenografts obtained from NSG mice and treated with the agents as outlined in the figure, mock data are also presented in Figure 1H (28 days of treatment duration, n=6 mock n=7 Aza + MGCD0103, data are mean ± SEM)

* p value< 0.05 relative to mock obtained by two tail t-test.

Effects of the drug combination paradigm on the transcriptome in NSCLC lines

Assessment of drug combination induced effects on gene expression yields important insight for signaling pathway alterations that may relate to eventual clinical efficacy. The combination epigenetic treatment induces an increase in differential gene expression relative to HDACi mono-treatment conditions, with a clear advantage noted from the application of Aza + ITF-2357 (**Figure 14A**). Clustering of top 500 differentially expressed genes shows a divergence between HDACi mono-treatment and Aza containing regimens (**Figure 14B**). DAVID pathway analysis revealed the most differentially expressed pathways to be immune, MYC and metabolism related (**Figure 14C).**

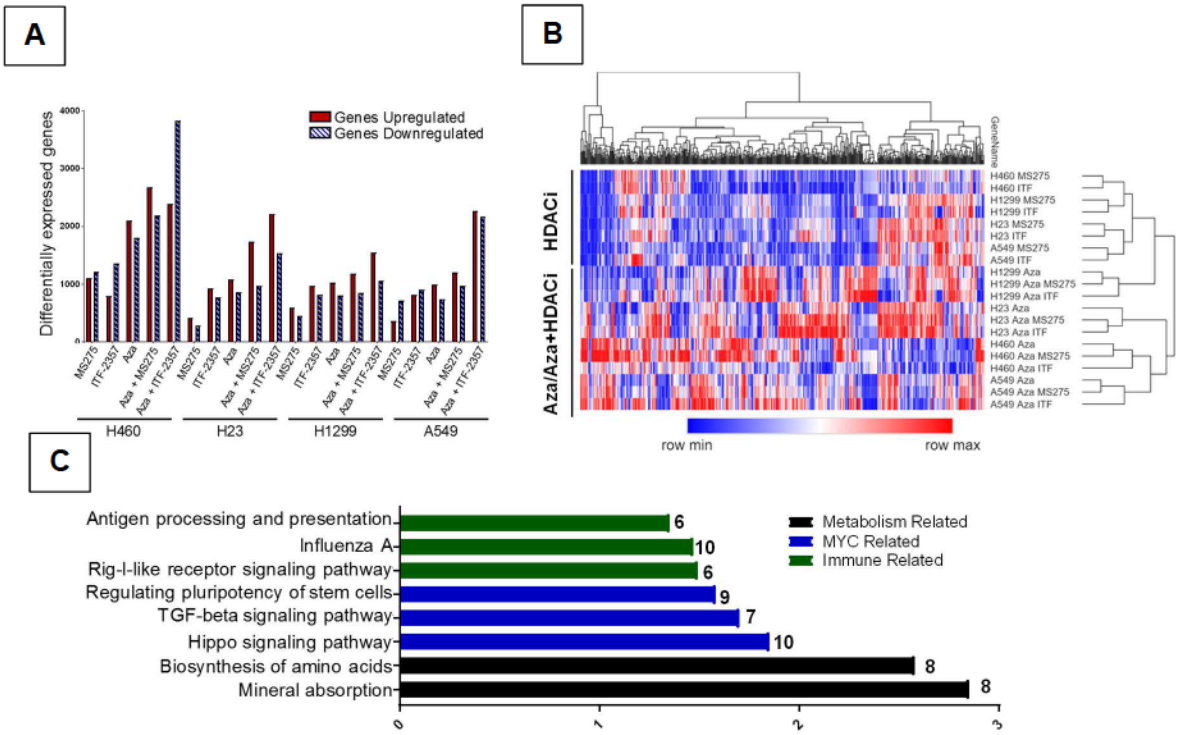

Figure 14: Combination Aza + HDACi potentiates differential gene expression over mono treatments alone, with a focus on Immune, Metabolism and MYC related genes

(A) Quantitation of differentially expressed genes (cutoff Log2 fold change over mock > 0.5) for each treatment condition. (**B)** Unsupervised hierarchical clustering of relative RNA expression by median absolute deviation (MAD). RNA expression is Log2 fold change over mock, blue to red color gradation is based on the ranking of each condition from minimum (blue) to maximum (red). The top 500 genes are depicted. **(C)** DAVID analysis of the top 500 MAD genes using KEGG gene ontology.

Above data are derived from microarray analysis of RNA from cells treated with 500nM Aza, 100nM ITF-2357, 100nM MS-275.

Gene Set Enrichment Analysis (GSEA) identified three significantly induced pathways by combination epigenetic treatment, two of which are related to immune signaling (**Figure 15A**). The interferon alpha-beta (IFNα/β) signaling pathway was the most prominent of these altered pathways (**Figure 15C**). Comparative analysis of combination epigenetic treatment downregulated pathways by GSEA revealed a conserved cell cycle repression signature across the drug combinations tested with a noted advantage for Aza + ITF-2357 (**Figure 15B**). The above transcriptional downregulation of cell cycle related pathways elicited by combinatorial epigenetic treatment matches with the observed proliferative arrest induced by combination epigenetic treatment (**Figure 15D**).

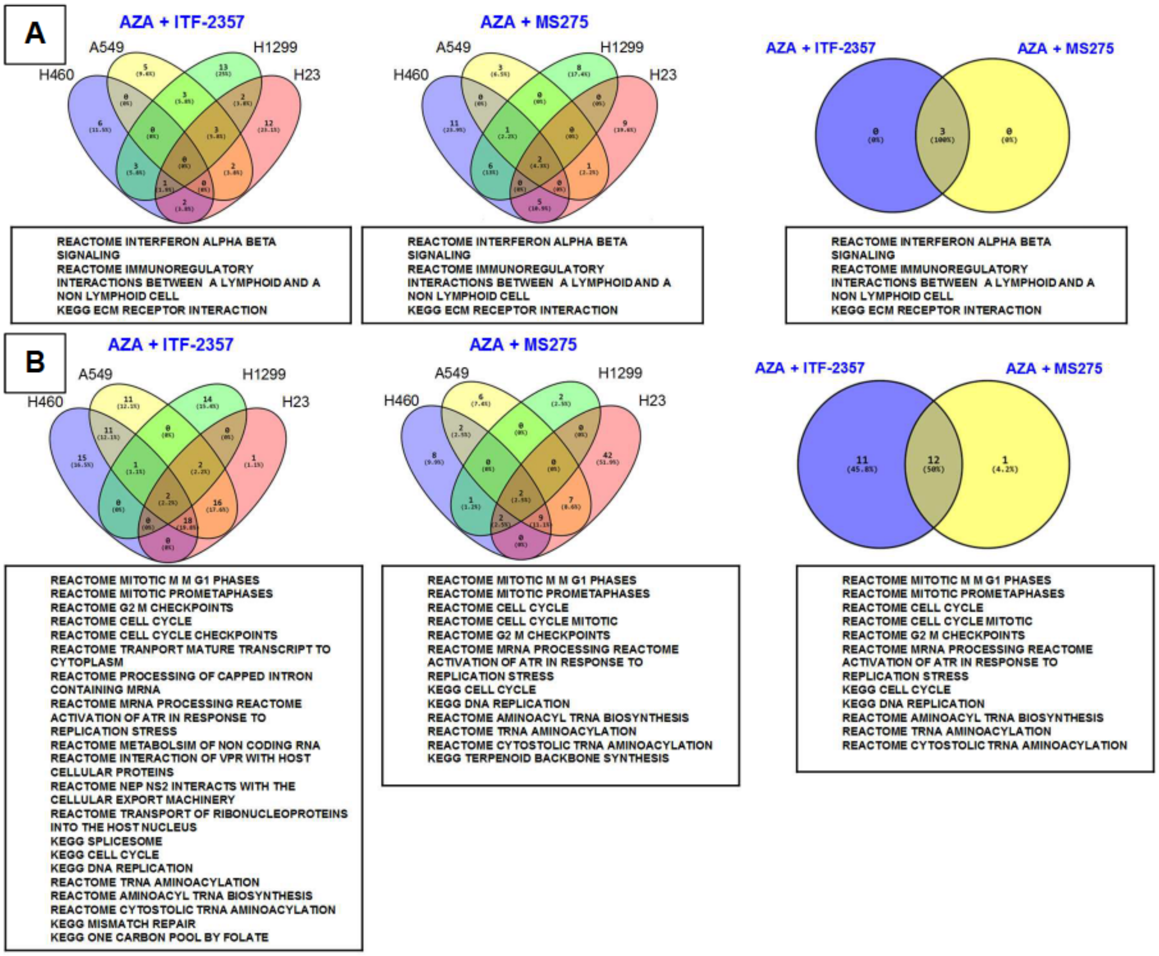

REACTOME INTERFERON ALPHA BETA SIGNALING
REACTOME IMMUNOREGULATORY INTERACTIONS BETWEEN A LYMPHOID AND A NON LYMPHOID CELL
KEGG ECM RECEPTOR INTERACTION

REACTOME INTERFERON ALPHA BETA SIGNALING
REACTOME IMMUNOREGULATORY INTERACTIONS BETWEEN A LYMPHOID AND A NON LYMPHOID CELL
KEGG ECM RECEPTOR INTERACTION

REACTOME INTERFERON ALPHA BETA SIGNALING
REACTOME IMMUNOREGULATORY INTERACTIONS BETWEEN A LYMPHOID AND A NON LYMPHOID CELL
KEGG ECM RECEPTOR INTERACTION

REACTOME MITOTIC M M G1 PHASES
REACTOME MITOTIC PROMETAPHASES
REACTOME G2 M CHECKPOINTS
REACTOME CELL CYCLE
REACTOME CELL CYCLE CHECKPOINTS
REACTOME TRANPORT MATURE TRANSCRIPT TO CYTOPLASM
REACTOME PROCESSING OF CAPPED INTRON CONTAINING MRNA
REACTOME MRNA PROCESSING REACTOME ACTIVATION OF ATR IN RESPONSE TO REPLICATION STRESS
REACTOME METABOLSIM OF NON CODING RNA
REACTOME INTERACTION OF VPR WITH HOST CELLULAR PROTEINS
REACTOME NEP NS2 INTERACTS WITH THE CELLULAR EXPORT MACHINERY
REACTOME TRANSPORT OF RIBONUCLEOPROTEINS INTO THE HOST NUCLEUS
KEGG SPLICESOME
KEGG CELL CYCLE
KEGG DNA REPLICATION
REACTOME TRNA AMINOACYLATION
REACTOME AMINOACYL TRNA BIOSYNTHESIS
REACTOME CYTOSTOLIC TRNA AMINOACYLATION
KEGG MISMATCH REPAIR
KEGG ONE CARBON POOL BY FOLATE

REACTOME MITOTIC M M G1 PHASES
REACTOME MITOTIC PROMETAPHASES
REACTOME CELL CYCLE
REACTOME CELL CYCLE MITOTIC
REACTOME G2 M CHECKPOINTS
REACTOME MRNA PROCESSING REACTOME ACTIVATION OF ATR IN RESPONSE TO REPLICATION STRESS
KEGG CELL CYCLE
KEGG DNA REPLICATION
REACTOME AMINOACYL TRNA BIOSYNTHESIS
REACTOME TRNA AMINOACYLATION
REACTOME CYTOSTOLIC TRNA AMINOACYLATION
KEGG TERPENOID BACKBONE SYNTHESIS

REACTOME MITOTIC M M G1 PHASES
REACTOME MITOTIC PROMETAPHASES
REACTOME CELL CYCLE
REACTOME CELL CYCLE MITOTIC
REACTOME G2 M CHECKPOINTS
REACTOME MRNA PROCESSING REACTOME ACTIVATION OF ATR IN RESPONSE TO REPLICATION STRESS
KEGG CELL CYCLE
KEGG DNA REPLICATION
REACTOME AMINOACYL TRNA BIOSYNTHESIS
REACTOME TRNA AMINOACYLATION
REACTOME CYTOSTOLIC TRNA AMINOACYLATION

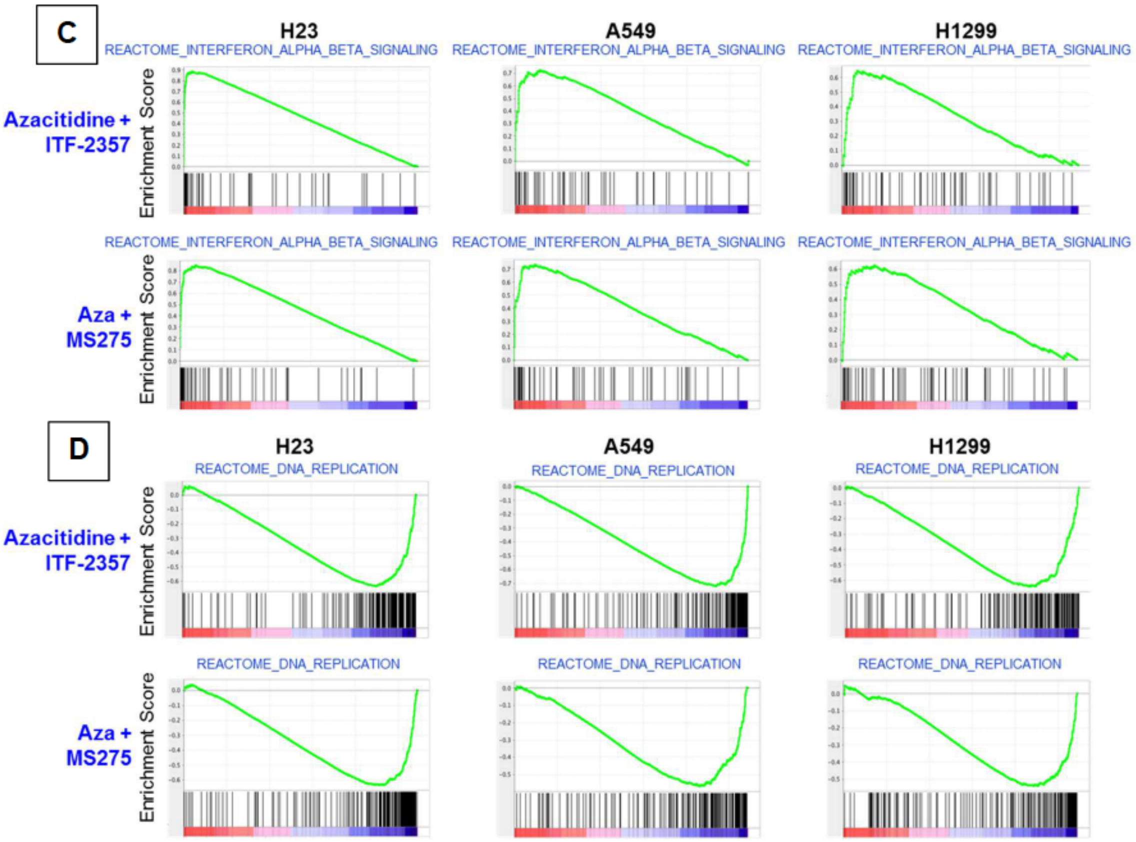
C
H23
A549
H1299
REACTOME_INTERFERON_ALPHA_BETA_SIGNALING
REACTOME_INTERFERON_ALPHA_BETA_SIGNALING
REACTOME_INTERFERON_ALPHA_BETA_SIGNALING
Azacitidine + ITF-2357
Enrichment Score
REACTOME_INTERFERON_ALPHA_BETA_SIGNALING
REACTOME_INTERFERON_ALPHA_BETA_SIGNALING
REACTOME_INTERFERON_ALPHA_BETA_SIGNALING
Aza + MS275
Enrichment Score
D
H23
A549
H1299
REACTOME_DNA_REPLICATION
REACTOME_DNA_REPLICATION
REACTOME_DNA_REPLICATION
Azacitidine + ITF-2357
Enrichment Score
REACTOME_DNA_REPLICATION
REACTOME_DNA_REPLICATION
REACTOME_DNA_REPLICATION
Aza + MS275
Enrichment Score

Figure 15: Aza + HDACi significantly imparts alteration of immune and cell cycle related genes sets

(A) Venn diagrams quantitating GSEA derived overlapping and unique pathways induced by combination treatment in at least 3 cell lines with the respective HDACi. (NES > 2.0, FDR < 0.25) and venn diagram of pathways commonly upregulated by combination treatment with Aza and the respective HDACi. **(B)** Venn diagrams quantitating GSEA derived overlapping and unique pathways downregulated by combination treatment in at least 3 cell lines with the respective HDACi. (NES < 2.0, FDR < 0.25) and venn diagram of pathways commonly down regulated by combination treatment with Aza and the respective HDACi. **(C)** GSEA enrichment plots for top upregulated pathway (Interferon αβ) following combination epigenetic treatment with the indicated HDACi. **(D)** GSEA enrichment plots for top downregulated pathway (DNA replication) following combination epigenetic treatment with the indicated HDACi. Above data are derived from microarray analysis of RNA from cells treated with 500nM Aza, 100nM ITF-2357, 100nM MS-275.

2.3 The potential of combinatorial epigenetic treatment to stimulate specific immune related genes

A primary goal for combined epigenetic therapy is to increase the efficacy of immune checkpoint and other immunotherapies. We found the combination of Aza + ITF-2357 to be the most effective relative to other conditions tested in terms of induction of IFNα/β pathway related genes, including those associated with antigen presentation (**Figures 16A, 16B and 16C**).

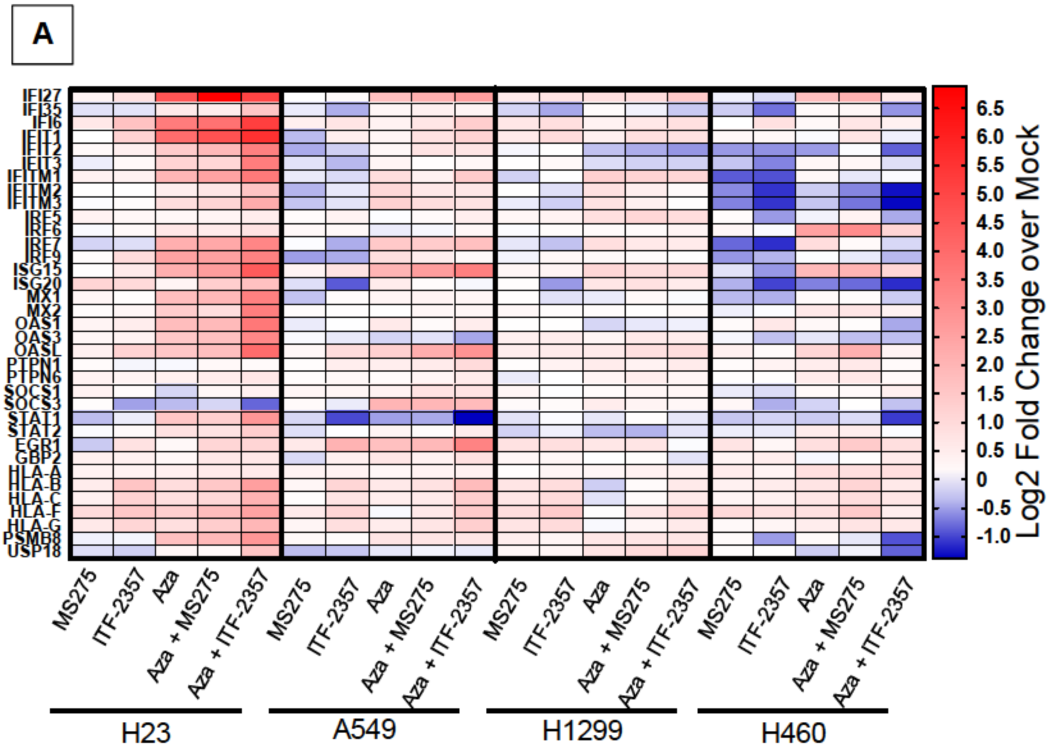
A
IFI27
IFI35
IFI6
IFIT1
IFIT2
IFIT3
IFITM1
IFITM2
IFITM3
IRF5
IRF6
IRF7
IRF9
ISG15
ISG20
MX1
MX2
OAS1
OAS3
OASL
PTPN1
PTPN6
SOCS1
SOCS3
STAT1
STAT2
EGR1
GBP2
HLA-A
HLA-B
HLA-C
HLA-F
HLA-G
PSMB8
USP18
MS275
ITF-2357
Aza
Aza + MS275
Aza + ITF-2357
H23
A549
H1299
H460
6.5
6.0
5.5
5.0
4.5
4.0
3.5
3.0
2.5
2.0
1.5
1.0
0.5
0
-0.5
-1.0
Log2 Fold Change over Mock

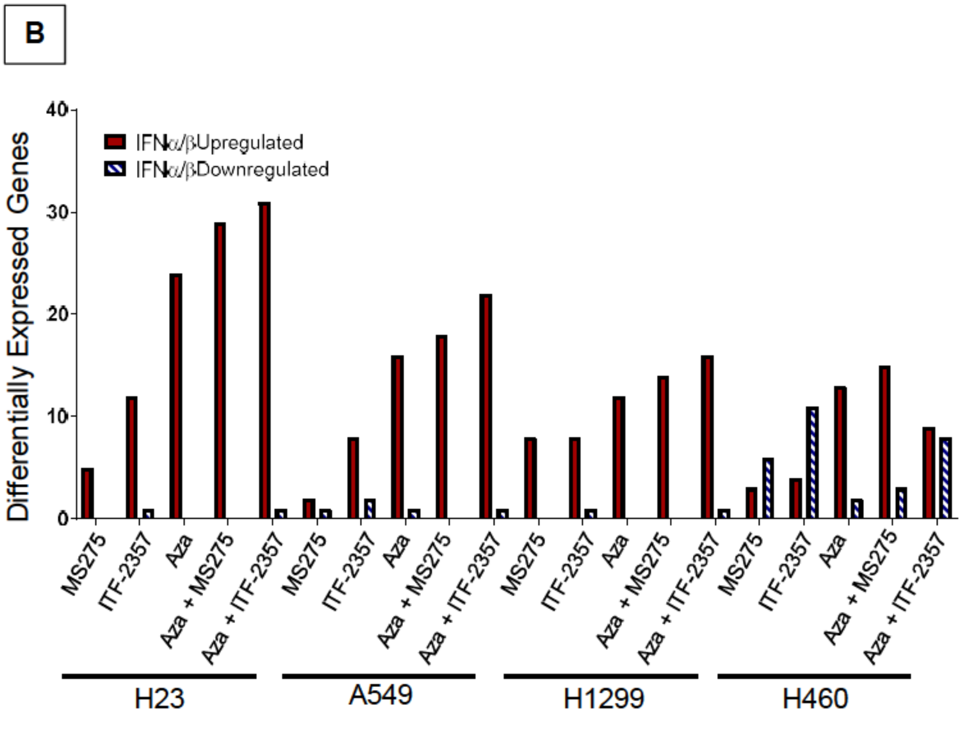
B
IFNα/β Upregulated
IFNα/β Downregulated
Differentially Expressed Genes
40
30
20
10
0
MS275
ITF-2357
Aza
Aza + MS275
Aza + ITF-2357
H23
A549
H1299
H460

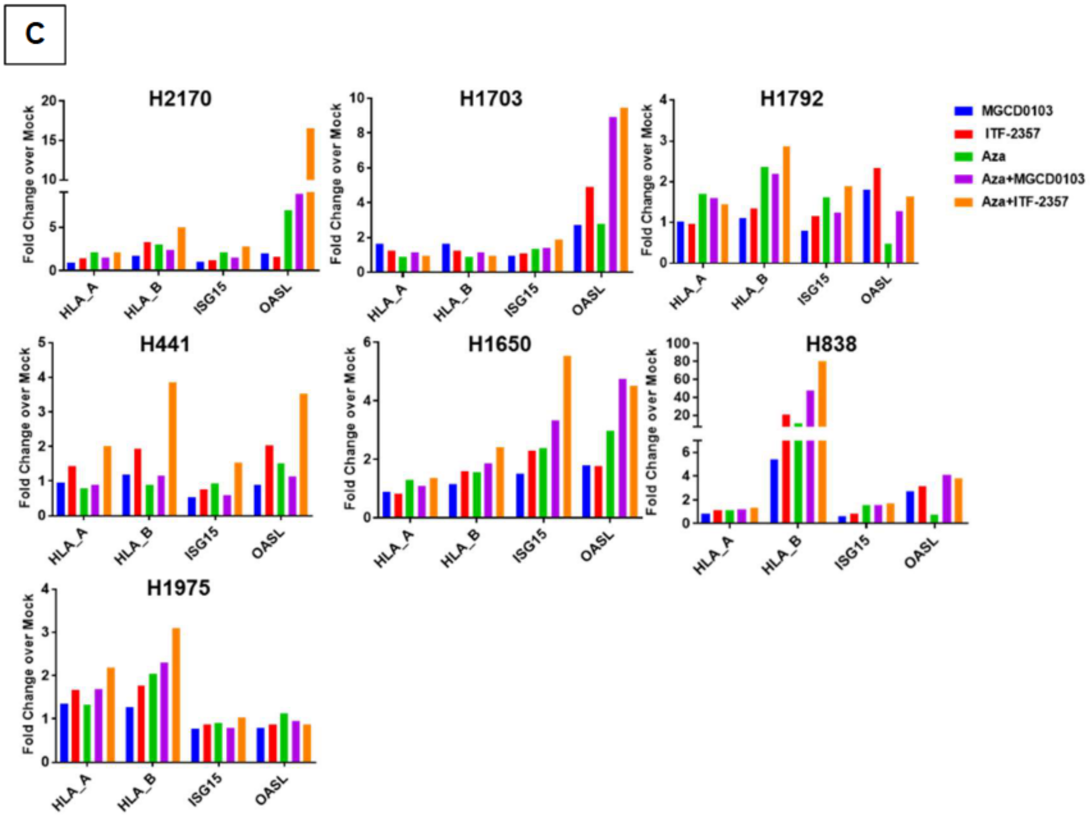

Figure 16: IFNα/β related genes are a conserved target of Aza + HDACi

(A) Heatmap of relative RNA expression for IFNα/β signaling pathway core enriched genes for indicated cell lines (microarray, day 8, 500nM Aza, 100nM MS275, 100nM ITF-2357). **(B)** Quantification of IFNα/β pathway core enriched genes differentially expressed by the indicated conditions (microarray, day 8, 500nM Aza, 100nM MS275, 100nM ITF-2357; differential gene expression cutoff Log2 fold change over mock > 0.5). **(C)** Expression of Interferon stimulated genes induced by Aza and/or the indicated HDACi in various NSCLC cell lines (qRT-PCR, day 8, 500nM Aza, 100nM ITF-2357, and 200nM MGCD0103).

To demonstrate whether this efficacy of immune gene induction by Aza + ITF-2357 was potency or isoform targeting based, we used isoform specific HDACi at concentrations mimicking 100nM ITF-2357. We observe the inhibition of HDAC1, 2 (MGCD0103) and HDAC6 (Tubastatin A) in combination with Aza induces IFNα/β pathway related genes, including antigen presentation, while HDAC3 (RGFP996) specific inhibitors demonstrate no significant induction of these genes (**Figures 17A-D**).

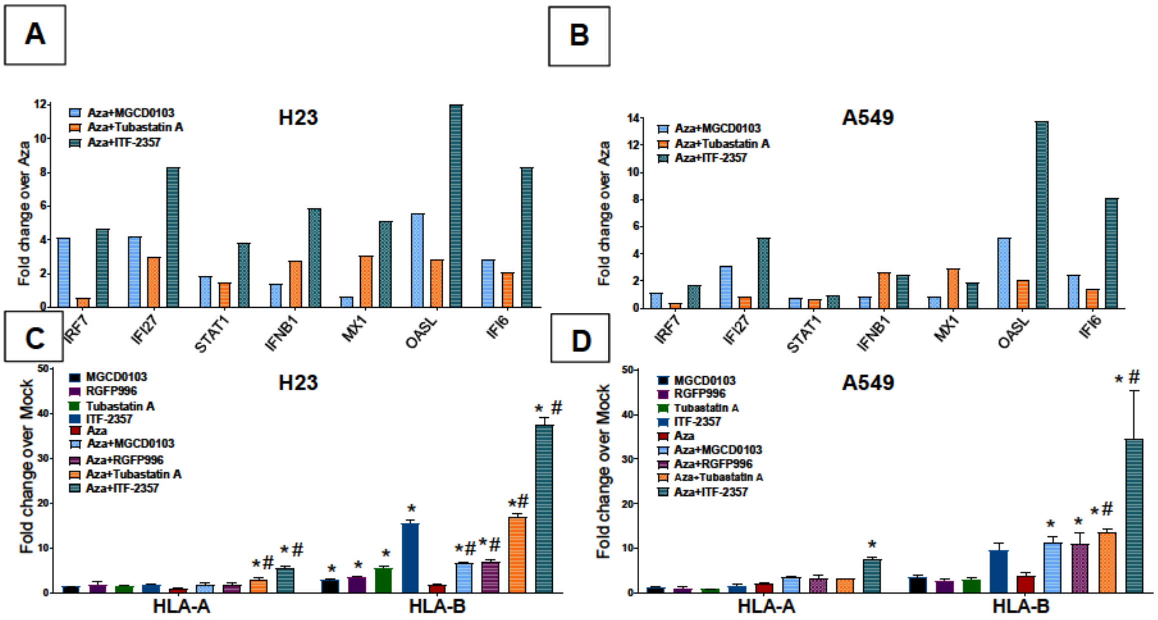

Figure 17: Inhibition of HDAC 1,2,6 isoforms increases Aza induced augmentation of IFNα/β related genes

(A and B) Expression of viral defense gene subset of IFNα/β pathway (PCR genecard, day 8, 500nM Aza, 100nM ITF-2357, 200nM MGCD0103, 1000nM Tubastatin A) in H23 **(A)** and A549 **(B)** cells. **(C and D)** Quantitation of selected MHC class I genes of IFNα/β pathway in response to Aza and/or HDACi in H23 **(C)** and A549 **(D)** cells (qRT-PCR, day 8, 500nM Aza, 100nM ITF-2357, 200nM MGCD0103, 2000nM RGFP996, 1000nM

We also compared the efficacy of ITF-2357 against another hydroxamic acid derivative HDACi (SAHA). Using doses at equal ratio of cmax for the respective inhibitors, we observe a superior augmentation of interferon genes by ITF-2357 when deployed in combination with Aza (**Figures 18A and 18B**). The above studies demonstrate an induction of interferon-stimulated genes by Aza, which are further augmented by HDACi's targeting isoforms 1, 2 and 6.

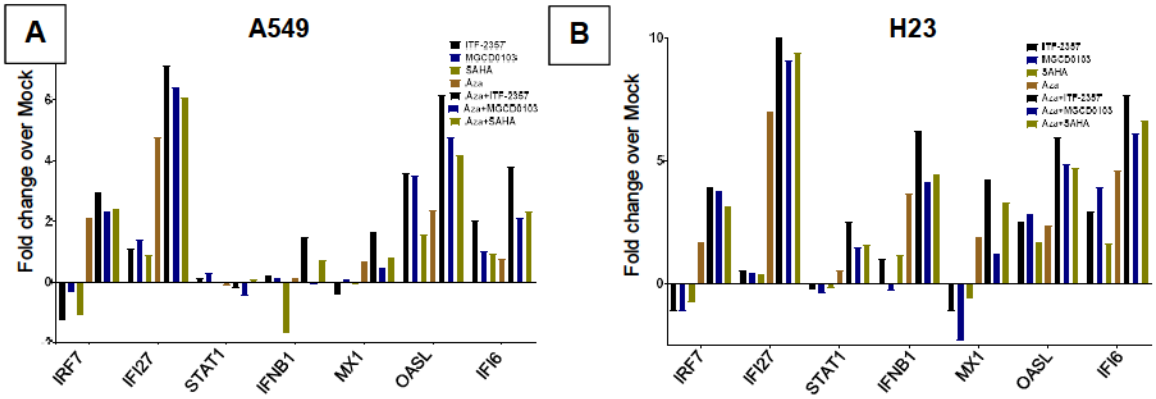

Figure 18: ITF-2357 is more potent than SAHA at facilitating ISG induction in combination with Aza

(A and B) Expression of Interferon stimulated genes induced by Aza and/or the indicated HDACi in (**A**) A549 and (**B**) H23 cells (PCR genecard, day 8, 500nM Aza, 100nM ITF-2357, 200nM MGCD0103, 300nM SAHA).

Cancer/testis antigens are epigenetic treatment-responsive and have an established role in facilitating the recognition of tumors through immune surveillance (Moreno-Bost et al., 2011; Oi et al., 2009; Weiser et al., 2001). We find in agreement with previous studies, the expression of cancer/testis antigens are Aza inducible, but a significant additional benefit is noted with the combination of Aza + ITF-2357 (**Figures 19A-D**).

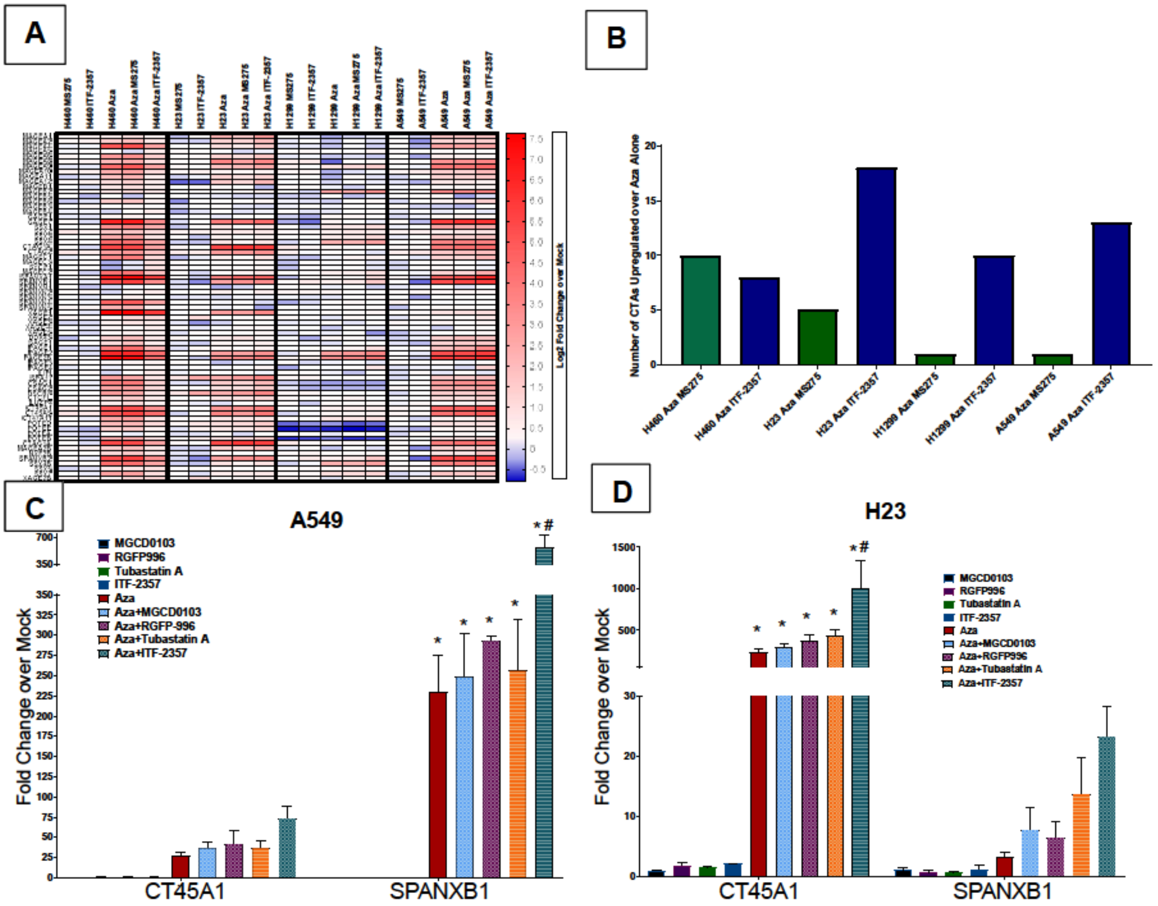

Figure 19: Cancer/Testis antigens are Aza inducible with further augmentation noted through the application Aza + ITF-2357

(A) Heatmap of relative RNA expression for cancer/testis antigen genes across NSCLC cell lines (microarray, day 8, 500nM Aza, 100nM MS275, 100nM ITF-2357). **(B)** Quantification of cancer/testis antigen transcriptional induction by combination Aza + HDACi treatment over Aza alone across NSCLC cell lines (microarray, day 8, 500nM Aza, 100nM MS275, 100nM ITF-2357; differential gene expression cutoff Log2 fold change over Aza >0.5). **(C and D)** Relative RNA expression of selected cancer/testis antigen transcripts in response to Aza and/or HDACi (qRT-PCR, day 8, 500nM Aza, 100nM ITF-2357, 200nM MGCD0103, 2000nM RGFP996, 1000nM Tubastatin A, n=3, data are mean ± SEM).

The augmentation of the IFNα/β pathway by Aza partially relies on increasing dsRNA species, including ERV transcripts (Chiappinelli et al., 2015; Roulois et al., 2015; Stengel et al., 2010; Strissel et al., 2012). Indeed, combination HDACi with Aza transcriptionally induced multiple ERV's across all cell lines tested (**Figures 20A and 20B**). We found ERV9-1 to be the most differentially expressed ERV induced by Aza + ITF-2357. Using isoform specific inhibitors in combination with Aza we determined its transcription is potentiated most robustly by inhibition of HDAC6(a cytoplasmic HDAC) (**Figures 20C and 20D**). The inducibility of interferon signaling from ERV transcription are linked in our NSCLC cells as single ERV overexpression induces transcription of OASL1, an interferon responsive gene (**Figure 20E**).

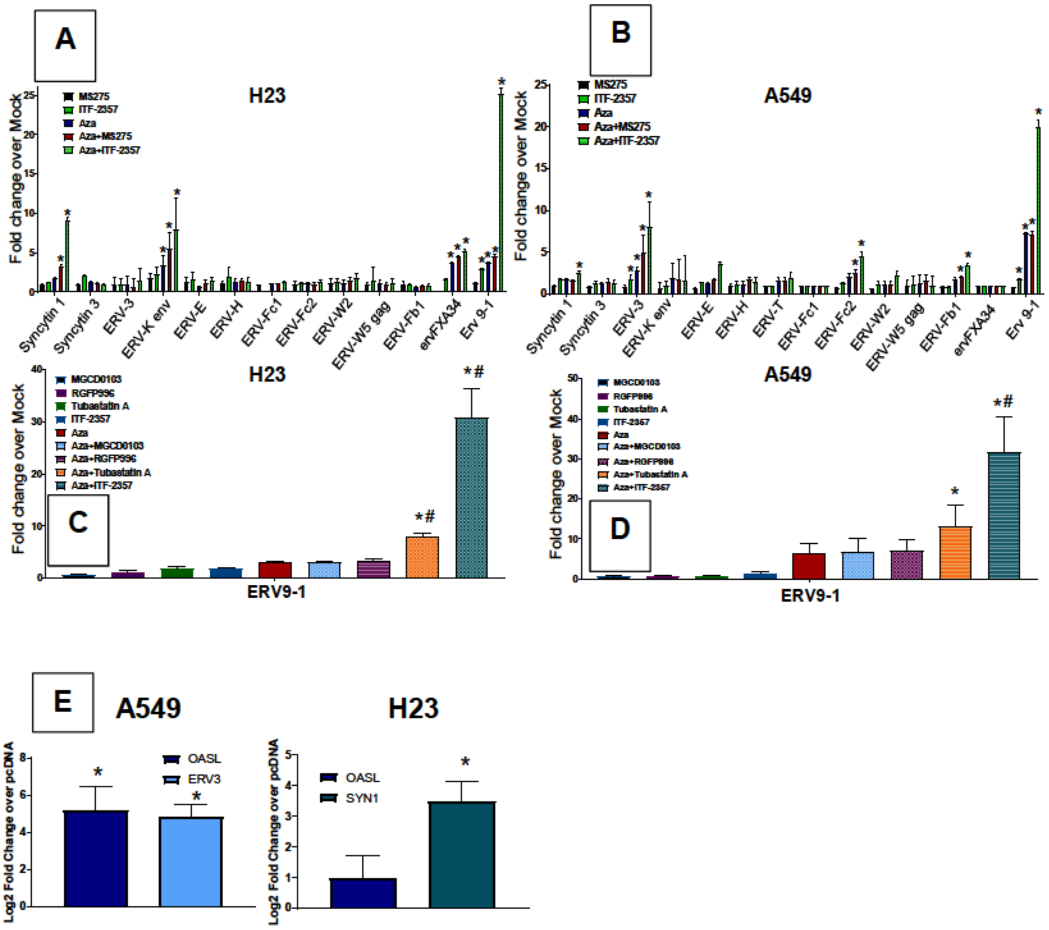

Figure 20: Combination epigenetic enhances the induction of ERVs over Aza alone

(**A and B)** Quantitation of ERV transcripts in response to Aza and/or HDACi in H23 **(A)** and A549 **(B)** cells (qRT-PCR, day 8, 500nM Aza, 100nM ITF-2357, 100nM MS-275; n=4). **(C and D)** Quantitation of ERV9-1 in response to Aza and/or HDACi in H23 **(C)** and A549 **(D)**. (500nM Aza, 100nM ITF-2357, 200nM MGCD0103, 2000nM RGFP996, 1000nM Tubastatin A, n=3). **(E)** Effect of ERV overexpression on transcription of the interferon stimulated gene, OASL, in A549 and H23 cells (48-hour post transfection, qRT-PCR, ERV3 overexpressed in A549, SYN1 overexpressed in H23, n=4, data are mean ± SEM). * p value< 0.05 calculated by two tail t test.

4. Discussion

In summary, Aza acts to sensitize NSCLC to the cytostatic actions of HDACi mainly through the inhibition of HDACs 1, 2, and 3. Combination epigenetic therapy deployed in vivo using our defined schema demonstrates efficacy in 3 independent immune incompetent mouse models, including a PDX model. HDACi's enhance Aza induced interferon responsive gene transcription mediated most robustly through the inhibition of HDAC's 1, 2, and 6. Class I antigen presentation is augmented through the inhibition of HDAC's 1, 2, 3, and 6 in combination with Aza. While the induction of cancer/testis antigen transcription requires potent HDACi's, such as ITF-2357, to mediate significant upregulation over Aza alone.

III. MYC perturbation as a driver of response to epigenetic treatment

1. Introduction

Combination epigenetic therapy holds promise based on the predicted mechanism of gene re-expression as defined in depth previously. But true predictors of response and actionable targets of combination epigenetic therapy in NSCLC have not been defined. In this section, we aim to elucidate correlative biomarkers which are predictive of response to combination epigenetic treatment and to prove causation of this or these targets in eliciting the phenotypes observed.

2. Materials and methods

MYC targets heatmap:

MYC targets heat maps are based on hierarchical clustering of Log2 fold change over mock using Euclidean distance and complete linkage of MYC hallmarks gene set v2.

MYC Immunoblotting:

Protein was extracted by 4% SDS mediated lysis, followed by processing of lysates through homogenizer column (Omega). Protein concentrations were estimated by BCA (Pierce Biotechnology). Lysates were processed using PAGE with 4-12% Bis-Tris BOLT gel (Life Technologies) and transferred to PVDF membrane (Millipore). Membranes were blocked in 10% milk/TBST and immunoblotted with the following antibodies.: rabbit monoclonal c-MYC (Cell Signaling, 1:1000, Mouse monoclonal anti-β-Actin (Sigma Aldrich, 1:10000). The loading control antibodies anti-β-Actin in all cases were applied after membrane stripping.

MYC Knockdown Cell Viability Assay:

MYC knockdown was initated using Broad TRCN0000010391 clone and control vector shGFP 5′- GCAAGCTGACCCTGAAGTTCAT3-3′. Clonal selection was initated with puromycin selection. Selected clones were plated at the cell densities and treated as described in Cell viabilty assay section of methods. MTS was used to quantify numbers of proliferating cells. Bar graphs depicted are representative of the percent of MYC knockdown cells present as a percentage of the empty vector treated controls for same dose of drug. Error bars are representative of mean +/- SEM between experimental replicates. Statistical significance was determined by two tailed t test between empty vector and MYC shRNA treated cells at each dose.

MYC Overexpression Cell Viability Assay:

MYC vector (Addgene plasmid # 46970) (Cheng et al., 2013) and empty vector (Clontech cat# 632154). Clonal selection was initated with puromycin, 2 days post infection. Selected clones were plated at cell densities and treated as described in Cell viabilty assay section of methods. MTS was used to quantify numbers of proliferating cells. Bar graphs depicted are representative of the percent of MYC overexpression cells present as a percentage of the empty vector treated controls for same dose of drug. Error bars are representative of mean +/- SEM between experimental replicates. Statistical significance was determined by two tailed t test between empty vector and MYC overexpression vector treated cells at each dose.

MYC overespression IFNα/β qPCR:

qPCR methodology for detecting IFNα/β related genes (ISG15, OASL1, HLA-A, HLA-B) differential expression was conducted on 20ng of cell line cDNA with SYBR green technology. Expression values were calculated as fold change over empty vector by delta-delta ct. Beta-actin was used as housekeeping gene for normalization of NSCLC cell line expression.

MYC overexpression Taqman microfluidic genecard:

1ug of total RNA was used for cDNA reaction and diluted to 50uL total volume in molecular grade water. Diluted cDNA was combined with 50uL of Taqman universal PCR mastermix and loaded onto a Taqman microfludic genecard with the following primer/probe sets preloaded: IRF7, IFI27, STAT1, IFNB1, MX1, OASL, IFI6, beta actin, TBP. Expression values were calculated as fold change over empty vector by delta-delta ct. Beta actin and TBP were used as housekeeping genes for normalization of NSCLC cell line expression.

3. Results

As described earlier DAVID analysis of the top 500 differentially expressed genes reveals three of the top eight pathways are MYC related (**Figure 13C**), suggesting the perturbation of MYC as a key target of our epigenetic therapy. Critically, in the tested NSCLC cell lines Aza produces a significant transcriptional downregulation of MYC, with an at least 1.4-fold reduction observed across all cell lines assayed (**Figure 20A)**. These transcription data correlate with downregulation of MYC protein in A549 and H460 cells (**Figure 20B**). Additional assessment of MYC protein downregulation by Aza and priming to sequential HDACi across a panel of NSCLC cell lines of varying oncogenotypes revealed a significant correlation between degree of downregulation and HDACi sensitization by Aza (**Figures 20B and 20C).**

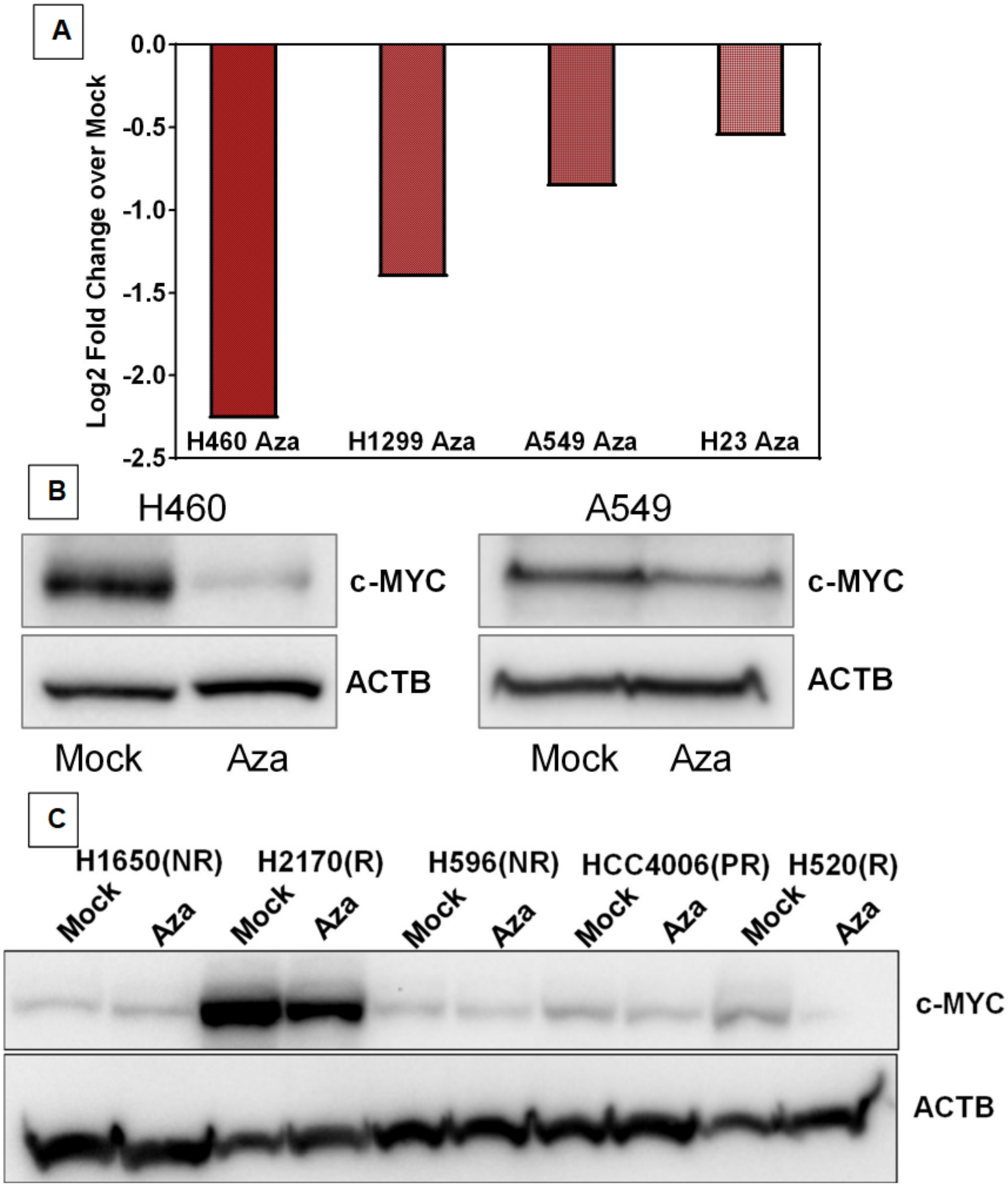
A
Log2 Fold Change over Mock
0.0
-0.5
-1.0
-1.5
-2.0
-2.5
H460 Aza
H1299 Aza
A549 Aza
H23 Aza
B
H460
A549
c-MYC
ACTB
c-MYC
ACTB
Mock
Aza
Mock
Aza
C
H1650(NR)
H2170(R)
H596(NR)
HCC4006(PR)
H520(R)
Mock
Aza
Mock
Aza
Mock
Aza
Mock
Aza
Mock
Aza
c-MYC
ACTB

Figure 21: c-MYC depletion by Aza is correlated with efficacy of HDACi across oncogenotypes of NSCLC

(A) Quantitation of relative MYC RNA expression in NSCLC cell lines following 500nM Aza treatment (microarray, day 8). (**B**) Immunoblot showing expression of MYC protein on day 9 of treatment. β Actin used as loading control (500nM Aza, n=3). (**C**) Immunoblot showing MYC expression in the indicated cell lines treated with Aza. β-Actin used as loading control. NR= non-responding cell line with no significant change in ITF-2357 IC50 by Aza pretreatment dose response data, PR= partial responder, less than a 25% reduction in ITF-2357 IC50 by 500nM Aza, R= responding cell line, greater than or equal to 50% ITF-2357 IC50 reduction by Aza pretreatment (Day 9, 500nM Aza)

Aza + HDACi acts to further deplete MYC over Aza treatment alone **(Figure 21A).** The application of Aza and Aza + HDACi treatment induces potent repression of the top 200 MYC targets (**Figure 21B**).

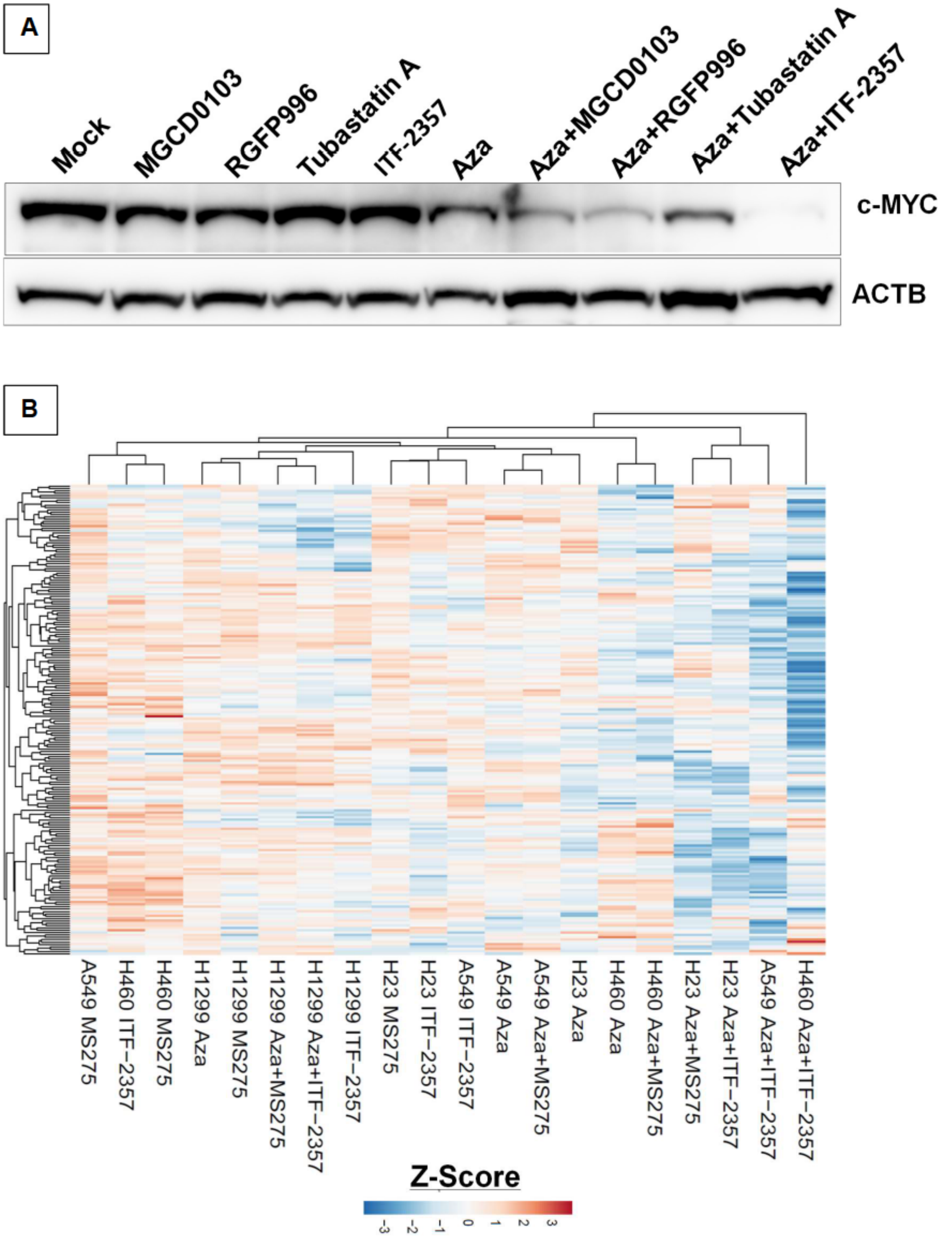

Figure 22: Combination epigenetic treatment further represses MYC signaling over Aza alone

(A) Immunoblot showing MYC expression in H460 cells treated with Aza with or without HDACi. β-Actin used as loading control (Day 9, 500nM Aza, 100nM ITF-2357, 200nM MGCD0103, 2000nM RGFP996, 1000nM Tubastatin A, n=2)

(B) Unsupervised hierarchical clustering of relative RNA expression for GSEA HALLMARK MYC TARGETS. Color gradation based on Z score ranking of log2 fold change over mock (microarray, day 8, 500nM Aza, 100nM MS-275, 100nM ITF-2357).

Importantly, knockdown of MYC protein phenocopies the Aza sensitization of NSCLC to HDACi induced cytostasis (**Figures 22A and 22C**). The stable overexpression of MYC partially rescues the Aza induced sensitization to HDACi induced cell depletion (**Figures 22B and 22D**). These data indicate an Aza induced MYC depletion as a potent sensitizer to HDACi induced proliferative arrest, and accordingly implicate depletion of MYC signaling as a driver of these events.

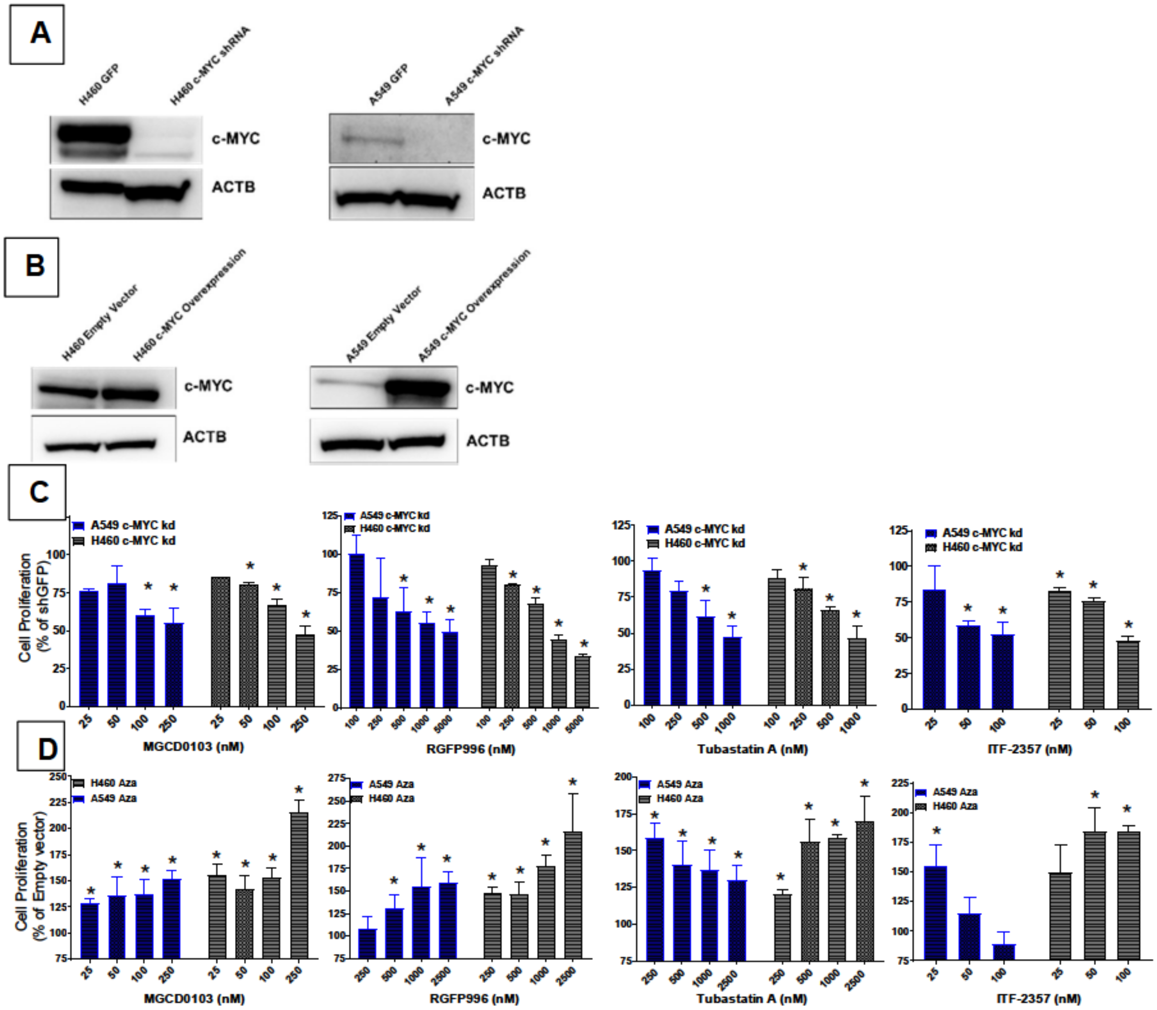

Figure 23: c-MYC perturbation impacts the anti-proliferative efficacy of NSCLC response to HDACi

(A) Immunoblot showing MYC expression in H460 and A549 cells infected with empty or MYC shRNA vector. β-Actin used as loading control. (day 4 of knockdown, n=2). **(B)** Immunoblotting for MYC in H460 and A549 cells infected with empty vector or MYC over expression vector. β-Actin used as loading control (day 5 of overexpression, n=2). **(C and D)** A549 and H460 cell line quantitation of colorimetric absorbance as indicator of proliferating cell number, normalized to untreated control **(C)** Percent proliferation for GFP and shMYC vector infected cells treated with the indicated HDACi for 5 days (n=3). **(D)** Percent proliferation for empty vector (EV) or MYC overexpression vector containing cells treated with indicated HDACi for 5 days (n=3 overexpression clones).

High MYC tumors have been reported to display resistance to IFNγ signaling and the action of cytotoxic T lymphocytes (Casey et al., 2016; Schlee et al., 2007a; Schlee et al., 2007b). In this regard, exogenous MYC overexpression results in antagonism of interferon stimulated gene induction and antigen presentation induced by epigenetic treatment (**Figures 23A and 23B).** Thus, the MYC depletion signature imparted by Aza sensitizes to the actions of HDACi induced cytostasis and augments NSCLC interferon signaling.

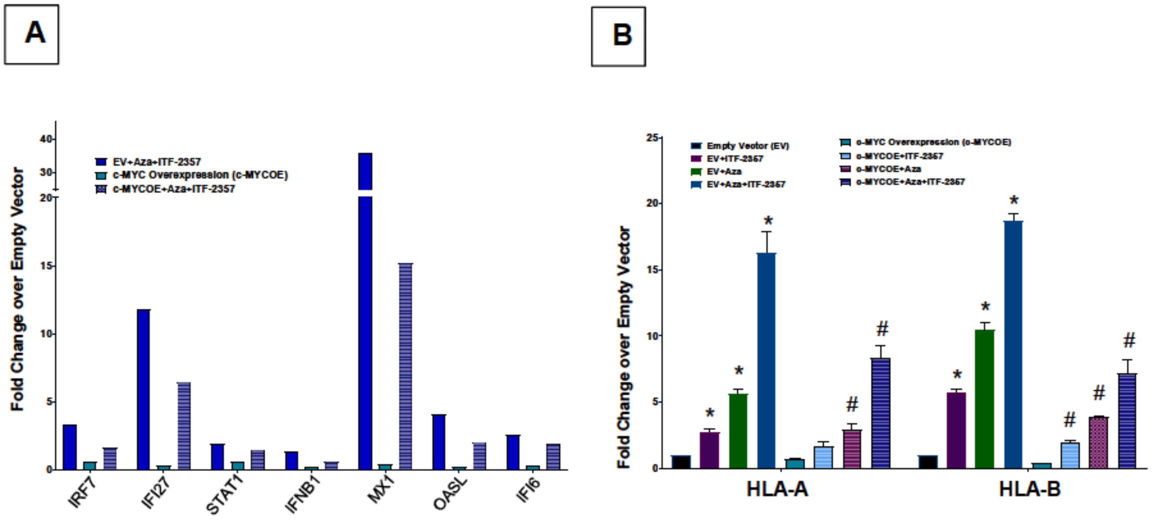

Figure 24: c-MYC overexpression antagonizes the induction of IFNαβ genes by epigenetic treatment

(A and B) Relative RNA expression of IFNα/β pathway responsive genes in A549 cells infected with EV or MYC overexpression construct and treated with mock or 500nM Aza + 100nM ITF-2357 **(A)** IFNα/β pathway - viral defense gene subset (genecard, day 8). **(B)** IFNα/β pathway- MHC class I genes (qRT-PCR, day 8, n=3).

Data are presented as mean ± SEM. * $p < 0.05$ relative to mock, # $p < 0.05$ relative to EV + Epigenetic treatment. P value determined by two-tail t test.

4. Discussion

These data implicate MYC signaling and its downregulation as a key arbiter of the combination epigenetic treatment efficacy. Specifically, the downregulation of MYC by Aza is significantly correlated with the efficacy of combination epigenetic therapy in terms of both cytostasis and IFN gene augmentation. Additionally, perturbation of MYC levels through knockdown and overexpression studies alters the response to epigenetic therapy. This result is suggestive of direct MYC causation in the observed phenotypes.

IV. Combination epigenetic treatment exerts a robust anti-tumor effect in 2 independent mouse models

1. Introduction

The application of our combination epigenetic regimen to immune competent mouse models allowed us to simultaneously validate both our immune dependent and immune autonomous phenotypes derived from our in vitro schemas. To accomplish these ends we deployed our regimen in both an interception early intervention genetic mouse model LSL-Kras^{G12D} and an aggressive adenocarcinoma mouse model Lewis Lung Carcinomas. Both phenotypic and transcriptomic parameters were assayed to evaluate therapeutic efficacy of combination epigenetic treatment.

2. Materials and methods

LSL-Kras^{G12D} mouse model:

LSL-Kras^{G12D} mice (Jackson et al., 2001) were obtained from Jackson laboratories and bred with wild type C57BL/6 mice to generate heterozygous LSL-Kras^{G12D} mice. LSL-Kras^{G12D} mice (8-10 weeks, both genders) were infected intratracheally with Adenoviral vectors encoding Cre (obtained from University of Iowa) to activate Kras. LSL-Kras^{G12D} mice harbor a latent point-mutant allele of Kras (KrasG12D) and infection with an adenoviral vector encoding Cre leads to Cre-mediated deletion of a transcriptional termination sequence (Lox-Stop-Lox, LSL) and the oncogenic Kras production, thereby resulting in very high frequency of lung tumors (Jackson et al., 2001). All experimental animal protocols were performed in accordance with guidelines approved by the animal care and use committee at the Johns Hopkins University (Baltimore, MD). Mice were examined for presence of disease at 16 weeks post infection with AdenoCre. Mice were sacrificed and lungs were examined histologically. At this stage most of the mice showed presence of significant regions of hyperplasia as well as adenomas. Drug treatments were started as per the schedule shown in Figure S7A. Mice were divided in two groups. Once group was injected with vehicle control while the other was injected with combination epigenetic drugs. Mice were uniformly distributed into the two treatment groups so that each group had comparable numbers of age and weight matched male and female mice.

Lewis lung Carcinoma (LLC) model :

LLC cells (LLC1, ATCC) 2.0 x 10^4 were injected subcutaneously in flanks of male C57BL6 mice (6-8 weeks old) obtained from Harlan. LLC1 cells were suspended in 100uL RPMI + Matrigell (1:1). Drug treatments were started 7 days post injection when palpable tumors could be discerned. Mice were injected with drugs as per the dosing schema in Figure S7A. Treatment was continued for a month followed and at the culmination of study mice were sacrificed, tumors were harvested and weighed. Lungs of these mice were infllated and fixed in formaldehyde for 24 hours prior to sectioning and staining with H&E stains.

In-vivo Drug Studies:

Mice were treated as follows: Azacitdine 0.5 mg/kg (PBS vehicle) IP injected daily for the first 5 days of every 14 day treatment cycle. In vivo HDACi was applied on day 7 of 14 day treatment cycle and injected daily for 5 days of 14 day cycle. ITF-2357 2.0 mg/kg (1% DMSO in PBS vehicle) IP injected daily for 5 days sequentially, every 14 days. MS-275 2.0 mg/kg (1% DMSO in PBS vehicle) IP injected daily for 5 days sequentially, every 14 days. MGCD0103 4.0 mg/kg (5% DMSO in PBS vehicle) IP injected daily for 5 days sequentially, every 14 days. InVivoMAb mouse Anti-PD1 (BioXcell RMPI 14 clone) injected 10ug/kg on the 12th day of a 14 day cycle. InVivoMAb Rat IgG2a Isotype control (BioXcell 2A3 clone) injected 10ug/kg on the 12th day of a 14 day cycle. CD8a depletion antibody (BioXcell, 2.43 clone), 3 times per week at 150ug per animal, see LLC CD8 depletion model for details about the treatment schema. For xenograft studies, treatment was iniated 10 days post injection when palpable tumors could be discerned and continued for 37 days. For Kras G12D mouse model studies, drug application initated 16 weeks post Ad-Cre instillation, and applied for 12 weeks as described in the Kras G12D animal model section. For LLC model treatment was initated 7 days after subcutaneous implant of flank tumor and mice were treated as described in (**Figure S7A**). Mice were injected IP with 150ug of CD8a antibody (BioXcell), three times per week throughout the duration of study. CD8 depletion was verfied by assesment of CD8% of CD45 population in the spleen of depleted sample vs. control samples.

Histological analysis of mouse tissues:

Lungs tissues were fixed in 10% formalin overnight, and subsequently transferred into 70% ethanol, embedded in paraffin and sectioned (5 μM) at 3 levels at regular intervals.

Sections were stained with Hematoxylin and eosin (H&E) and scanned using the Aperio whole slide scanning system (Scanscope CS) The entire left lung lobe was scanned for presence of adenomas/adenocarcinomas using the Aperio ImageScope analysis software. For each sample, sections from 2 levels were analyzed. Unstained sections of the left lung were also used for Immunohistochemistry (IHC) staining. All Images were scanned at 20x magnification using the Aperio Scanscope system.

Immunohistochemistry (IHC):

Immunostaining of lung sections was performed with the PowerVision kit according to the manufacturer's protocol (Leica Biosystems). Briefly, slides were heated at 60°C for 10 min,deparaffinized and hydrated through xylene, graded ethyl alcohols, dH2O, dH2O with 20% Tween 20 (P-7949, Sigma-Aldrich). After antigen retrieval (45 minutes of steaming in Target Retrieval Solution (Dako S170084-2) using Black and Decker Handy Steamer Plus), sections were treated 5 minutes with Dual Endogenous Enzyme Block (S2003, Dako). Sections with primary antibodies Ki67 (Cell signalling, 9101, 1:500) were incubated at room temperature for 45 minutes. Secondary used was anti-rabbit IgG-reagent provided in the Powervision kit (PV6119, Leica Biosystems) for 30 minutes. Immunostaining was visualized with DAB chromogen (D4293, Sigma-Aldrich) and sections were counterstained with Mayer's hematoxylin. Control slide: No primary control.

Gene expression analysis by microarray:

RNA expression were conducted by microarray for the conditions descibed in the relevant figures. The R/Bioconductor package limma was used to process expression data. Within- and between-array normalizations were performed using the loess and aquantile methods, respectively. The normexp option was used for background correction. Raw files read in using the read.maimages function. Log2 fold change in transcription for drug treated conditions over mock treated was obtained for each sample at each time point studied. Ranked lists of log2 fold change were analyzed using Gene Set Enrichment Analysis (GSEA) by the Broad Institute and data packages (Subramanian et al., 2005). Pathways enriched with a false discovery rate less than 0.25 were selected with cutoff 1.5 normalized enrichment score cutoff in mouse studies. Median absolute deviation analysis of Log2 fold change transcription data were obtained using Morpheus program (Broad).

3. Results

The translational potential for utilizing our chronic schema of alternating, low dose 1-week Aza followed by 1-week ITF-2357 is apparent from robust efficacy when tested in two mouse models of NSCLC. The first, the LSL-Kras^{G12D} mouse model of NSCLC, represents an interception model as we began treatment when lung adenomas emerge 16 weeks following the lung specific activation of the mutation (Jackson et al., 2001). Mice were treated with the combination drug treatment for 3 months using the schema as shown in **Figure 24A**. The therapy is well tolerated and while mock treated mice developed large adenocarcinoma lesions in the lungs, combination epigenetic treatment prevents the occurrence of these macroscopic lesions and caused over a 60% reduction of tumor area in the treated mice **(Figures 24B and 24C).** Consistent with all the studies in the human NSCLC cells, proliferation as assessed by ki67 positivity is markedly reduced in any remaining histologic, adenomatous lesions (**Figure 24D**).

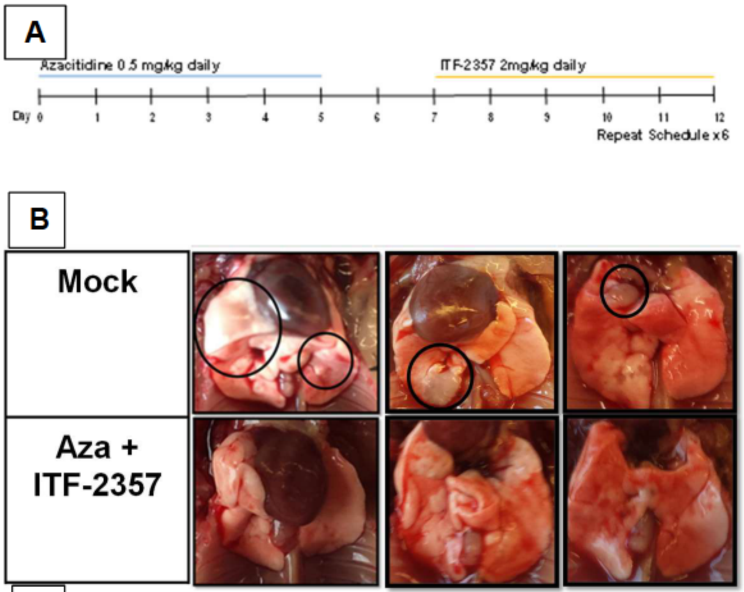
A
Azacitidine 0.5 mg/kg daily
ITF-2357 2mg/kg daily
Day 0 1 2 3 4 5 6 7 8 9 10 11 12
Repeat Schedule x6
B
Mock
Aza +
ITF-2357

C

D

Figure 25: Combination epigenetic therapy reduces burden, progression and proliferation of LSL-Kras^{G12D} model

(A) In vivo treatment schema for Aza + ITF2357 applied to a LSL-Kras^{G12D} murine model of NSCLC **(B)** Macroscopic images of LSL-Kras^{G12D} lungs treated with vehicle or Aza and ITF-2357, for 3 months (n=7 mock and n=8 Aza + ITF-2357). **(C)** Representative H & E stained images of murine lung sections treated with mock or Aza + ITF-2357 (n=6 mock, n=7 Aza + ITF-2357 per group). Scale bar = 100 μ. Quantitation of total tumor area occupied by lesions in lungs of LSL-Kras^{G12D} mice treated with mock or Aza + ITF-2357. Data are presented as mean ± SEM, p value determined by two tail t test (n=6 mock, n=7 Aza + ITF-2357 mice per group/2sections analyzed per mouse). **(D)** Representative Ki67 stained IHC images of murine lung sections treated with mock or Aza + ITF-2357 (n=5 per group) Scale bar = 100 μ.

The translational potential for our combination epigenetic drug efficacy for established, aggressive NSCLC is apparent utilizing a second mouse model of NSCLC, Lewis Lung Carcinoma (LLC). This murine model has demonstrated high correlation between response in the animal and response in the clinic for 2 therapeutic regimens (Kellar et al., 2015). Treatment with our alternating schedule of Aza + ITF-2357, and of Aza + MGCD0103 for 1 month, not only reduces growth of established and rapidly growing primary tumor explants of the LLC cells, but dramatically reduces metastatic occurrence and burden (**Figure 25A and 25B**).

Figure 26: Combination epigenetic treatment of LLC model reduces both primary and metastatic burden

(A) Lewis lung carcinoma (LLC) tumor weights of subcutaneous explants from one-month mock and Aza + ITF-2357 treated mice (n=19 mice per group, error bars SEM). Representative H & E stained images of lung metastasis from LLC mice obtained from one-month mock and Aza + ITF-2357 treated mice (n=12 mice per group) with indicated percentage frequency of metastasis. **(B)** Lewis lung carcinoma (LLC) tumor weights for subcutaneous explants from one-month mock and Aza + MCCD0103 treated mice (n=19 mock, same mice represented in Figure 5D, and n=12 Aza + MGCD0103). Representative H & E stained images of lung metastasis from these mice. Percentage frequency of this is event shown on the right.

Transcriptomic analysis of combination epigenetic treatment in murine NSCLC model

Importantly, as outlined below, the above efficacy of our combination therapy is accompanied by profound immune effects. First, in the LSL-Kras^{G12D} mice, the combination epigenetic treatment profoundly altered the tumor transcriptome with 5167 significantly upregulated and 4540 downregulated genes (**Figure 26A**). This corresponds to 18 gene sets upregulated and 52 gene sets downregulated by GSEA analyses with the former predominantly associated with immune parameters and the latter with cell cycle pathways, respectively (**Figure 26B**). Similar to the results for human NSCLC lines, 12 of the 18 gene sets upregulated involved strong induction of cytokine and interferon related gene sets (**Figure 26C**) as well as for 24 genes involved with inflammatory responses (**Figure 26D**). Concomitantly, as for the human NSCLC lines, most of the down-regulated cell cycle pathways involved myc pathway signaling (**Figure 26E**) with decreases in 30 myc pathway related genes (**Figure 26F).**

A B

C D E F

Figure 27: Combination epigenetic treatment induces tumor immune signature with a correlated repression of proliferation and MYC related signaling

(A) Volcano plot of relative RNA expression from LSL-Kras^{G12D} mice tumors treated for 3 months with Aza + ITF-2357 as compared to mock mice. Genes in upper left and right quadrants are significantly, differentially expressed (microarray, n=2 per group). **(B)** GSEA (KEGG, REACTOME, HALLMARK gene ontologies) pathway distribution for Aza + ITF-2357 vs. mock tumors from LSL-Kras^{G12D} mice. Horizontal line denotes FDR significance cutoff of 0.25. Immune and cell cycle related gene sets are demarcated by green and red dots respectively (microarray, n=2 per group). **(C)** Gene sets upregulated in LSL-Kras^{G12D} mice (< FDR 0.25 and > NES 1.5) by Aza + ITF-2357. Color gradation based on GSEA NES. **(D)** Representative upregulated GSEA plots with corresponding core enriched genes; color gradation representative of Log2 fold change over mock. **(E)** Gene sets downregulated in LSL-Kras^{G12D} mice (< FDR 0.25 and < NES 1.5) by Aza + ITF-2357. Color gradation based on GSEA NES. **(F)** Representative Downregulated GSEA plot with core enriched genes; color gradation representative of Log2 fold change over mock treated RNA expression.

4. Discussion

These data demonstrate a potent reduction in tumor proliferation, growth, and burden is induced by combination epigenetic treatment in 2 independent mouse models of NSCLC. Additionally, we observe a transcriptional signature similar to the noted response in the human NSCLC cell lines. These data demonstrate that immune related signaling and MYC pathway downregulation is a conserved response to combination epigenetic therapy and suggest these pathways may be tied to therapeutic efficacy both in vitro and in vivo.

V. Combination epigenetic treatment alters the tumor immune microenvironment, most markedly on the lymphocyte compartment.

1. Introduction

The immune related signaling noted in the whole tumor transcriptomics provided the suggestion that the immune microenvironment could be altered by the application of combination epigenetic treatment in vivo. In an effort to understand the immune microenvironment, we sought to define the polarization of both infiltrating macrophages and lymphocytes into the tumor microenvironment. These data aided in delineating the respective roles of these populations in both the phenotype observed and the whole tumor transcriptional signature noted.

2. Materials and methods

Immunohistochemistry (IHC):

Immunostaining of lung sections was performed with the PowerVision kit according to the manufacturer's protocol (Leica Biosystems). Briefly, slides were heated at 60°C for 10 min,deparaffinized and hydrated through xylene, graded ethyl alcohols, dH2O, dH2O with 20% Tween 20 (P-7949, Sigma-Aldrich). After antigen retrieval (45 minutes of steaming in Target Retrieval Solution (Dako S170084-2) using Black and Decker Handy Steamer Plus), sections were treated 5 minutes with Dual Endogenous Enzyme Block (S2003, Dako). Additional blocking steps were used for CD8 and F4/80 slides using DakoCytomation Biotin Blocking System (X0590). Antibody incubations for CD8 (eBiosciences, 14-0808, 1:800) and F4/80 (Serotec, MCAP497, 1:1000) were carried out at room temperature for 45 minutes, soaked an additional 45 min in PBS-Tween, and followed by mouse adsorbed biotinylated anti Rat IgG (Vector, BA-4001, 1:500) for 15 minutes. For all, the secondary used was anti-rabbit IgG-reagent provided in the Powervision kit (PV6119, Leica Biosystems) for 30 minutes. Immunostaining was visualized with DAB chromogen (D4293, Sigma-Aldrich) and sections were counterstained with Mayer's hematoxylin. Control slides: No primary for each, CD8 (spleen), F480 (tumor)

F4/80 Intratumor Macrophage Analysis:

F4/80 IHC stained sections were scanned used the Aperio system as described earlier, these images were analyzed use imagescope software. To generate the false color images depicted, used to demarcate pixel saturation by macrophage infiltration, the images were analyzed by the positive pixel v4 algorythm.

Isoation of murine bone marrow derive macrophages (BMDMs):

Mice (6-8) week old were euthanized and hind legs were harvested under aseptic conditions. Femors and tibia were obtained and flushed with RPMI medium. Cells were then centrigued and treated with ACK buffer to lyse RBC's. Cell pellets with then washed with and resuspended in RPMI medium and plated in six well plates in the presence of M-CSF. Medium was changed every 2 days. Treatments with Aza and HDACi were started after 4 days and the in vitro drug treatment schema was 5 days of Aza followed by either vehicle or the indicated HDACi (see figure) for 5 days. Cells were then collected and RNA extracted.

FACS sorting and profiling of macrophages and T cells LSL-Kras^{G12D}:

For FACS sorting of macrophages and CD8 T cells from LSL-KRasG12D mice, lungs were harvested from mock or treated mice following three months of treatment. Tissue was then digested for 30 minutes at 37 deg C in digestion buffer (RPMI, FBS (10%), Collagenase Type 1 (0.2%), Collagenase Type 2 (0.2%) and DNase I (50u/mL). Tissue was then minced and strained through a 40um cell strainer to obtain a single cell suspension. RBC's were then lysed with ACK buffer and the cell pellet was washed twice in RPMI prior to suspension in RPMI medium. Cells were then counted and blocked with Rat monoclonal anti-CD16/CD32 (Fc block Antibody) in PBS for 30 min at 4 deg C. Cells were then stained with antibodies against CD45, Cd11b and F4/80 for macrophages or CD45, CD3, CD8a for CD8^{+} T-cells. Propidium Iodide was used as a viability marker (5uL/100uL total volume). Cells were sorted and pellets were lysed and RNA extracted using RNeasy kit. RNA was then quantitated and amplified using the Sigma Whole Transcriptome Amplification kit. Amplified RNA was then processed and analyzed on an Agilent 4x44 single color microarray. Post sort purity checks were utilized and the sorted populations were determined to be more than 95% pure population.

FACS profiling T cells LSL-Kras^{G12D}:

For FACS sorting of macrophages and CD8$^+$ T cells from LLC mice, primary tumors were harvested from mock or treated mice following one month of treatment. Tissue was then digested using a mixture of collagenase, hyaluronidase and DNase. The resulting single cell suspension was counted and plated at in complete media (RPMI+10% FBS) with or with eBiosciences stimulation cocktail (1:1000) for 4 hours. Cells were then collected and blocked with Rat monoclonal anti-CD16/CD32 (Fc block Antibody) in PBS for 30 min at 4 deg C. Cells were then stained with antibodies against Live/dead, CD45, CD3, CD8a, and IFNγ for CD8$^+$ T-cells. Cells were then profiled by FACS.

Immune cell infiltration data:

IHC quantification- tumor infiltrating CD8 T cells were enumerated in field of view for hotspots of infiltration for the conditions indicated in the figure. The n values depicted indicate individual animals scored for infiltration. p values for IHC quantification data were derived using Graphpad Prism software and were defined as <0.05 by unpaired two tailed t test when comparing treated condition versus control, independent animals were used for the derivation of significance. FACS infiltration data- tumor infiltrating CD8 T cells were profiled from whole digested tumors. The n values depicted indicate individual animals profiled by FACS. p values for FACS data were derived using Graphpad Prism software and were defined as <0.05 by unpaired two tailed t test when comparing treated condition versus control, independent animals were used for the derivation of significance.

Gene expression analysis by microarray:

RNA expression were conducted by microarray for the conditions descibed in the relevant figures. The R/Bioconductor package limma was used to process expression data. Within- and between-array normalizations were performed using the loess and aquantile methods, respectively. The normexp option was used for background correction. Raw files read in using the read.maimages function. Log2 fold change in transcription for drug treated conditions over mock treated was obtained for each sample at each time point studied. Ranked lists of log2 fold change were analyzed using Gene Set Enrichment Analysis (GSEA) by the Broad Institute and data packages (Subramanian et al., 2005).

Hypergeometric test of cumulative distribution function:

The number of overlapping genes present in the Wherry et al. 2007 and our RNA expression data set (>0.5 log2 fold change, p value <0.05) were used to calculate over representation of these genes. p values were calculated using hypergeometric test of cumulative distribution function using p value/ representation calculator (http://systems.crump.ucla.edu/hypergeometric/).

3. Results

In the above mouse models, deployment of epigenetic treatment reverses tumor immune evasion status and a significant perturbation of tumor associated immune cell subsets appears to underlie the efficacy of the drug combinations. First, there is a robust alteration in the distribution of F4/80$^+$ macrophages which have been shown to have an established role in the progression of the LSL-Kras^{G12D} mouse model (Okayama et al.,

2013) These cells have been shown to basally infiltrate tumors induced in this model and our combination treatment results in a significant decrease in their numbers (**Figure 27A**). Transcriptional profiling of tumor associated macrophages (TAMs) isolated by FACS sorting of F4/80^{hi}, CD11b^{+} macrophages from the lungs following the three months of combination epigenetic treatment revealed differential expression of 1104 genes (**Figure 27B**) including significant downregulation of angiogenesis and hypoxia responsive genes and gene sets (**Figure 27C**). These observed perturbations appear to be a direct effect of the treatment and not a function of tumor stage, as treatment of normal bone marrow derived macrophages (BMDM) in vitro induces angiogenic signature downregulation as part of the 2295 differentially expressed genes (**Figures 27D and 27E**).

A

B

C

D

E

Figure 28: Combination epigenetic therapy reduces both macrophage infiltration and angiogenic signatures

(A) Representative IHC staining of F4/80$^+$ macrophages with F4/80 in LSL-Kras^{G12D} lung tumor sections treated with mock or Aza + ITF-2357 for 3 months. Upper panel: Representative F4/80$^+$ IHC; Lower panel: Positive pixel transformation of IHC images in upper panel using Aperio Imagescope software. Scale bar = 100 μ **(B)** Volcano plot of relative RNA expression from FACS sorted CD45$^+$CD11b$^+$F4/80^{hi} macrophages isolated from tumor bearing lungs from 3-month mock or Aza + ITF-2357 treated LSL-Kras^{G12D} mice. Genes in upper left and right quadrants are significantly, differentially expressed (microarray, n=2 per group). Hypoxia and angiogenic pathway associated genes are highlighted. (**C)** Key affected pathways obtained from GSEA of CD45$^+$CD11b$^+$F4/80^{hi} macrophage RNA isolated from tumor bearing lungs from 3-month Aza + ITF-2357 treated LSL-Kras^{G12D} mice as compared to mock treated mice. (**D)** Log2 fold relative RNA probe distribution showing differential gene expression from bone marrow derived macrophages (BMDMs) treated *in vitro* with mock or Aza + ITF-2357. Angiogenic pathway associated genes are highlighted. (microarray, BMDM data representative of n=3 mice). **(E)** BMDM GSEA enrichment plot angiogenesis pathway from BMDM RNA expression.

The above altered pathways in TAMS may have implications for mediating CD8$^+$ T cell intra-tumor infiltration. The inhibition of angiogenesis has proved efficacious in the MMTV mouse model through facilitating an increase in CD8$^+$ tumor infiltrating lymphocytes (Huang et al., 2012). This anti-angiogenic based strategy for the induced infiltration of T lymphocytes depends on the concept of vascular normalization (Huang et al., 2013). Therefore, the repression of angiogenic programs in macrophages may act locally in the tumor to create a more immune infiltrate permissive environment in the LSL-Kras^{G12D}.

Critically, there is increased CD8$^+$ tumor infiltrating lymphocytes (TILs) in the tumor microenvironment of treated mice (**Figure 28A**). This enhanced TIL accumulation is accompanied by an IFNγ responsive signature in the transcriptional profile of LSL-Kras^{G12D} whole tumor lysates (**Figure 28B**). As a validation of this signature, we profiled TILs by FACS in the LLC model and although we did not see any change in total CD8 numbers in this short-term treatment model, we observed a 2.25-fold increase in IFNγ positivity, as the result of exposure to epigenetic treatment (**Figure 28C).**

A

C

D

Figure 29: Combination epigenetic therapy induces the accumulation of activated T cells in the tumor microenvironment

(A) CD8⁺ IHC in lung tumors of mock and Aza + ITF-2357 treated LSL-Kras^{G12D} mice following 3 months of treatment, scale bar = 100 µ. The graph on the right indicates the average number of CD8⁺ T cells counted per field of view (FOV) intra-tumor for mock and treated mice. (n=6 mock, n=7 Aza + ITF=2357 mice). **(B)** Relative RNA expression based enrichment plot for 'hallmark interferon gamma response' gene set in tumors from LSL-Kras^{G12D} mice treated with mock and Aza + ITF-2357. Color gradation is representative of Log2 fold change over mock RNA expression (microarray, n=2 per group). **(C)** Percentage Ifnγ⁺ CD8⁺/CD3⁺ TILs by FACS in LLC subcutaneous tumors from one-month mock and Aza + ITF-2357 treated mice.

Transcriptional profiling of TILs from control and treated tumors in the LSL-Kras^{G12D} mice suggests a key role of epigenetic therapy on these cells. TILs are known to acquire an exhaustion state in response to continuous stimuli and interaction with inhibitory ligands (Wherry and Kurachi, 2015; Zehn and Wherry, 2015). Therefore, the reversion or prevention of this exhausted state remains a major hurdle for durable T cell mediated anti-tumor responses. A recent study by Ghoneim et al. established the utility of demethylating agents to reverse CD8^{+} T cell exhaustion, thereby allowing this population to be actionable by PD-1 blockade (Ghoneim et al., 2017). Our epigenetic treatment regimen induces alteration of the TIL transcriptome. Comparative analysis of our 3698 differentially expressed TIL genes (**Figure 29A**) revealed downregulation of exhaustion associated genes, and induction of activation and memory associated genes as defined by Wherry et al (Wherry et al., 2007). Our gene signature reflects an admixture of increased memory and/or effector T cells (**Figure 29B and 29C**).

A

B

C

Figure 30: Combination epigenetic therapy skews TIL phenotype towards memory and effector fates

(A) Volcano plot of relative RNA expression for $CD45^+CD3^+CD8^+$ FACS obtained lymphocytes isolated from tumor bearing lungs of 3-month Aza + ITF-2357 treated LSL-$Kras^{G12D}$ mice as compared to mock mice. Genes in upper left and right quadrants are significantly, differentially expressed (microarray, n=2 per group). Highlighted genes are involved in T cell fate determination. **(B and C)** Fold change in expression of selected differentially expressed genes in FACS obtained T cells from 3-month Aza + ITF-2357 treated mice. Genes shown are those which overlapped with exhaustion versus memory signatures **(B)** or exhaustion versus effector signatures **(C)** queried from Wherry et al. as defined in results. Genes on the left of each panel were differentially expressed by Aza + ITF-2357 and directionality in the gene set queried is on the right, red=upregulated and blue=downregulated. The associated p value for the probability of overlap as derived by hypergeometric probability calculation is depicted above each panel.

4. Discussion

The application of epigenetic treatment reduces the infiltration of macrophages into the tumor microenvironment. Additionally, we note a repression of angiogenic signatures associated with this population. We also observe a significant alteration of T cell phenotypes in the tumor microenvironment with a skewing away from exhausted towards memory and effector T cell phenotypes.

The expansion of these effector/memory T cell populations is associated with durable responses to immune checkpoint blockade (Ribas et al., 2016). Thus, through the deployment of epigenetic treatment in two animal models, we confirm epigenetic treatment can both increase activated CD8s in an inflamed tumor and induce the attraction of effector-memory CD8s to an immune desert tumor.

VI. Combination epigenetic treatment inhibits tumor growth through CD8$^+$ T cells and MYC dependent mechanisms

1. Introduction

The above demonstrated therapy effects can potentially reduce a barrier to immune therapy, namely, the failure of tumors to attract functional CD8$^+$ T cells. This leads to the question of whether the efficacy of epigenetic therapy is dependent on T cells in the tumor microenvironment and what events imparted by the therapy which may act to induce the noted T cell attraction.

2. Materials and methods

LLC model CD8 depletion model:

CD8a antibody (BioXcell, 2.43 clone) meidated CD8 depletion of male C57BL6 mice was intiated 3 days prior to onset of treatment (Day 4 post implantation). Implantation and therapeutic treatment of CD depleted LLC model is described in Lewis Lung Carcinoma model section of methods. For CD8 depletion mice were injected IP with 150ug of CD8a antibody (BioXcell, 2.43 clone), three times per week throughout the duration of study. CD8 depletion was verfied by assesment of CD8% of CD45 population in the spleen of depleted sample vs. control samples. Treatment was continued for a month followed and at the culmination of study mice were sacrificed, tumors were harvested and weighed. Lungs of these mice were inflated and fixed in formaldehyde for 24 hours prior to sectioning and staining with H&E stains.

Gene expression analysis by microarray:

RNA expression were conducted by microarray for the conditions descibed in the relevant figures. The R/Bioconductor package limma was used to process expression data. Within- and between-array normalizations were performed using the loess and aquantile methods, respectively. The normexp option was used for background correction. Raw files read in using the read.maimages function. Log2 fold change in transcription for drug treated conditions over mock treated was obtained for each sample at each time point studied. Ranked lists of log2 fold change were analyzed using Gene Set Enrichment Analysis (GSEA) by the Broad Institute and data packages (Subramanian et al., 2005). Pathways enriched with a false discovery rate less than 0.25 were selected with cutoff of 2.0 normalized enrichment score in human and 1.5 normalized enrichment score cutoff in mouse studies.

Bronchoalveolar lavage (BAL) fluid cytokine analysis:

1.0 mL of BAL fluid was instilled into the right lung of tumor bearing KrasG12D mice. 50uL of this BAL was utilized for cytokine analysis as described by the manufacturer (Raybiotech, QAM-CYT-1). Cytokine array was scanned by the manufacurer. Cytokine quantifcation was conducted using a standard curve of each cytokine present at known concentrations supplied by the manufactuer. p values for cytokine data were derived using Graphpad Prism software and were defined as <0.05 by unpaired two tailed t test when comparing treated condition versus control, biological replicates were used for the derivation of significance. Data are mean +/- SD between biological replicates.

TCGA Analysis :

Broad Morpheus tool was used to analyze TCGA LUAD data for the relationship between CCL5 and MYC. First the 2 genes were selected from available RNA seq data of 576 patients available. These data were used to generate a new heat map. This new heat map was sorted based on CCL5 and MYC expression and the samples were separated into low, intermediate and high expression groups. These subsets were than compared using the profile interaction tool, to generate the depicted plots. 576 LUAD samples were ranked by expression of CCL5 and MYC into: low, intermediate and high expression groups. These 3 expression categories for MYC and CCL5 were then compared as follows on the Y-axis, where gene(y) is sorted based on low, intermediate or high expression of other gene: MYC high:CCL5(y), MYCintermediate:CCL5(y), MYClow:CCL5(y), MYC(y):CCL5high, MYC(y):CCL5intermediate, MYC(y):CCL5low.

Patient and sample characteristics used for *MYC* amplification studies:

We analyzed pre-treatment exome data derived from a recently published set of NSCLC patients treated with immune checkpoint blockade (Anagnostou et al., 2017). Patient and sample characteristics as well as treatment and response assessments are described in detail elsewhere (Anagnostou et al., 2017). In brief, our study group consisted of two NSCLC patients treated with PD-1 blockade (CGLU117T1 and CGLU127T1) and two NSCLC patients treated with combined PD-1 and CTLA4 blockade (CGLU116T1 and CGLU161T1). All patients achieved a partial response of more than six months in duration (durable clinical benefit-DCB) apart from CGLU117T1, who achieved stable disease (22% tumor regression by RECIST 1.1) of 4 months duration before he developed disease progression (non-durable clinical benefit-NCB). An additional NSCLC tumor sample from a patient with sustained response to PD-1 blockade was obtained for comparative analysis of CD8+ T-cell density.

Somatic Copy Number Analysis:

Whole exome sequence data from a previously published cohort of four patients with NSCLC (Anagnostou et al., 2017) was evaluated to determine the somatic copy number of MYC locus in pre-treatment tumor samples. The sequencing depth of coverage of the tumor sample in bins spanning coding and non-coding regions of the genome were compared to the matched normal sample from each patient. The $\log_2$ read ratio values were corrected for biases resulting from the exome capture process and sequence composition using CNVKit (0.7.6) (Talevich et al., 2016), and were adjusted to account for variable normal cell contamination as previously described (Anagnostou et al., 2017).

3. Results

Depleting CD8$^+$ T cells in the LLC mouse model attenuated the efficacy of epigenetic treatment on the reduction of primary tumor burden (**Figure 30**). Relative to the Aza + ITF-2357 efficacy established in **Figure 25**, we also observe an increase in both metastatic frequency and burden as the result of CD8 depletion. In the CD8 depleted environment we noted a metastatic frequency of 33% in mock and 20% in Aza + ITF-2357 treated mice (**Figure 30**).

Figure 31: CD8 depletion in LLC model strongly antagonizes the efficacy of combination epigenetic therapy.

Weights of subcutaneous LLC tumors from one-month mock and Aza + ITF-2357 mice treated in the presence of CD8a depleting antibody (n=7 mock and n=5 treated mice) and representative H & E stained images of lung metastases from above one-month mock and Aza + ITF-2357 mice treated in the presence of CD8a depleting antibody (n=7 mock and n = 5 treated mice).

Additionally, in response to our combined epigenetic treatment there is transcriptional augmentation of CCL5, a secreted chemokine involved in lymphocyte attraction (**Figure 31A**). Importantly, protein levels of CCL5 also accumulate in bronchoalveolar lavage of mice treated with combination epigenetic therapy (**Figure 31B**). This protein and its ligand have been identified as the primary factors influencing T cell infiltration of melanoma post-chemotherapy (Hong et al., 2011). This suggests that the enhanced levels of CCL5 induced by the epigenetic treatment may contribute to the increased number of $CD8^+$ T cells observed in tumors of treated mice.

A **B**

Figure 32: T cell attraction is correlated with an induction of the T cell attractant cytokine CCL5

(A) Expression of ccl5 RNA in lung tumors from LSL-Kras^{G12D} mice in response to 3 months treatment with mock or Aza + ITF-2357 (microarray, n=2, p value < 0.05). **(B)** Quantitation of ccl5 protein levels in bronchoalveolar lavage from LSL-Kras^{G12D} mice treated with mock or Aza + ITF-2357 (n=3, error bars=SD, * p value < 0.05)

Several key findings suggest the importance of the above CCL5 results and link this parameter with the combination treatment mediated downregulation of MYC signaling. First, expression of exogenous MYC in human A549 NSCLC cells acts as a potent repressor of CCL5 transcriptional induction in response to epigenetic treatment **(Figure 32A)**. This links perturbation of MYC by epigenetic treatment to the alteration of immune correlates**.** Second, the potentially repressive role of MYC on CCL5 is also apparent in Cancer Genome Atlas project (TCGA) primary NSCLC, lung adenocarcinoma (LUAD) samples, wherein there is an inverse relationship between CCL5 and MYC RNA transcription (**Figure 32**)

A

B

Figure 33: CCL5 and MYC expression are inversely correlated in TCGA adenocarcinoma patient samples

(A) Relative fold change for CCL5 RNA expression in empty vector (EV) or MYC overexpressing A549 human NSCLC cells treated with 500nM Aza and/or 100nM ITF-2357 (qRT-PCR, Day 8, n=3, Data are presented as mean ± SEM, * p value < 0.05 relative to EV, # p value < 0.05 relative to EV + Aza + ITF-2357). **(B)** Profile interaction plots of TCGA RNA seq data for CCL5 and MYC expression across primary LUAD samples

Finally, our new findings in a small, previously reported cohort of patients with NSCLC treated with immune checkpoint therapy (Anagnostou et al., 2017) provide a suggestion for the importance of the present pre-clinical findings for the role of MYC signaling in response to immune therapy. In these four patients, all but one achieved durable clinical benefit with partial responses for greater than 6-months as defined by RECIST 1.1. Genome-wide copy number variation analysis on the tumors of these patients revealed a significant amplification of the *MYC* locus only in the one patient who did not achieve durable benefit (**Figure 33**). Of note, the tumors from all four patients had characteristics predicting favorable response to checkpoint blockade therapy (Anagnostou et al., 2017) including high PD-L1 protein expression and high mutation density (Rizvi et al., 2015; Tumeh et al., 2014).

A

B

Figure 34: MYC amplification antagonizes response to immune checkpoint blockade in small cohort of NSCLC patients

. **(A)** Somatic copy number status of the *MYC* locus in NSCLC tumors. A 1.13 Mbp segment overlapping *MYC* harbored a 12-fold amplification in CGLU117T1, the tumor that did not derive durable clinical benefit from immune checkpoint blockade. Orange lines represent segments of constant copy number. Circle and triangle markers indicate genomic bins in coding (target) and non-coding (off-target) regions, respectively. (**B)** Copy number status of chromosome 8. The heatmap depicts segmental copy ratios after tumor purity correction, highlighting the amplification of the MYC locus for CGLU117T1 (arrow), but not for the other tumors analyzed.

4. Discussion

These data demonstrate a correlative link between T cell attraction and induction of the potent T cell attractant CCL5. Furthermore, we demonstrate the causation of T cells in an aggressive adenocarcinoma model of NSCLC. Additionally, these data, which must be validated in larger patient cohorts, suggest a predictive value when considering both the genetic and expression status of MYC for monitoring outcomes and practicing precision medicine for patients with NSCLC and other cancers receiving immune checkpoint therapy.

VII. Summary Discussion

We have derived pre-clinical data supporting a role for epigenetic therapy in decreasing c-MYC signaling and driving a substantial anti-tumor response associated with a reversion of an immune evasion phenotype. We describe a novel regimen using careful selection of specific HDACi's in combination with Aza. We find the inhibition of HDAC1, 2, and 3 isoforms are key for inducing a profound proliferative arrest, imparting most of this effect at clinically relevant concentrations of ITF-2357 **(Figure 11B**). The inhibition of HDAC6 appears to play a more important role in interferon signaling **(Figures 17A-D)**, possibly involving its known function for regulating Stat-1 dependent NF-kB signaling (Kramer et al., 2006).

We find these HDACis can complement the therapeutic effects of Aza across a diverse panel of NSCLC cell lines, thus suggesting its applicability for the treatment of NSCLC **(Figures 6 and 7)**. Our observation of a strong correlation between both MYC basal levels and degree of downregulation by Aza suggest the importance of MYC assessment for the delineation of patients most likely to respond to epigenetic treatment **(Figure 21B and 21C)**.

The best indication of the translational potential for our combination epigenetic therapy are the phenotypic results achieved by treating two mouse models of NSCLC **(Figures 25 and 26)**. These models allow for our observations that the epigenetic treatment alters the intra-tumor localization and functional status of key immune cell populations **(Figures 28 and 29)**. This occurs concurrently with a decrease in MYC pathway signaling **(Figures 27E and 27F)**. The importance of MYC in driving tumor formation in the LSL-Kras^{G12D} mouse model has been established wherein inhibition of MYC and its targets has been shown to eradicate lung tumor lesions (Soucek et al., 2013).

Although the above antitumor responses are partly driven by the direct growth inhibitory effects of the therapy as observed in immune incompetent mice **(Figures 13A-13F)**, we also observed a significant alteration of immune populations mediated by our therapeutic paradigm when treating immune competent mouse models **(Figures 28 and 29)**. The crucial role of the CD8^{+} T cells in driving the anti-tumor response is apparent from the significant attenuation of the anti-tumor response in the immune competent mice following CD8 depletion (**Figure 31)**. Our observation of decreased angiogenic potential of tumor associated macrophages post treatment has implications in tumor vascularization, which is essential for the growth of large adenocarcinoma lesions **(Figures 28A-28E)**. Key among these findings is the effect of epigenetic treatment duration on the modulation of T cell fate. A critical observation is that application of epigenetic treatment for limited duration induces the accumulation of activated T effector cells **(Figure 29D)**, while chronic, long term treatment induces modulation away from an exhausted T cell phenotype, inducing a profile more indicative of the formation of effector-memory T cells **(Figures 30B and 30C)**. This acquisition of a memory phenotype coupled with intra-tumor accumulation of activated T-cells imparts an immunological landscape primed for durable response to immune checkpoint therapy (Ribas et al., 2016).

A final point for high translational implications is our linking epigenetic therapy induced attraction of CD8$^+$ T cells to the tumor microenvironment and the relationship of this event with decreased MYC signaling. An important parameter altered, which may have implications for the induced infiltration of CD8$^+$ T cells into the tumor microenvironment, is the simultaneous upregulation of CCL5 protein secretion into the bronchioloalveolar compartment **(Figures 32A and 32B)**. The forced overexpression of this secreted protein has been found to induce recruitment of T cells (Lavergne et al., 2004). Notably, others have found higher levels of CCL5 to be an independent prognostic indicator for longer overall survival, with an induction of an active tumor associated lymphocyte compartment in NSCLC patients (Moran et al., 2002).

In patient tumors, CCL5 augmentation by epigenetic therapy may prove crucial both functionally and as a biomarker in pre- and post-epigenetic treatment. As a biomarker, these data indicate that such findings for basal levels of CCL5 may be especially valuable when combined with the other markers studied such as the genetic and expression status of MYC. Considering these relationships may enable the prediction of those patients most likely to respond to combination of epigenetic and immune therapy. Specifically, based on our corollary hypothesis, patients with MYC high, CCL5 low tumors could be those who most benefit from this combination.

In summary, we believe that combination epigenetic therapy induced depletion of MYC can remove a barrier to interferon responsiveness, potentiate T cell attraction and cause direct anti-proliferative actions. This coupled with the reversion of T cell exhaustion and acquisition of a T cell memory fate suggest the potential for use of epigenetic therapy in combination with immune checkpoint blockade. Our early findings for *MYC* amplification in the one of four patients who had a much less robust initial response to immune checkpoint response than the others who achieved durable clinical benefit is in keeping with the need to further pursue these findings in the clinic **(Figure 7G and H)**. In this regard, the work in our present study, and the hypotheses derived are being pursued in the afore mentioned clinical trial for patients with NSCLC testing our combined epigenetic therapy, with the DNA demethylating agent, Guadecitabine plus the HDACi, Mocetinostat plus anti-PD1 (NCT03220477).

VIII. References

Anagnostou, V., Smith, K.N., Forde, P.M., Niknafs, N., Bhattacharya, R., White, J., Zhang, T., Adleff, V., Phallen, J., Wali, N., *et al.* (2017). Evolution of Neoantigen Landscape during Immune Checkpoint Blockade in Non-Small Cell Lung Cancer. Cancer discovery *7*, 264-276.

Bantscheff, M., C. Hopf, M. M. Savitski, A. Dittmann, P. Grandi, A. M. Michon, J. Schlegl, Y. Abraham, I. Becher, G. Bergamini, M. Boesche, M. Delling, B. Dumpelfeld, D. Eberhard, C. Huthmacher, T. Mathieson, D. Poeckel, V. Reader, K. Strunk, G. Sweetman, U. Kruse, G. Neubauer, N. G. Ramsden and G. Drewes (2011). "Chemoproteomics profiling of HDAC inhibitors reveals selective targeting of HDAC complexes." Nat Biotechnol 29(3): 255-265.

Barth, T. K. and A. Imhof (2010). "Fast signals and slow marks: the dynamics of histone modifications." Trends Biochem Sci 35(11): 618-626.

Baylin SB, Jones PA. (2016). Epigenetic Determinants of Cancer. Cold Spring Harb Perspect Biol. 1;8(9).

Bhalla, S., S. Balasubramanian, K. David, M. Sirisawad, J. Buggy, L. Mauro, S. Prachand, R. Miller, L. I. Gordon and A. M. Evens (2009). "PCI-24781 induces caspase and reactive oxygen species-dependent apoptosis through NF-kappaB mechanisms and is synergistic with bortezomib in lymphoma cells." Clin Cancer Res 15(10): 3354-336

Borghaei, H., Paz-Ares, L., Horn, L., Spigel, D.R., Steins, M., Ready, N.E., Chow, L.Q., Vokes, E.E., Felip, E., Holgado, E., *et al.* (2015). Nivolumab versus Docetaxel in Advanced Nonsquamous Non-Small-Cell Lung Cancer. The New England journal of medicine *373*, 1627-1639.

Boyer, L. A., M. R. Langer, K. A. Crowley, S. Tan, J. M. Denu and C. L. Peterson (2002). "Essential role for the SANT domain in the functioning of multiple chromatin remodeling enzymes." Mol Cell 10(4): 935-942.

Bradner, J.E., West, N., Grachan, M.L., Greenberg, E.F., Haggarty, S.J., Warnow, T., and Mazitschek, R. (2010). Chemical phylogenetics of histone deacetylases. Nature chemical biology *6*, 238-243.

Cai, Y., Geutjes, E.J., de Lint, K., Roepman, P., Bruurs, L., Yu, L.R., Wang, W., van Blijswijk, J., Mohammad, H., de Rink, I., *et al.* (2014). The NuRD complex cooperates with DNMTs to maintain silencing of key colorectal tumor suppressor genes. Oncogene *33*, 2157-2168.

Cai, Y., Tsai, H.C., Yen, R.C., Zhang, Y.W., Kong, X., Wang, W., Xia, L., and Baylin, S.B. (2017). Critical threshold levels of DNA methyltransferase 1 are required to maintain DNA methylation across the genome in human cancer cells. Genome research *27*, 533-544.

Cameron, E.E., Bachman, K.E., Myohanen, S., Herman, J.G., and Baylin, S.B. (1999). Synergy of demethylation and histone deacetylase inhibition in the re-expression of genes silenced in cancer. Nature genetics *21*, 103-107.

Casey, S.C., Tong, L., Li, Y., Do, R., Walz, S., Fitzgerald, K.N., Gouw, A.M., Baylot, V., Gutgemann, I., Eilers, M., *et al.* (2016). MYC regulates the antitumor immune response through CD47 and PD-L1. Science *352*, 227-231.

Charlet J, Duymich CE, Lay FD, Mundbjerg K, Dalsgaard Sørensen K, Liang G, Jones PA (2016). Bivalent Regions of Cytosine Methylation and H3K27 Acetylation Suggest an Active Role for DNA Methylation at Enhancers. Mol Cell 62(3):422-31.

Chen, Ueda, Dodge, Wang, and Li (2003). Establishment and Maintenance of Genomic Methylation Patterns in Mouse Embryonic Stem Cells by Dnmt3a and Dnmt3b. Mol Cell 23(16): 5594–5605.

Cheng, Z., Gong, Y., Ma, Y., Lu, K., Lu, X., Pierce, L.A., Thompson, R.C., Muller, S., Knapp, S., and Wang, J. (2013). Inhibition of BET bromodomain targets genetically diverse glioblastoma. Clinical cancer research : an official journal of the American Association for Cancer Research *19*, 1748-1759.

Chiappinelli, K.B., Strissel, P.L., Desrichard, A., Li, H., Henke, C., Akman, B., Hein, A., Rote, N.S., Cope, L.M., Snyder, A., *et al.* (2015). Inhibiting DNA Methylation Causes an Interferon Response in Cancer via dsRNA Including Endogenous Retroviruses. Cell *162*, 974-986.

Codina, A., J. D. Love, Y. Li, M. A. Lazar, D. Neuhaus and J. W. Schwabe (2005). Structural insights into the interaction and activation of histone deacetylase 3 by nuclear receptor corepressors. Proc Natl Acad Sci U S A 102(17): 6009-6014.

Cancer Genome Atlas Research Network. (2014). Comprehensive molecular profiling of lung adenocarcinoma. Nature ;511(7511):543-50

Cancer Genome Atlas Research Network. (2012). Comprehensive genomic characterization of squamous cell lung cancers. Nature;489(7417):519-25.

Denslow, S. A. and P. A. Wade (2007). The human Mi-2/NuRD complex and gene regulation. Oncogene 26(37): 5433-5438.

Derissen, Beijnen, Schellens (2013). Concise Drug Review: Azacitidine and Decitabine. Oncologist. 18(5): 619–624.

Duymich CE, Charlet J, Yang X, Jones PA, Liang G (2016). DNMT3B isoforms without catalytic activity stimulate gene body methylation as accessory proteins in somatic cells. Nat Commun. 7:11453.

Ebert, D. H., H. W. Gabel, N. D. Robinson, N. R. Kastan, L. S. Hu, S. Cohen, A. J. Navarro, M. J. Lyst, R. Ekiert, A. P. Bird and M. E. Greenberg (2013). "Activity-dependent phosphorylation of MeCP2 threonine 308 regulates interaction with NCoR." Nature 499(7458): 341-345.

Falkenberg, K.J., and Johnstone, R.W. (2014). Histone deacetylases and their inhibitors in cancer, neurological diseases and immune disorders. Nature reviews Drug discovery *13*, 673-691.

Forneris, F., C. Binda, A. Adamo, E. Battaglioli and A. Mattevi (2007). "Structural basis of LSD1-CoREST selectivity in histone H3 recognition." J Biol Chem 282(28): 20070-20074.

Fotheringham, S., M. T. Epping, L. Stimson, O. Khan, V. Wood, F. Pezzella, R. Bernards and N. B. La Thangue (2009). Genome-wide loss-of-function screen reveals an important role for the proteasome in HDAC inhibitor-induced apoptosis. Cancer Cell 15(1): 57-66.

Furlan, A., Monzani, V., Reznikov, L.L., Leoni, F., Fossati, G., Modena, D., Mascagni, P., and Dinarello, C.A. (2011). Pharmacokinetics, safety and inducible cytokine responses during a phase 1 trial of the oral histone deacetylase inhibitor ITF2357 (givinostat). Molecular medicine *17*, 353-362.

Garon, E.B., Rizvi, N.A., Hui, R., Leighl, N., Balmanoukian, A.S., Eder, J.P., Patnaik, A., Aggarwal, C., Gubens, M., Horn, L., *et al.* (2015). Pembrolizumab for the treatment of non-small-cell lung cancer. The New England journal of medicine *372*, 2018-2028.

Ghoneim, H.E., Fan, Y., Moustaki, A., Abdelsamed, H.A., Dash, P., Dogra, P., Carter, R., Awad, W., Neale, G., Thomas, P.G., *et al.* (2017). De Novo Epigenetic Programs Inhibit PD-1 Blockade-Mediated T Cell Rejuvenation. Cell *170*, 142-157 e119.

Gore, L., Rothenberg, M.L., O'Bryant, C.L., Schultz, M.K., Sandler, A.B., Coffin, D., McCoy, C., Schott, A., Scholz, C., and Eckhardt, S.G. (2008). A phase I and pharmacokinetic study of the oral histone deacetylase inhibitor, MS-275, in patients with refractory solid tumors and lymphomas. Clinical cancer research : an official journal of the American Association for Cancer Research *14*, 4517-4525.

Guenther, M. G., O. Barak and M. A. Lazar (2001). The SMRT and N-CoR corepressors are activating cofactors for histone deacetylase 3. Mol Cell Biol 21(18): 6091-6101.

Gui, C. Y., L. Ngo, W. S. Xu, V. M. Richon and P. A. Marks (2004). "Histone deacetylase (HDAC) inhibitor activation of p21WAF1 involves changes in promoter-associated proteins, including HDAC1." Proc Natl Acad Sci U S A 101(5): 1241-1246.

Herbst R.S., Heymach J.V., Lippman S.M. (2008) Lung Cancer. N Engl J Med. 25;359(13):1367-80.

Holz-Schietinger C, Reich NO. (2010). The inherent processivity of the human de novo methyltransferase 3A (DNMT3A) is enhanced by DNMT3L. J Biol Chem. 17;285(38):29091-100.

Hong, M., Puaux, A.L., Huang, C., Loumagne, L., Tow, C., Mackay, C., Kato, M., Prevost-Blondel, A., Avril, M.F., Nardin, A., *et al.* (2011). Chemotherapy induces intratumoral expression of chemokines in cutaneous melanoma, favoring T-cell infiltration and tumor control. Cancer research *71*, 6997-7009.

Huang da, W., Sherman, B.T., and Lempicki, R.A. (2009a). Bioinformatics enrichment tools: paths toward the comprehensive functional analysis of large gene lists. Nucleic acids research *37*, 1-13.

Huang da, W., Sherman, B.T., and Lempicki, R.A. (2009b). Systematic and integrative analysis of large gene lists using DAVID bioinformatics resources. Nature protocols *4*, 44-57.

Huang, Y., Goel, S., Duda, D.G., Fukumura, D., and Jain, R.K. (2013). Vascular normalization as an emerging strategy to enhance cancer immunotherapy. Cancer research *73*, 2943-2948.

Huang, Y., Yuan, J., Righi, E., Kamoun, W.S., Ancukiewicz, M., Nezivar, J., Santosuosso, M., Martin, J.D., Martin, M.R., Vianello, F., *et al.* (2012). Vascular normalizing doses of antiangiogenic treatment reprogram the immunosuppressive tumor microenvironment and enhance immunotherapy. Proceedings of the National Academy of Sciences of the United States of America *109*, 17561-17566.

Jackson, E.L., Willis, N., Mercer, K., Bronson, R.T., Crowley, D., Montoya, R., Jacks, T., and Tuveson, D.A. (2001). Analysis of lung tumor initiation and progression using conditional expression of oncogenic K-ras. Genes & development *15*, 3243-3248.

Jones, P.A. and Baylin, S (2014). The epigenomics of cancer. Cell; 128(4): 683–692.

Jones, P.A., Issa, J.P., and Baylin, S. (2016). Targeting the cancer epigenome for therapy. Nature reviews Genetics *17*, 630-641.

Jones, S. F., J. R. Infante, D. R. Spigel, N. W. Peacock, D. S. Thompson, F. A. Greco, W. McCulloch and H. A. Burris, 3rd (2012). "Phase 1 results from a study of romidepsin in combination with gemcitabine in patients with advanced solid tumors." Cancer Invest 30(6): 481-486.

Juergens, R.A., Wrangle, J., Vendetti, F.P., Murphy, S.C., Zhao, M., Coleman, B., Sebree, R., Rodgers, K., Hooker, C.M., Franco, N., *et al.* (2011). Combination epigenetic therapy has efficacy in patients with refractory advanced non-small cell lung cancer. Cancer discovery *1*, 598-607.

Khan, O., S. Fotheringham, V. Wood, L. Stimson, C. Zhang, F. Pezzella, M. Duvic, D. J. Kerr and N. B. La Thangue (2010). "HR23B is a biomarker for tumor sensitivity to HDAC inhibitor-based therapy." Proc Natl Acad Sci U S A 107(14): 6532-6537

Kellar, A., Egan, C., and Morris, D. (2015). Preclinical Murine Models for Lung Cancer: Clinical Trial Applications. BioMed research international *2015*, 621324.

Kim, M., L. A. Thompson, S. D. Wenger and C. L. O'Bryant (2012). "Romidepsin: a histone deacetylase inhibitor for refractory cutaneous T-cell lymphoma." Ann Pharmacother 46(10): 1340-1348.

Kramer, O.H., Baus, D., Knauer, S.K., Stein, S., Jager, E., Stauber, R.H., Grez, M., Pfitzner, E., and Heinzel, T. (2006). Acetylation of Stat1 modulates NF-kappaB activity. Genes & development *20*, 473-485.

Lavergne, E., Combadiere, C., Iga, M., Boissonnas, A., Bonduelle, O., Maho, M., Debre, P., and Combadiere, B. (2004). Intratumoral CC chemokine ligand 5 overexpression delays tumor growth and increases tumor cell infiltration. Journal of immunology *173*, 3755-3762.

Lee, H. Z., V. E. Kwitkowski, P. L. Del Valle, M. S. Ricci, H. Saber, B. A. Habtemariam, J. Bullock, E. Bloomquist, Y. Li Shen, X. H. Chen, J. Brown, N. Mehrotra, S. Dorff, R. Charlab, R. C. Kane, E. Kaminskas, R. Justice, A. T. Farrell and R. Pazdur (2015). "FDA Approval: Belinostat for the Treatment of Patients with Relapsed or Refractory Peripheral T-cell Lymphoma." Clin Cancer Res 21(12): 2666-2670.

Li, H., Chiappinelli, K.B., Guzzetta, A.A., Easwaran, H., Yen, R.W., Vatapalli, R., Topper, M.J., Luo, J., Connolly, R.M., Azad, N.S., *et al.* (2014). Immune regulation by low doses of the DNA methyltransferase inhibitor 5-azacitidine in common human epithelial cancers. Oncotarget *5*, 587-598.

Lombardi, P. M., K. E. Cole, D. P. Dowling and D. W. Christianson (2011). "Structure, mechanism, and inhibition of histone deacetylases and related metalloenzymes." Curr Opin Struct Biol 21(6): 735-743.

Mann, B. S., J. R. Johnson, K. He, R. Sridhara, S. Abraham, B. P. Booth, L. Verbois, D. E. Morse, J. M. Jee, S. Pope, R. S. Harapanhalli, R. Dagher, A. Farrell, R. Justice and R. Pazdur (2007). "Vorinostat for treatment of cutaneous manifestations of advanced primary cutaneous T-cell lymphoma." Clin Cancer Res 13(8): 2318-2322.

Mann, B. S., J. R. Johnson, M. H. Cohen, R. Justice and R. Pazdur (2007). "FDA approval summary: vorinostat for treatment of advanced primary cutaneous T-cell lymphoma." Oncologist 12(10): 1247-1252.

Meilinger, Fellinger, Bultmann, Rothbauer, Bonapace, Klinkert, Spada, Leonhardt. (2009) Np95 interacts with de novo DNA methyltransferases, Dnmt3a and Dnmt3b, and mediates epigenetic silencing of the viral CMV promoter in embryonic stem cells. EMBO Rep. 10(11): 1259–1264.

Moran, C.J., Arenberg, D.A., Huang, C.C., Giordano, T.J., Thomas, D.G., Misek, D.E., Chen, G., Iannettoni, M.D., Orringer, M.B., Hanash, S., *et al.* (2002). RANTES expression is a predictor of survival in stage I lung adenocarcinoma. Clinical cancer research : an official journal of the American Association for Cancer Research *8*, 3803-3812.

Moreno-Bost, A., Szmania, S., Stone, K., Garg, T., Hoerring, A., Szymonifka, J., Shaughnessy, J., Jr., Barlogie, B., Prentice, H.G., and van Rhee, F. (2011). Epigenetic modulation of MAGE-A3 antigen expression in multiple myeloma following treatment with the demethylation agent 5-azacitidine and the histone deacetlyase inhibitor MGCD0103. Cytotherapy *13*, 618-628.

New, M., H. Olzscha and N. B. La Thangue (2012). "HDAC inhibitor-based therapies: can we interpret the code?" Mol Oncol 6(6): 637-656.

Phiel, C. J., F. Zhang, E. Y. Huang, M. G. Guenther, M. A. Lazar and P. S. Klein (2001). "Histone deacetylase is a direct target of valproic acid, a potent anticonvulsant, mood stabilizer, and teratogen." J Biol Chem 276(39): 36734-36741.

Oi, S., Natsume, A., Ito, M., Kondo, Y., Shimato, S., Maeda, Y., Saito, K., and Wakabayashi, T. (2009). Synergistic induction of NY-ESO-1 antigen expression by a novel histone deacetylase inhibitor, valproic acid, with 5-aza-2'-deoxycytidine in glioma cells. Journal of neuro-oncology *92*, 15-22.

Okayama, H., Saito, M., Oue, N., Weiss, J.M., Stauffer, J., Takenoshita, S., Wiltrout, R.H., Hussain, S.P., and Harris, C.C. (2013). NOS2 enhances KRAS-induced lung carcinogenesis, inflammation and microRNA-21 expression. International journal of cancer *132*, 9-18.

Perissi, V., K. Jepsen, C. K. Glass and M. G. Rosenfeld (2010). "Deconstructing repression: evolving models of co-repressor action." Nat Rev Genet 11(2): 109-123.

Prince, H. M., M. J. Bishton and S. J. Harrison (2009). "Clinical studies of histone deacetylase inhibitors." Clin Cancer Res 15(12): 3958-3969

Rao, R., S. Nalluri, R. Kolhe, Y. Yang, W. Fiskus, J. Chen, K. Ha, K. M. Buckley, R. Balusu, V. Coothankandaswamy, A. Joshi, P. Atadja and K. N. Bhalla (2010). "Treatment with panobinostat induces glucose-regulated protein 78 acetylation and endoplasmic reticulum stress in breast cancer cells." Mol Cancer Ther 9(4): 942-952.

Rasheed, W.K., Johnstone, R.W., and Prince, H.M. (2007). Histone deacetylase inhibitors in cancer therapy. Expert opinion on investigational drugs *16*, 659-678.

Reck, M., Rodriguez-Abreu, D., Robinson, A.G., Hui, R., Csoszi, T., Fulop, A., Gottfried, M., Peled, N., Tafreshi, A., Cuffe, S., *et al.* (2016). Pembrolizumab versus Chemotherapy for PD-L1-Positive Non-Small-Cell Lung Cancer. The New England journal of medicine *375*, 1823-1833.

Richardson, P. G., R. D. Harvey, J. P. Laubach, P. Moreau, S. Lonial and J. F. San-Miguel (2016). "Panobinostat for the treatment of relapsed or relapsed/refractory multiple myeloma: pharmacology and clinical outcomes." Expert Rev Clin Pharmacol 9(1): 35-48.

Ribas, A., Shin, D.S., Zaretsky, J., Frederiksen, J., Cornish, A., Avramis, E., Seja, E., Kivork, C., Siebert, J., Kaplan-Lefko, P., *et al.* (2016). PD-1 Blockade Expands Intratumoral Memory T Cells. Cancer immunology research *4*, 194-203.

Rinaldi L, Datta D, Serrat J, Morey L, Solanas G, Avgustinova A, Blanco E, Pons JI, Matallanas D, Von Kriegsheim A, Di Croce L, Benitah SA. (2016) Cell Stem Cell 19(4):491-501.

Rizvi, N.A., Hellmann, M.D., Snyder, A., Kvistborg, P., Makarov, V., Havel, J.J., Lee, W., Yuan, J., Wong, P., Ho, T.S., *et al.* (2015). Cancer immunology. Mutational landscape determines sensitivity to PD-1 blockade in non-small cell lung cancer. Science *348*, 124-128.

Ropero, S. and M. Esteller (2007). "The role of histone deacetylases (HDACs) in human cancer." Mol Oncol 1(1): 19-25.

Rose, N. R. and R. J. Klose (2014). "Understanding the relationship between DNA methylation and histone lysine methylation." Biochim Biophys Acta 1839(12): 1362-1372.

Roulois, D., Loo Yau, H., Singhania, R., Wang, Y., Danesh, A., Shen, S.Y., Han, H., Liang, G., Jones, P.A., Pugh, T.J., *et al.* (2015). DNA-Demethylating Agents Target Colorectal Cancer Cells by Inducing Viral Mimicry by Endogenous Transcripts. Cell *162*, 961-973.

Ryan, Q.C., Headlee, D., Acharya, M., Sparreboom, A., Trepel, J.B., Ye, J., Figg, W.D., Hwang, K., Chung, E.J., Murgo, A., *et al.* (2005). Phase I and pharmacokinetic study of MS-275, a histone deacetylase inhibitor, in patients with advanced and refractory solid tumors or lymphoma. Journal of clinical oncology : official journal of the American Society of Clinical Oncology *23*, 3912-3922.

San-Miguel, J. F., P. G. Richardson, A. Gunther, O. Sezer, D. Siegel, J. Blade, R. LeBlanc, H. Sutherland, M. Sopala, K. K. Mishra, S. Mu, P. M. Bourquelot, M. Victoria Mateos and K. C. Anderson (2013). "Phase Ib study of panobinostat and bortezomib in relapsed or relapsed and refractory multiple myeloma." J Clin Oncol 31(29): 3696-3703.

Schlee, M., Holzel, M., Bernard, S., Mailhammer, R., Schuhmacher, M., Reschke, J., Eick, D., Marinkovic, D., Wirth, T., Rosenwald, A., *et al.* (2007a). C-myc activation impairs the NF-kappaB and the interferon response: implications for the pathogenesis of Burkitt's lymphoma. International journal of cancer *120*, 1387-1395.

Schlee, M., Schuhmacher, M., Holzel, M., Laux, G., and Bornkamm, G.W. (2007b). c-MYC impairs immunogenicity of human B cells. Advances in cancer research *97*, 167-188.

Shao, Y., Z. Gao, P. A. Marks and X. Jiang (2004). "Apoptotic and autophagic cell death induced by histone deacetylase inhibitors." Proc Natl Acad Sci U S A 101(52): 18030-18035.

Soucek, L., Whitfield, J.R., Sodir, N.M., Masso-Valles, D., Serrano, E., Karnezis, A.N., Swigart, L.B., and Evan, G.I. (2013). Inhibition of Myc family proteins eradicates KRas-driven lung cancer in mice. Genes & development *27*, 504-513.

Stengel, S., Fiebig, U., Kurth, R., and Denner, J. (2010). Regulation of human endogenous retrovirus-K expression in melanomas by CpG methylation. Genes, chromosomes & cancer *49*, 401-411.

Stresemann C, Lyko F. (2008). Modes of action of the DNA methyltransferase inhibitors azacytidine and decitabine. Int J Cancer. 123(1):8-13.

Stimson, L. and N. B. La Thangue (2009). "Biomarkers for predicting clinical responses to HDAC inhibitors." Cancer Lett 280(2): 177-183

Strissel, P.L., Ruebner, M., Thiel, F., Wachter, D., Ekici, A.B., Wolf, F., Thieme, F., Ruprecht, K., Beckmann, M.W., and Strick, R. (2012). Reactivation of codogenic endogenous retroviral (ERV) envelope genes in human endometrial carcinoma and prestages: Emergence of new molecular targets. Oncotarget *3*, 1204-1219.

Subramanian, A., Tamayo, P., Mootha, V.K., Mukherjee, S., Ebert, B.L., Gillette, M.A., Paulovich, A., Pomeroy, S.L., Golub, T.R., Lander, E.S., *et al.* (2005). Gene set enrichment analysis: a knowledge-based approach for interpreting genome-wide expression profiles. Proceedings of the National Academy of Sciences of the United States of America *102*, 15545-15550.

Talevich, E., Shain, A.H., Botton, T., and Bastian, B.C. (2016). CNVkit: Genome-Wide Copy Number Detection and Visualization from Targeted DNA Sequencing. PLoS computational biology *12*, e1004873.

Tsai, H.C., Li, H., Van Neste, L., Cai, Y., Robert, C., Rassool, F.V., Shin, J.J., Harbom, K.M., Beaty, R., Pappou, E., *et al.* (2012). Transient low doses of DNA-demethylating agents exert durable antitumor effects on hematological and epithelial tumor cells. Cancer cell *21*, 430-446.

Tumeh, P.C., Harview, C.L., Yearley, J.H., Shintaku, I.P., Taylor, E.J., Robert, L., Chmielowski, B., Spasic, M., Henry, G., Ciobanu, V., *et al.* (2014). PD-1 blockade induces responses by inhibiting adaptive immune resistance. Nature *515*, 568-571.

Verdin, E., F. Dequiedt and H. G. Kasler (2003). "Class II histone deacetylases: versatile regulators." Trends Genet 19(5): 286-293.

Wang, Y., H. Zhang, Y. Chen, Y. Sun, F. Yang, W. Yu, J. Liang, L. Sun, X. Yang, L. Shi, R. Li, Y. Li, Y. Zhang, Q. Li, X. Yi and Y. Shang (2009). "LSD1 is a subunit of the NuRD complex and targets the metastasis programs in breast cancer." Cell 138(4): 660-672.

Weiser, T.S., Guo, Z.S., Ohnmacht, G.A., Parkhurst, M.L., Tong-On, P., Marincola, F.M., Fischette, M.R., Yu, X., Chen, G.A., Hong, J.A., *et al.* (2001). Sequential 5-Aza-2 deoxycytidine-depsipeptide FR901228 treatment induces apoptosis preferentially in cancer cells and facilitates their recognition by cytolytic T lymphocytes specific for NY-ESO-1. Journal of immunotherapy *24*, 151-161.

Wherry, E.J., Ha, S.J., Kaech, S.M., Haining, W.N., Sarkar, S., Kalia, V., Subramaniam, S., Blattman, J.N., Barber, D.L., and Ahmed, R. (2007). Molecular signature of CD8+ T cell exhaustion during chronic viral infection. Immunity *27*, 670-684.

Wherry, E.J., and Kurachi, M. (2015). Molecular and cellular insights into T cell exhaustion. Nature reviews Immunology *15*, 486-499.

Witt, O. and R. Lindemann (2009). "HDAC inhibitors: magic bullets, dirty drugs or just another targeted therapy." Cancer Lett 280(2): 123-124.

Witt, O., H. E. Deubzer, T. Milde and I. Oehme (2009). "HDAC family: What are the cancer relevant targets?" Cancer Lett 277(1): 8-21.

Wrangle, J., Wang, W., Koch, A., Easwaran, H., Mohammad, H.P., Vendetti, F., Vancriekinge, W., Demeyer, T., Du, Z., Parsana, P., *et al.* (2013). Alterations of immune response of Non-Small Cell Lung Cancer with Azacytidine. Oncotarget *4*, 2067-2079.

Xia L, Huang W, Bellani M, Seidman MM, Wu K, Fan D, Nie Y, Cai Y, Zhang YW, Yu LR, Li H, Zahnow CA, Xie W, Chiu Yen RW, Rassool FV, Baylin SB. (2017). CHD4 Has Oncogenic Functions in Initiating and Maintaining Epigenetic Suppression of Multiple Tumor Suppressor Genes. Cancer Cell;31(5):653-668.

Yang, W. M., S. C. Tsai, Y. D. Wen, G. Fejer and E. Seto (2002). Functional domains of histone deacetylase-3. J Biol Chem 277(11): 9447-9454.

Yang, M., C. B. Gocke, X. Luo, D. Borek, D. R. Tomchick, M. Machius, Z. Otwinowski and H. Yu (2006). "Structural basis for CoREST-dependent demethylation of nucleosomes by the human LSD1 histone demethylase." Mol Cell 23(3): 377-387.

Yardley, D. A., R. R. Ismail-Khan, B. Melichar, M. Lichinitser, P. N. Munster, P. M. Klein, S. Cruickshank, K. D. Miller, M. J. Lee and J. B. Trepel (2013). "Randomized phase II, double-blind, placebo-controlled study of exemestane with or without entinostat in postmenopausal women with locally recurrent or metastatic estrogen receptor-positive breast cancer progressing on treatment with a nonsteroidal aromatase inhibitor." J Clin Oncol 31(17): 2128-2135.

Zahnow, C.A., Topper, M., Stone, M., Murray-Stewart, T., Li, H., Baylin, S.B., and Casero, R.A., Jr. (2016). Inhibitors of DNA Methylation, Histone Deacetylation, and Histone Demethylation: A Perfect Combination for Cancer Therapy. Advances in cancer research *130*, 55-111.

Zehn, D., and Wherry, E.J. (2015). Immune Memory and Exhaustion: Clinically Relevant Lessons from the LCMV Model. Advances in experimental medicine and biology *850*, 137-152.

Zhang, J., M. Kalkum, B. T. Chait and R. G. Roeder (2002). "The N-CoR-HDAC3 nuclear receptor corepressor complex inhibits the JNK pathway through the integral subunit GPS2." Mol Cell 9(3): 611-623.

IX. Biographical Sketch

Michael J. Topper

Date of Birth: November 11, 1984

Education

2012-Present	*Ph.D.* Cellular and Molecular Medicine, **Johns Hopkins University, School of Medicine**, Baltimore, Maryland
2011	*B.S.* Biological Sciences, **University of Maryland, Baltimore County**, Baltimore, Maryland

Research Experience

2012-Present	Doctoral Student, Cellular and Molecular Medicine Program, Johns Hopkins University School of Medicine, Baltimore, MD Principal Investigator: Stephen Baylin, M.D. Dissertation Title: Epigenetic therapy ties MYC depletion to reversing immune evasion and treating lung cancer
2008-2010	Undergraduate Research Assistant, University of Maryland, Baltimore County. Baltimore, MD Principal Investigator: Jeff Leips, Ph.D. Project: Age specific Immunocompetence in Drosophila Melanogaster

Selected Poster Presentations

Sequential Azacitidine and histone deacetylase inhibition induces a potent anti-tumor response in a genetically engineered mouse model of non-small cell lung cancer. AACR Annual Meeting 2017, Washington D.C.

Combination Azacitidine and histone deacetylase inhibition induces a multi factorial synergistic anti-tumor response in non-small cell lung cancer. Sidney Kimmel Comprehensive Cancer Center Research Fellows Day 2016, (Poster First Place Clinical/Translational category). Baltimore, MD

Combination Azacitidine and histone deacetylase inhibition induces a multi factorial synergistic anti-tumor response in non-small cell lung cancer (NSCLC) AACR Annual Meeting 2016, New Orleans, LA.

Genome wide association tests for age-specific immunocompetence in Drosophila. Drosophila Research Conference 2010, Washington D.C.

Publications

Topper MJ, Vaz M, Chiappinelli K, Shields CD, Niknafs N, Chiu Yen RC, Wenzel A, Hicks J, Ballew M, Stone M, Tran P, Zahnow CA, Hellmann M, Anagnostou V, Strissel P, Strick R, Velculescu V, Baylin SB (2017) Epigenetic therapy ties MYC depletion to reversing immune evasion and treating lung cancer. *Cell,* accepted manuscript.

Zahnow CA, Topper M, Stone M, Murray-Stewart T, Li H, Baylin SB, Casero RA Jr. (2016). Inhibitors of DNA Methylation, Histone Deacetylation, and Histone Demethylation: A Perfect Combination for Cancer Therapy. *Adv Cancer Res.,* 130:55-111

Vendetti FP, Topper M, Huang P, Dobromilskaya I, Easwaran H, Wrangle J, Baylin SB, Poirier JT, Rudin CM. (2015). Evaluation of azacitidine and entinostat as sensitization agents to cytotoxic chemotherapy in preclinical models of non-small cell lung cancer. *Oncotarget*;6(1):56-70.

Li H, Chiappinelli KB, Guzzetta AA, Easwaran H, Yen RW, Vatapalli R, Topper MJ, Luo J, Connolly RM, Azad NS, Stearns V, Pardoll DM, Davidson N, Jones PA, Slamon DJ, Baylin SB, Zahnow CA, Ahuja N. (2014). Immune regulation by low doses of the DNA methyltransferase inhibitor 5-azacitidine in common human epithelial cancers. *Oncotarget*;5(3):587-98.